Steady and Pulsatile Flow in Curved Vessels

Thesis by

Mehrdad Mahmoudi Zarandi

In Partial Fulfillment of the Requirements

for the Degree of

Doctor of Philosophy

California Institute of Technology

Pasadena, California

2000

(Submitted January 3, 2000)

Acknowledgements

The author wishes to thank many people who have contributed to what might be considered worthwhile in this thesis. First of all, without the constant guidance and inspiration of my advisor, Professor Morteza Gharib, it would have never become a reality. His deep and far-reaching insight has taught me more than what is manifested in the current work. I will always remain grateful to him for all that he has taught me in various realms of academic research as well as in many other aspects of life. The credit for much of this work goes to him more than to anybody else.

I would like to thank my thesis committee members, Professors John Brady, Julia Kornfield and David Tirrel for their generous guidance and support. Other members of the Chemical Engineering Department at Caltech, especially Professor George Gavalas, have helped me during my graduate work. Professor Guruswaminaidu Ravichandran from GALCIT and Professor David Sahn from Oregon University School of Health Sciences have also provided generous help which is much appreciated. In addition, I am grateful to Professor Mary Lidstrom and Professor Zhen-gang Wang for their generous support.

I am also grateful to the members of Professor Gharib's research group and technical staff who have helped me at different stages of this work. Edmond Rambod, Haitao Huang, Brad Dooley, David Kuzo, Han Park, Flavio Noca, David Jeon, Lavi Zuhal, Michael Ol, Hilla Shaviv, Fabien Scheurer, Frederic Taugwalder, Francisco Pereira, Dana Dabiri, Steve Haase, Ken Chadwick, Yu-Chi Chu, Bahram Valiferdowsi, Alan Goudy, Kathleen Hamilton and Lori Cameron have all contributed to various extents to the accomplishment of this work.

I have enjoyed the financial support provided by the California Institute of Tech-

nology through various research and teaching assistantships and through funding by the Powell Foundation. My sincere thanks and appreciation goes to Caltech and the Powell Foundation for their support.

My parents, Ahmad and Parvin, my sisters, Minoo, Mehrnaz and Mehrnoosh, and my brother Mahdi, have always been there with their love and guidance. I am grateful to all of them for what they have been.

Tutti li miei pensier parlan d'Amore;

(Dante, La Vita Nova)

Abstract

An experimental investigation is carried out on the nature of secondary flow patterns in a curved vessel. This study concentrates on the role of the upstream spatial boundary conditions and the time-periodicity of the formation of the secondary flow patterns in curved vessels. Four sets of studies are made. In the first set, steady flow is compared to a pulsatile flow simulating the physiological conditions in the human aorta. To study the effect of spatial upstream boundary conditions, we investigated the effect of an upstream constriction, which represents the actual physiological conditions in the human aorta. All *in vitro* studies are carried out in models with dimensions close to those of the human aorta and with the Reynolds number ($1400 < Re < 7000$), Dean number ($1470 < De < 7300$) and Womersley number ($8.6 < \alpha < 12.6$) all in a range close to the physiological values. The technique of Digital Particle Image Velocimetry is used to measure instantaneous and average flow fields.

In the first stage of this research, an orifice with a stenosis ratio of $\beta = 80\%$ is used to simulate the upstream constriction and study its effect on the secondary flow patterns. It is found that the existence of the upstream constriction profoundly changes the nature of the secondary flow pattern. In the presence of the upstream constriction, the double circulation pattern of Dean flow is substituted with a single circulation pattern.

Next, to investigate where the transition from one pattern to the other occurs, similar sets of experiments are carried out with constrictions of different sizes corresponding to stenosis ratios of $\beta = 65\%$ and $\beta = 88\%$. In addition, to investigate the sense of rotation for the single circulation pattern, an orifice with an asymmetric opening mounted at different angular positions is used.

The comparison of the secondary flow patterns for steady versus pulsatile flow revealed that the flow pattern does not change its main structure due to the time-periodicity of the flow. However, the pulsatile flow in general shows secondary flow

rates greater than the steady flow.

On the other hand, the spatial boundary conditions are found to be central in determining the secondary flow patterns. First, the presence of an upstream constriction or stenosis ratio of $\beta = 65\%$ will result in a single circulation pattern. Therefore, the transition between the double circulation pattern of the non-constrained flow and the single circulation pattern occur at constrictions less than $\beta = 65\%$. Secondary flow velocities and shear rate along the vessel wall are much higher for the flow with an upstream constriction than those for the flow without an upstream constriction. In the presence of an upstream constriction, the axial velocity and secondary flow maximum velocity are of the same order of magnitude.

The results of the experiments with the asymmetric orifice show that the sense of rotation depends on the position of the upstream opening with respect to the central axis of the vessel. The clinical data show that the aortic valve opening, even at the full open stage, is less than the maximum diameter of the sinus of valsalva at the base of the human aorta by at least 30% which is equivalent to a stenosis ratio of $\beta = 51\%$. Therefore, our results are important in the understanding of the nature of shear stress development along the vessel walls and in the study of the radial distribution of blood cells in a secondary flow field. Similarly, for industrial application these results are important for the assessment of the transport properties in coiled heat exchangers or fluid-fluid absorption systems. In order to investigate the spatial condition which determines the sense of rotation in single-circulation patterns, a series of experiments were carried out changing the position of orifice opening in 45^0 increments with respect to anterior-posterior wall axis. These results strongly support the conjecture that the incoming jet impingement on the vessel wall is redirected by the local curvature of the vessel wall into a helical pattern which overcomes the Dean's flow and causes the single-circulation patterns.

To summarize, three distinct secondary flow patterns are observed in our experimental study. The first one is the known Dean flow, which is a double-circulation pattern. The second and third patterns, which are discovered for the first time, are the clockwise and counterclockwise single-circulation patterns. The transition from one

pattern to another is dependent on the spatial boundary conditions and is independent of the temporal boundary conditions. The secondary flow velocity gradient and hence its shear stress is comparable to the axial flow velocity gradient and shear stress in the single-circulation pattern. For the Dean flow or double-circulation secondary flow pattern, shear stress values are much less than those for the axial flow. This finding can greatly contribute to our understanding of blood flow-related pathology. In addition, the position of the upstream orifice opening with respect to the anterior-posterior vessel wall is an important factor in the design of artificial aortic valves. The dependence of the sense of the rotation of single-circulation patterns on the relative position of orifice opening with respect to the anterior-posterior vessel wall axis suggests that the out of plane curvature of aorta may play an important role in the re-direction of the incoming jet in the arch.

Contents

List of Figures

List of Tables

Chapter 1 Introduction

The main objective of this study is to understand the structure of the primary and secondary flows in curved vessels, the understanding of these secondary patterns is relevant to the flow in human arteries as well as to many applications in flows used in industrial systems.

1.1 Basic Features of the Flow in Curved Vessels

Systematic theoretical and experimental studies of flow in curved pipes started with the investigation of Thomson (1876, 1877) on the effect of curvature in open channel flows. In 1902, Williams *et al.*(1902) observed that the location of the maximum axial velocity is shifted towards the outer wall of a curved pipe. Later, Eustice (1910, 1911) demonstrated the existence of a secondary flow by injecting ink into water flowing through a coiled pipe. It has been long known that for steady flows the transition to turbulence for even slightly curved pipes occurs at a much higher Reynolds number than flow in straight tubes. Numerous investigators (*e.g.*, White 1929, Taylor 1929, and Adler 1934) have studied this empirical fact, but a conclusive explanation is still lacking (Coles 1981) and there has not been a fundamental breakthrough since then. The existence of secondary flows is another interesting phenomenon associated with the curvature effects. The existence of secondary flows is attributed to the physical fact that the fluid elements experience a variation in centrifugal force along their position in the arch. Knowledge of the pressure loss is essential for the design of pipe/pumping networks. As far as curved pipes are an indispensable part of most heat and mass transfer systems, a proper modeling of secondary flows is of crucial importance for calculating the transport coefficients in such systems. Steady flow in curved pipes was formulated and studied by Dean (1927). He derived the fundamental non-dimensional parameter which determines the nature of secondary flows in curved

pipes:the Dean number.

1.2 Formulation of the Problem and the Basic Dimensionless Flow Parameters

1.2.1 Steady Flow in a Curved Pipe

Steady flow in curved pipes was formulated and studied by W. R. Dean (1927). He defined the non-dimensional parameter De as:

$$De \equiv 2.\delta^{1/2} Re \tag{1.1}$$

where δ, defined as the ratio a/R, represents the relative curvature of the arch, as the main parameter in describing flows in curved pipes. This parameter incorporates the non-dimensional geometric factor, which represents the curvature of the vessel relative to the radius of the vessel itself, into the Reynolds number, which is the dynamical parameter. Figure 1.2 shows the geometry of the problem:a circular pipe with cross-sectional radius a coiled in a circle of radius R. The toroidal coordinate system (r', α, θ) shown in Figure 1.2, where r' denotes the radial coordinate in the cross-section of the pipe from the center of the cross-section, α the angle between the radius vector and the plane of symmetry, and θ the angular distance of the cross section from the beginning of the arch semi-circle. The three components of the velocity vector are (u', v', w'). The problem can be presented in the following dimensionless parameters

$$r = r'/a \quad s = R\theta/a \quad t = \bar{W}_0 t'/a \quad \mathbf{q} = \mathbf{q}'/\bar{W}_0 \quad p = p'/\rho \bar{W}_0{}^2 \tag{1.2}$$

Primes denote dimensional quantities, unprimed quantities are dimensionless, t is the time, $\mathbf{q} = (u, v, w)$, p is the pressure, ρ the density, and $\bar{W}_0$ the mean axial velocity in the pipe. The governing equations for flow in such a geometry are

continuity

$$u_r + \frac{u}{r}\frac{1+2\delta r\cos\alpha}{1+\delta r\cos\alpha} + \frac{v_\alpha}{r} - \frac{\delta v\sin\alpha}{1+\delta r\cos\alpha} + \frac{w_s}{1+\delta r\cos\alpha} = 0 \tag{1.3}$$

momentum in r direction (1.4)

$$\begin{aligned} u_r + uu_r + \frac{vu_\alpha}{r} + \frac{wu_s}{1+\delta r\cos\alpha} - \frac{v^2}{r} - \frac{\delta w^2\cos\alpha}{1+\delta r\cos\alpha} = \\ - p_r - \left(\frac{1}{Re}\right)\left(\frac{1}{r}\frac{\partial}{\partial\alpha} - \frac{\delta\sin\alpha}{1+\delta r\cos\alpha}\right)\left(v_r + \frac{v}{r} - \frac{u_\alpha}{r}\right) \\ - \left(\frac{1}{Re}\right)\left(\left(\frac{u_{ss}}{(1+\delta r\cos\alpha)^2}\right) + \frac{1}{1+\delta r\cos\alpha}\left(w_{rs} + \frac{\delta w_s\cos\alpha}{1+\delta\cos\alpha}\right)\right) \end{aligned}$$

momentum in α direction (1.5)

$$\begin{aligned} u_t + uu_r + \frac{vu_\alpha}{r} + \frac{wu_s}{1+\delta r\cos\alpha} - \frac{v^2}{r} - \frac{\delta w^2\cos\alpha}{1+\delta r\cos\alpha} = \\ - p_r - \left(\frac{1}{Re}\right)\left(\left(\frac{1}{r}\frac{\partial}{\partial\alpha} - \frac{\delta\sin\alpha}{1+\delta r\cos\alpha}\right)\left(v_r + \frac{v}{r} - \frac{u_\alpha}{r}\right)\right. \\ \left. - \left(\frac{1}{Re}\right)\left(\left(\frac{u_{ss}}{(1+\delta r\cos\alpha)^2}\right) + \frac{1}{1+\delta r\cos\alpha}\left(w_{rs} + \frac{\delta w_s\cos\alpha}{1+\delta\cos\alpha}\right)\right)\right. \end{aligned}$$

momentum in s direction (1.6)

$$\begin{aligned} w_t + uw_r + \frac{\delta uw\cos\alpha}{1+\delta r\cos\alpha} + \frac{vw_\alpha}{r} - \frac{\delta vw\sin\alpha}{1+\delta r\cos\alpha} + \frac{ww_s}{1+\delta r\cos\alpha} = \\ - \frac{p_s}{1+\delta r\cos\alpha} + \frac{1}{Re}\left(\left(\frac{\partial}{\partial r} + \frac{1}{r}\right)\left(w_r + \frac{\delta w\cos\alpha}{1+\delta r\cos\alpha}\right) + \frac{w_{\alpha\alpha}}{r^2}\right) \\ - \left(\frac{1}{Re}\right)\left(\frac{1}{r}\frac{\partial}{\partial\alpha}\left(\frac{\delta w\sin\alpha}{1+\delta r\cos\alpha}\right) - \left(\frac{\partial}{\partial r} + \frac{1}{r}\right)\frac{u_s}{1+\delta r\cos\alpha} - \frac{1}{r}\frac{\partial}{\partial\alpha}\left(\frac{v_s}{1+\delta r\cos\alpha}\right)\right) \end{aligned}$$

(subscripts denote derivatives) where the curvature ratio is

$$\delta = \frac{a}{R} \tag{1.7}$$

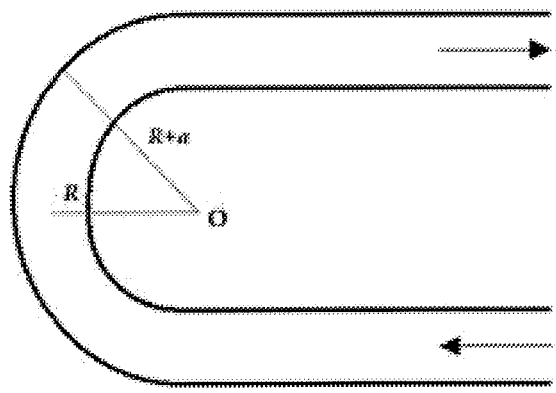

Figure 1.1: Longitudinal schematic of the curved pipe problem. Point O is the center of the arch circle, R is the average arch radius and a is the radius of the tube cross section.

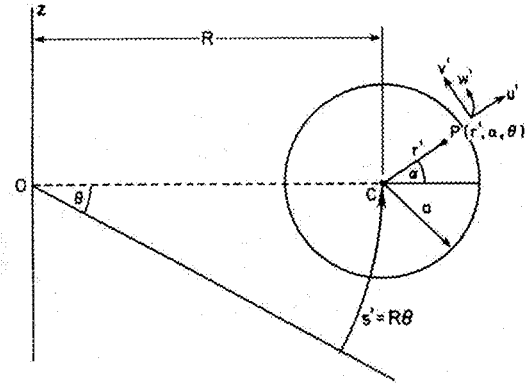

Figure 1.2: Geometrical configuration of the curved pipe problem in a toroidal coordinate system. Point O is the center of the arch circle, R is the average arch radius, and a is the radius of the tube cross section.

and the Reynolds number is

$$Re = \frac{a\bar{W}_0}{\nu} \tag{1.8}$$

As Berger *et al.* (1983) have pointed out, nearly all of the analysis of the above equations are based on the following entry conditions:

- constant total pressure across the entrance cross section
- constant injection velocity
- fully developed Poiseuille flow.

These equations and boundary conditions combined with the no-slip condition

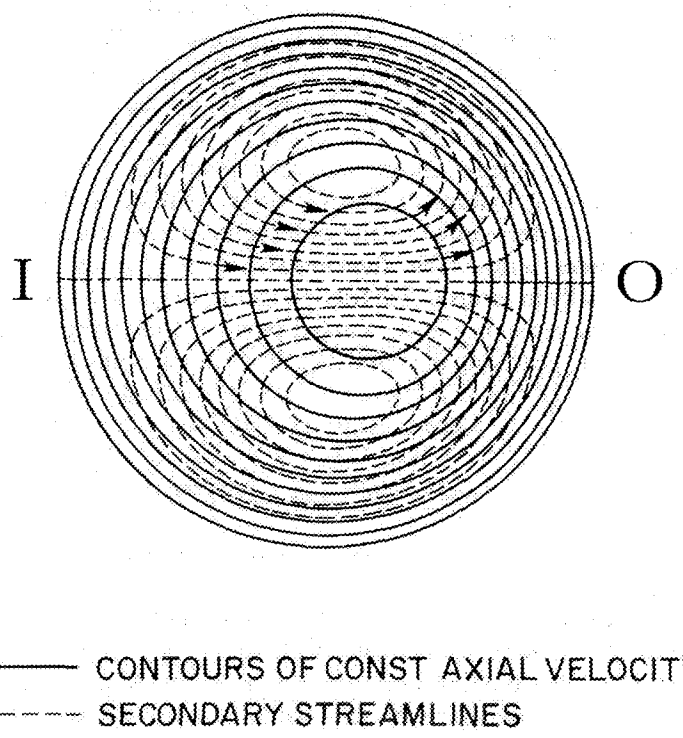

Figure 1.3: A typical secondary flow pattern for steady flow through a curved pipe. Dean (1927). $De = 96$.

at the wall give the complete governing equations, the solution of which would give the flow field in the curved vessel. Figure 1.3 shows the secondary flow patterns as obtained by solving the linear approximation of the equations of motion by Dean (1927). Dean solved the problem by expanding the solution in term of a polynomial series in powers of the Dean number. Figure 1.3 shows the streamlines and the flow field for a steady flow through a curved vessel as calculated from Dean's solution. The symmetry with respect to the axial plane seems to be a natural consequence of geometrical symmetry. This assumption would be analyzed in more detail later on. The effect of the Dean number on the structure of the secondary flow is apparent from the results for two different Dean numbers in Figure 1.4.

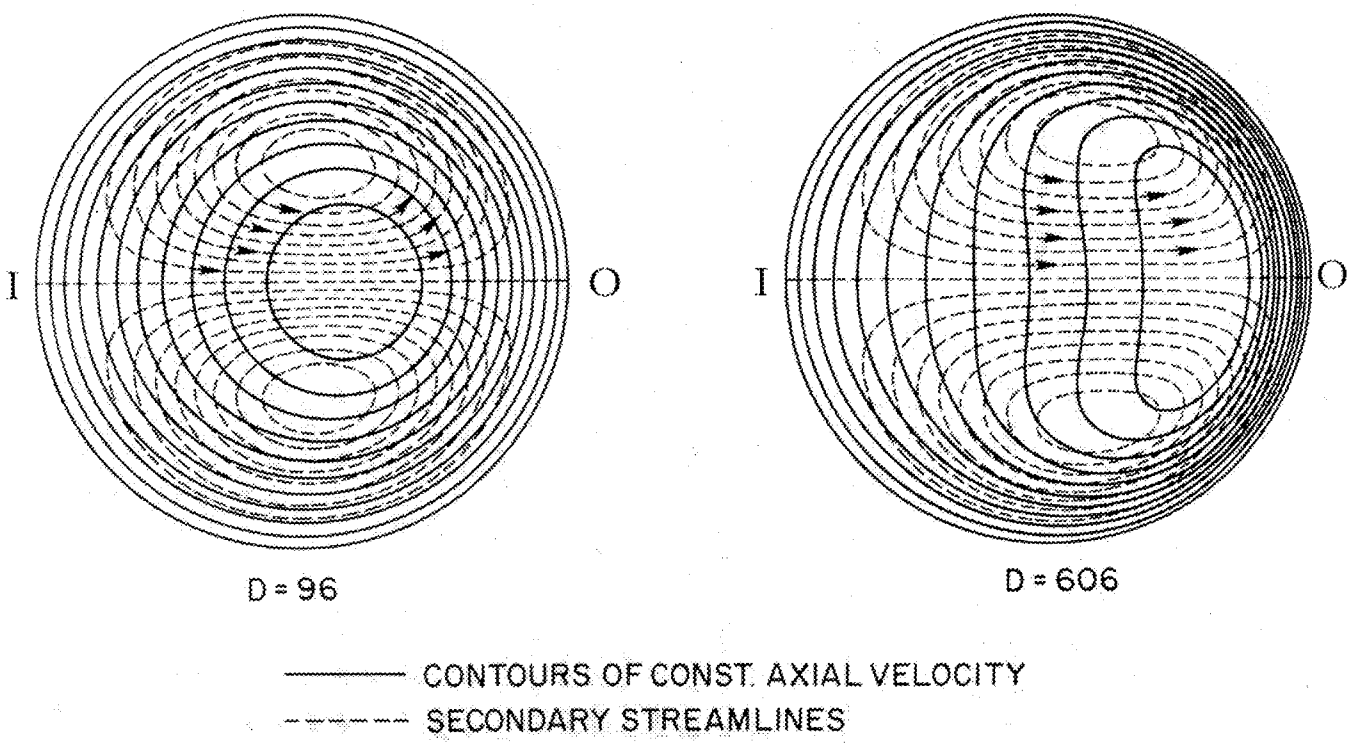

Figure 1.4: Secondary flow pattern for the steady flow through a 180-degree curved vessel. The effect of the Dean number on secondary flow pattern can be seen from comparison of the left side flow at $De = 96$ and the right side at $De = 606$.

1.2.2 Pulsatile Flow in a Curved Pipe

After the initial studies on steady flows by Dean (1927, 1928), thirty year later, Womersley (1957) tackled the question of time periodicity on the laminar flow development in curved and elastic pipes. He used a simplified flow model based on the linearization of the pulsatile flow in the form of a sinusoidal wave superimposed on a non-zero mean (Womersley, 1957). The non-dimensional parameter (Womersley number) is defined as:

$$\alpha \equiv R\sqrt{(\omega/\nu)} \tag{1.9}$$

or

$\alpha \equiv R\sqrt{(\omega.\rho/\mu)}$

Where

$R = Vessel\ \ Radius$

$\mu = Dynamic\ \ Viscosity$

$\rho = Density$

$\omega = Frequency$

Womersley applied his linear analysis to a straight tube with a pulsatile flow in the form of a simple sinusoidal wave. The Womersley parameter can be considered a Reynolds number for oscillatory flows, the numerator being the oscillating inertial force and the denominator being the viscous force. It represents the kinematic similarities in oscillatory fluid motion. It should be noted that Witzig (1914) in his doctoral thesis had actually calculated the velocity profiles, in reference to arterial flow at values of $\alpha = 4.0$ and $\alpha = 10$, but his work was not known until cited by Lambossy (1952). Both Lambossy and Witzig had calculated the velocity profiles for values relevant to the blood circulation, but for various reasons their results remained unknown until Womersley attacked this problem again. The systematic study of the combined effect of the pulsation and the curvature on the flow in circular pipes was the next step which various researchers worked on in the 1970s, both theoretically (Yao & Berger (1975) and Zalosh *et al.* (1975))—, and experimentally (Agrawal *et*

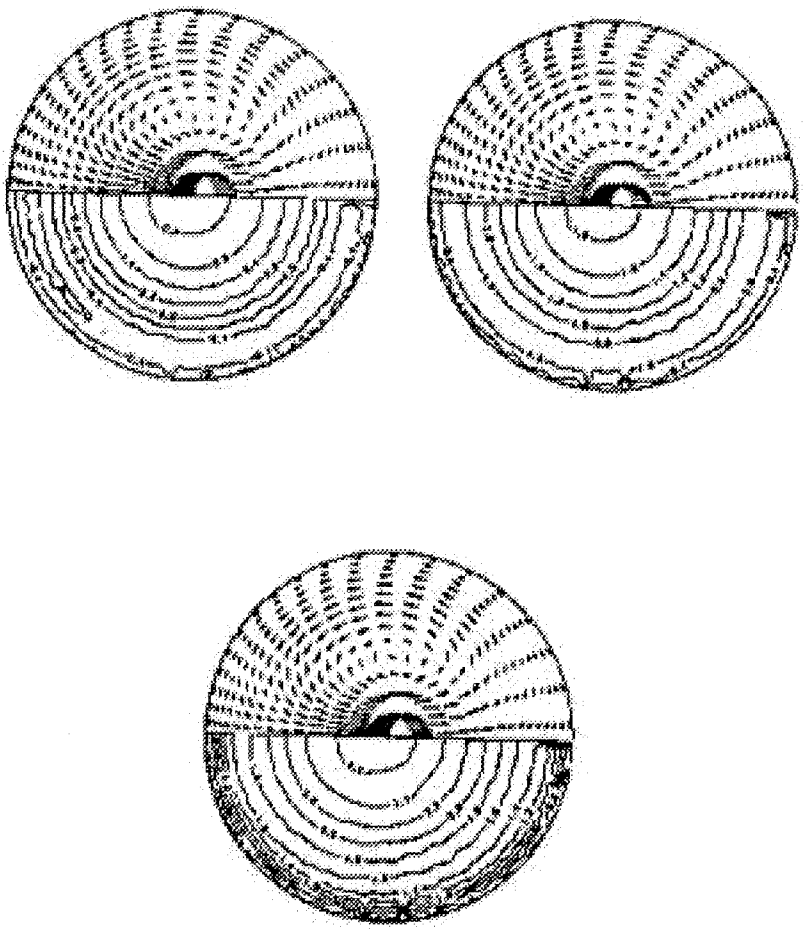

Figure 1.5: Secondary flow pattern for the pulsatile flow through a 180-degree curved vessel. from Hamakiotes & Berger (1988, 1990).

al. 1978). The results of Hamakiotes and Berger (1988) are the most celebrated simulations of pulsatile flow in curved pipes. Figure 1.5 shows a typical result for the secondary flow patterns from direct numerical simulation of pulsatile flow through a curved vessel by Hamakiotes and Berger (1988). The Dean numbers for these cases are close to the physiological values and the Womersley number corresponds to a frequency of $1 - 3HZ$.

The structural resemblance between pulsatile and steady flow, in terms of a double-circulation pattern is obvious. With minor differences it shows that the secondary flow is symmetrical with respect to the axial plane. Because of the symmetry with respect to the central plane, Hamakiotes and Berger (1990) have used the same symmetry plane to show the velocity vector field and the vorticity contour plot in

the same figure. These results have been used extensively for modeling aortic flow and obtaining the shear stress values along the vessel walls (Tada *et al.* 1996). The results of Hamakiotes and Berger (1990) have been obtained for a non-constrained fully developed entrance velocity profile. Such a condition for the upstream flow is not a realistic physiological condition. In reality, flow enters the aortic arch through the opening of the aortic valve, which at best has an opening diameter slightly less than that of the aorta. With aging and natural diseases, the opening of the aortic valve shrinks in size and this causes considerable constriction of the flow passage. Therefore, one can expect a flow ejection during systole with a flat velocity profile into the aorta. In this respect and to our best knowledge, no previous studies have considered the impact of such a non-parabolic, impulsive upstream flow condition on the secondary flow patterns in curved pipe flow. Since we have obtained the double-circulation for a non-parabolic upstream profile, we conjecture that the presence of a single-circulation pattern does not depend on the shape of the upstream velocity profile. Rather, we conclude from our results that the upstream constriction is the determining factor in secondary flow patterns in curved pipes. In the present study, we focus on this issue and try to design a series of systematic experiments to determine when the transition from a double-circulation pattern to a single-circulation pattern occurs.

1.3 Physiological Applications and the Effects of the Initial Constriction

In biofluid dynamics the issue of secondary flows arises again since the blood delivery system is composed mainly of curved vessels. For physiological applications, the proper understanding of such flows is required not only for mapping the flow hemodynamics but also for determining the shear stress values alongside the vessel walls. This is important in understanding phenomena such as atherosclerosis and atherostenosis, which depend on the filtration properties through the endothelial vessel linings and

the precipitation of large lipoproteins in this region. The largest vessel in the human body, which is responsible for delivering blood to the whole body, is aorta, which is highly curved. Therefore, many physiologists are interested in knowing the physics of the fluid flow in curved vessels and its relation to certain aortic diseases such as atherosclerosis and atherostenosis. Since flow in large arteries is pulsatile, another challenge arises in the study of the effect of pulsation on the flow in the curved pipes. This effect is also important in industrial applications when reciprocating pumps deliver flow in a pulsatile manner. Womersley (1957) tackled the question of time periodicity on the laminar flow development in curved and elastic pipes. He used a simplified flow model based on the linearization of the pulsatile flow in the form of a sinusoidal wave superimposed on a non-zero mean. The study of the pulsatile flow of a viscous fluid in a curved vessel is a step towards the simulation of the blood flow at curvature sites, which are common in arterial and venous flow systems. For such flows an understanding of the distribution of velocities, shear stresses and pressure will help to provide some insight into the origin of arterial diseases. Curvature sites have been associated with the onset of atherosclerosis (Wolstraholme & Knight, 1973), which is one of the primary causes of circulatory failure. Lesions are distributed non-uniformly around the surface of arteries, being found more commonly near bifurcation sites, on the inner wall of the curves, and in larger arteries. The regions where lesions tend to develop are closely correlated with areas of the wall in which the endothelial cells are found experimentally to have a relatively low permeability to large molecules such as lipoproteins, which are known to be implicated in the generation of lesions. However, the role of wall shear rate on this phenomenon is a matter of controversy among different researchers.

One of the main controversies is whether low or high shear rate is favorable from a physiological point of view. The vascular endothelium, by virtue of its position at the interface between the blood and the vessel wall, is known to play a critical role in the control of thrombosis and fibrinolysis. Thrombomodulin (TM) is a surface receptor that binds thrombin and is a potent activator of the protein C anticoagulant pathway. Although TM expression is known to be regulated by various cytokines, little is known

about its response to ever-present biomechanical stimuli. Following Lighthill (1975), a school of thought has emerged attributing this to a relatively low shear rate. Detailed patterns of wall shear rate and the stress associated with the flow may play a role in atherogenesis. The secondary flows induced by the centrifugal effects developed at the curvature sites will result in asymmetrical wall stresses with a high-shear region and a low-pressure region. Texon (1986) and Chandran (1974) postulate that a suction effect in the low-pressure region causes the incipient atheroma. Another school of thought following Fry (1968) claims that high shear stress might damage the endothelial linings of the blood vessels and arterial walls, which can foster the development of atherogenesis. Caro et al. (1971), on the other hand, associate the natural causes of the incipient atheroma with a low-shear region and justify this claim by proposing a shear-dependent mass transfer mechanism for filtration function of endothelial lining of arterial vessel walls. More recently, Malek *et al.*(1994) have explored the role of fluid shear stress, imparted on the luminal surface of the endothelial cell as a result of blood flow, on the expression of TM mRNA and protein in both bovine aortic endothelial (BAE) and bovine smooth muscle (BSM) cells in an *in vitro* system. They claim that TM expression is regulated by flow. They observed that subjecting BAE cells to fluid shear stress in the physiological range of magnitude of 15 (moderate shear stress) and 36 (elevated shear stress) $dynes/cm^2$ resulted in a mild transient increase followed by a significant decrease in TM mRNA to 37% and 16% of its resting level, respectively, by 9 hours after the onset of flow. In contrast they found that shear stress at the low magnitude of 4 $dynes/cm^2$ did not affect TM mRNA levels. They found that the sensitivity of TM mRNA expression by flow is specific to endothelium, since it was not observed in BSM cells exposed to steady laminar shear stress of 15 $dynes/cm^2$. Furthermore, unlike BAE cells, BSM cells do not exhibit altered cell shape nor align in the direction of flow after 24 hours of shear stress at 15 $dynes/cm^2$. Malek *et al.*(1999), in a more recent study, claim that the change of direction of the shear stress applied to the endothelial linings of the blood vessels has an unfavorable effect on the function of the vascular endothelium and is more important than the absolute value of the shear stress itself.

Obviously, a better knowledge of the flow field including the velocity, vorticity, pressure and shear stress distributions is essential to a better understanding of the origin of some common fatal diseases and possible ways of overcoming them. This knowledge is also indispensable to the designers of artificial organs in optimizing their design for the flow delivery without damaging the vessel walls or affecting the filtration and transport functions of them. The aorta is the major blood vessel transporting blood pumped by the left ventricle to the systemic circulation. The tricuspid aortic valve at the root of the aorta provides a centralized flow with nearly uniform velocity profile into the ascending aorta. The aorta consisting of the ascending limb, the aortic arch, and the descending segment is a vessel of complex geometry including curvature in multiple planes, branches and taper. The understanding of the development of blood flow in this distensible vessel has been the subject of several theoretical as well as experimental investigations. Flow development in the aorta and in the branch vessels has been of interest in delineating the role of wall shear stresses on the etiology of atherosclerosis. The current status of our understanding of the complex flow dynamics in the aorta is far from conclusive. With the advent of transesophageal echocardiography and magnetic resonance velocity mapping, further evidence of the presence of secondary flows in even the descending aorta has been reported. The importance of the effect of secondary flow in the descending aorta on the perfusion of distal blood vessels (such as superior mesenteric and renal arterial branches) as well as in the iliac bifurcation are topics of current interest. Caro et al. (1996) have extended the usage of Magnetic Resonance Imaging to examine the geometry of arterial curvature and branching in casts and *in vivo*, and to measure the distribution of axial velocity in the associated flow. They have found that, contrary to a widely held view, that the geometry is commonly non-planar. Moreover, relatively small values of the parameters which render the geometry non-planar appear to affect significantly the velocity distribution. The findings suggest that non-planarity is an important factor influencing arterial flows, including wall shear.

Many investigators have made insight into the fluid dynamics of curved tubes with a particular interest in understanding of the blood flow characteristics in the

aortic arch (Berger et al. 1983). However, concerning this physiological application, only a few of them (Pedley 1980), Chandran and Yearwood (1979)-(1984), Chang and Tarbell (1985) and Rindt et al. (1991)-(1996) have considered physiological pressure gradient or flow boundary conditions in their experiments or numerical simulations. Swanson *et al.*(1993) have tried to study experimentally the oscillatory flow through a 180-degrees curved tube applying a flow rate which is constrained to vary sinusoidally about a non-zero mean at a specified period T, and mean flow rate Q. Though this study is valuable in some industrial applications, it neglects the important temporal characteristics of the physiological flows, and using its results for estimating flow characteristics in human arteries is far from justified. More recently, Wood (1999) has tried to study the entrance effects in steady and unsteady pipe flow and compared and contrasted them, but his study is more concentrating on presenting how Stokes' first and second problems illustrate key aspects of unsteady viscous diffusion and boundary layers in the circulation. The nature of primary and secondary flow in curved vessels is untouched in his work. In the present work, we will place a particular emphasis on the sensitivity of the secondary flow to time and spatial boundary conditions that may be found in physiological situations.

Zabielski & Mestel (1998) investigated fully developed flow in a helical pipe with a view to modeling blood flow around the commonly non-planar bends in the arterial system. They claimed that medical research suggests that the formation of atherosclerotic lesions is strongly correlated with regions of low wall shear and it has been suggested that the observed non-planar geometry may result in a more uniform shear distribution. They studied helical flows driven by an oscillating pressure gradient analytically and numerically. They were able to derive an expression in the high-frequency limit for the second-order steady flow driven by streaming from the Stokes layers. Although they used finite difference methods to calculate flows driven by sinusoidal or physiological pressure gradients in various geometries, still they were limited by the fully-developed flow assumption. They suggested the advantage of the observed helical rather than planar arterial bends in terms of wall shear distribution and the inhibition of boundary-layer separation. They have studied both steady and

unsteady flow patterns and supported the Dean flow axisymmetric structure. As Chen et al. (1992) have noted, a new non-dimensional parameter which is a measure of torsion enters into the formulation of this problem. Ishigaki (1994) derived an analogy between the secondary flow of a viscous fluid, caused by the Coriolis force, through a straight pipe rotating about an axis perpendicular to the pipe axis, to the flow of a fluid, caused by the centrifugal force, through a stationary curved pipe. He demonstrated the quantitative analogy between these two fully developed laminar flows through similarity arguments, computational studies and the use of experimental data. Similarity considerations result in two analogous governing parameters for each flow, which include a new one for the rotating flow. When one of these analogous pairs of parameters of the two flows is large, Ishigaki demonstrated that there are strong similarities between the two flows regarding friction factors, heat transfer rates, flow patterns and flow properties for the same values of the other pair of parameters.

Another application of oscillatory flows in curved vessels is flow through airways in the respiratory system. Sharp *et al.*(1991) studied these types of flows experimentally and analytically. In their results again only one structure for the secondary flows is presented which is the Dean double-circulation pattern.

Pedrizzetti (1996) is one of the first researchers who systematically attacked this problem with a view to the spatial geometry of ascending aorta. He studied analytically and in detail the unsteady flow in a circular conduit with a smooth expansion by numerically integrating the equation of motion in the axisymmetric approximation. In his model the values of governing parameters were chosen such that to be relevant to medical problems, while the geometry corresponded to a scenario of post-surgical conditions. The flow determined by an oscillatory volume was characterized by a sequence of vortex rings moving in the expanded part of the tube. The development of wall shear stress was found to be governed by the separated translating vorticity which induced an evolving band of large intensity for about a complete oscillation cycle. This factor influences the dynamics of unsteady separation whose space-time development reveals features of some generality which he tried to classify. The time

variation of the pressure jump was found to be dominated by inertial effects. He has also investigated systematically the dependence of the flow on the dimensionless parameters in great detail. Pedrizzetti has demonstrated the relevance of these results to physiological applications quantitatively by simulating the flow induced by a pulsatile flow rate.

1.3.1 Effect of the Upstream Boundary Condition

The studies reported in section 1.2 are all done using an upstream boundary condition of either a fully developed velocity profile or a flat velocity profile, none of which simulate the physiological conditions in the human aorta. In our work, the main idea for the design, which resulted in the discovery of new secondary flow patterns in curved vessels, was inspired because of the anatomy of the human ascending aorta. At the beginning of the ascending aorta, we see a bulging structure called the Sinus of Valsalva. The reason for the existence of this cavity is that, because of the watertight lining of the heart (the endocardium) and the thickness of the myocardium, the heart cannot depend on the blood contained in its own chambers for oxygen and nourishment. It possesses a vascular system of its own, called the coronary arterial system. In the most common distribution, this comprises two major coronary arteries, the right and the left. Normally, the left coronary artery divides soon after its origin into two major branches, called the left anterior descending and the circumflex coronary arteries. The right, the left anterior descending, and the left circumflex coronary arteries have many branches and are of almost equal importance. Thus, there are commonly said to be three main functional coronary arteries rather than two. The right and left coronary arteries originate from the right and left aortic sinuses (the Sinuses of Valsalva), which are bulges at the origin of the ascending aorta immediately beyond, or distal to, the aortic valve. The ostium, or opening, of the right coronary artery is in the right aortic sinus and that of the left coronary artery is in the left aortic sinus, just above the aortic valve ring. There is also a non-coronary sinus of Valsalva, which lies to the left and posteriorly at the origin of the ascending aorta. The left

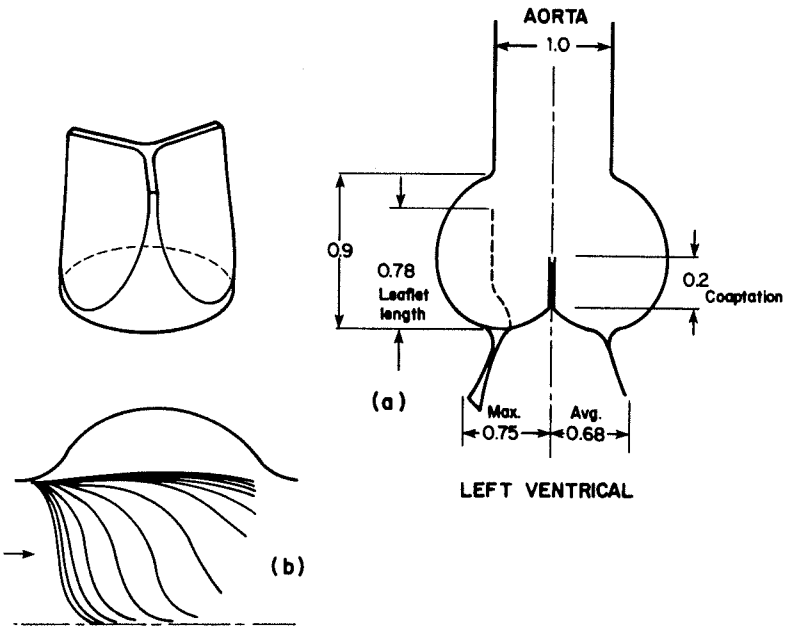

Figure 1.6: The geometry of the aortic valve, the sinus of valsalva and the ascending aorta. from Chandran (1992).

coronary arterial system is more important than the right because it supplies blood to the larger left ventricle, and because the dimension of the left coronary ostium is larger than that of the right. The existence of the aortic valve and also the Sinus of valsalva at the beginning of the aorta represents a drastically different initial condition and boundary condition than the idealized studies of Hamakiotes and Berger (1990) and others for a fully-developed entry velocity profile. A common path which has been followed in most of the previous studies on flow in curved vessels. Figure 1.6 shows the geometry of the ascending aorta and its relative dimensions. The aortic valve orifice opens to the cavity of the Sinus of Valsalva. This prompted us to think that there can be two possible scenarios which have not been considered in previous studies. These possibilities are:

- Separation of flow in steady case
- Vortex ring formation in pulsatile case

The mean diameter of the Sinus of Valsalva in human beings is about 50% larger than the maximum opening diameter of the aortic valve. Therefore, it seems relevant

that the effect of this cavity be incorporated into the study of the flow in aortic arch. Surprisingly, the researchers on aortic flow have not considered this factor in their studies. The current work stresses this factor and tries to study its effect on the flow in the aorta.

1.4 Objectives and Outline of the Current Work

To study the structure of the primary and the secondary flows in a curved vessel, with a view to aortic flow, an experimental set up consisting of a U-shaped pipe was designed to simulate physiological pulsatile flow conditions. Two types of flow motion have been implemented, a gravity-driven steady flow under a constant head reservoir, and a pulsatile flow using a pulsatile pump with characteristics close to those of human cardiac flows. Using Digital Particle Image Velocimetry (DPIV), quantitative flow measurements were performed in several cross sections along the 180-degree bend. From the analysis of these global flow measurements, it appears that the secondary flow pattern is highly dependent on the temporal and initial spatial boundary conditions. Our results indicate that the double vortex structure, which is the main characteristic of Dean flow, does not exist for constrained upstream entrance conditions—which is the characteristic of physiological conditions during cardiac systole. Instead, a single circulation pattern dominates the secondary flow for the constrained cases. From an analytical point of view our results indicate the non-uniqueness of the double vortex pattern. This possibility has been theoretically postulated by Pedley (1980).

For similar values of the frequency parameter—Womersley number α— and Dean number De, the marked differences between constrained and non-constrained initial conditions in the secondary patterns lead to very different shear stress distributions along the vessel wall for physiological applications.

The experimental study in the current work is divided into three stages: First, flow in the aortic arch model was studied without any upstream constriction. To understand the effect of entrance condition, we first studied flow in a curved pipe

similar to the conditions that Berger *et al.* had used in their studies. This provided us with a reference flow standard. Then, an orifice with an opening diameter less than half of the pipe diameter was mounted symmetrically at the entrance of the arch model. The results of this stage showed a difference between secondary flow structures and the transition from a double circulation pattern to a single circulation pattern. The latter pattern had not been observed before. In addition, while for the Dean type of secondary flows the primary flow shear stress on the vessel walls is about one order of magnitude higher than the wall shear rate because of the secondary flows, for the single-circulation patterns the primary and the secondary flows exert about the same amount of shear stress on the vessel walls.

To further elucidate the nature of the secondary flow patterns, based on the results of the first stage, the following studies were carried out:

- Designing an *in vitro* model which allowed reducing the size of the constriction to determine when the transition from double-circulation to single-circulation starts

- Designing a model with an asymmetric constriction in different angular and radial positions to determine the onset of the transition between clockwise and counterclockwise circulation and also the factors responsible for the sense of rotation of the circulatory patterns

- Carrying the same experiments with models with different sizes and curvature ratios in order to investigate the universality of the single circulation pattern for the secondary flows

In the second stage of this study orifices with different opening diameters were used to study where the aforementioned transition occurs. In the final stage, an orifice with an asymmetric opening was used to determine whether the sense of the rotation depends on the radial position of the constriction. By mounting different orifices in various positions at the entrance of the arch, we varied considerably the entrance flow condition, and studied its impact on the downstream flow field. This impact is

important because it elucidates the possible effect of the aortic valve and the Sinus of Valsalva on the flow in the aorta. An important motive for this approach is that the majority of the medical literature lacks any substantial evidence for the existence of the double circulation pattern. The very fact that the boundary conditions used for solving the equations of motion in curved vessels do not conform to the reality of the physiological characteristics of the aortic flow is another incentive to investigate the effect of this factor.

The objective behind this thesis was to develop a physical understanding of the aforementioned issues by conducting systematic experiments to elucidate the following factors in three distinct secondary flow patterns which have been experimentally observed or discovered in this study:

- The nature of the secondary flow in curved pipes under various boundary conditions, both spatial and temporal
- The effect of periodic flow conditions
- The combined effect of various spatial and temporal flow conditions—position of constriction, size of constriction and the effect of its angular position on the direction of secondary circulatory patterns
- The factors determining the secondary flow patterns and their structure, including the sense of rotation for circulatory patterns
- The transition threshold from double-circulation to single-circulation pattern
- The change in the values of the wall shear stress and Reynolds stress in different secondary flow patterns and to analyze the effects of circulatory patterns on the wall shear stress and turbulent Reynolds stresses in curved vessels

Chapter 2 Experimental Setup

In this chapter we explain the experimental design and setup used to model the flow in a 180-degree curved pipe with a view to aortic dimensions.

2.1 The Curved Vessel Model

A glass model of a 180-degree curved vessel was designed with the dimensions about the size of the human aorta. The inside diameter of the glass tube was 30 mm and the radius of arch curvature was 80 mm. This corresponds to a curvature ratio ($\delta = a/R$) of 0.27 and a Dean number of 2000-7000 depending on the flow rate, which is close to the range for aortic flow. In order to eliminate the turbulent irregular structures before entering the test region, at the beginning of the model a structure was provided for holding honeycomb eddy breakers. Figure 2.1 shows the arch model used for the experiment. Figure 2.2 shows how the position of the orifice at the entrance and its opening diameter were varied in order to simulate different upstream boundary conditions in aortic flow. The stenosis ratio, β, is defined as:

$$\beta = 1 - \frac{A_o}{A_t} \tag{2.1}$$

where A_o is the opening area and A_t is the total cross-sectional area of the vessel(Figure 2.3)

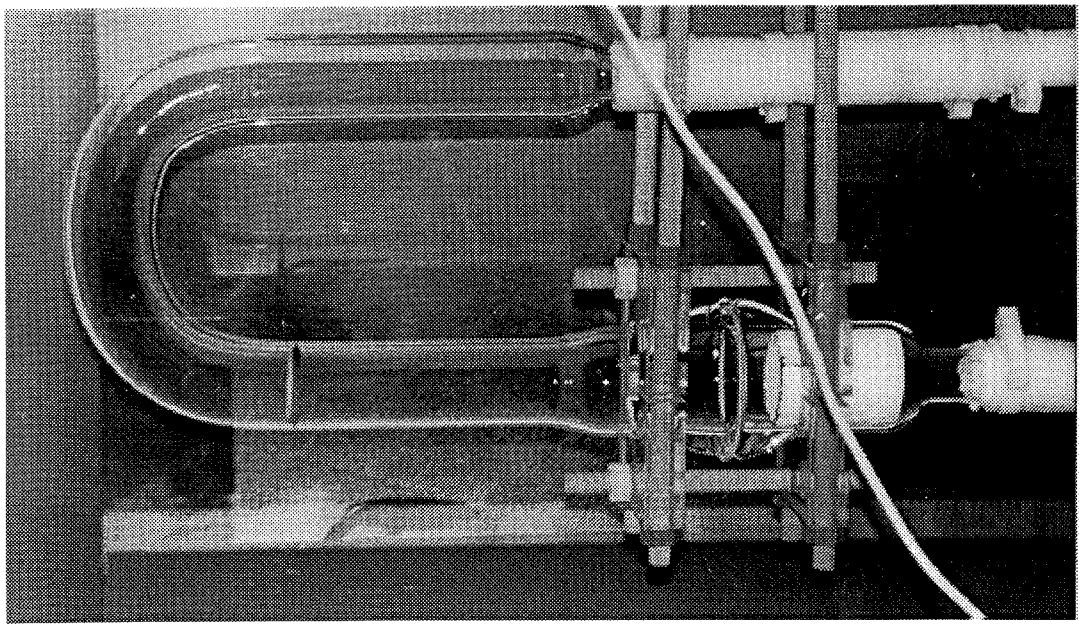

Figure 2.1: The arch model.

2.2 Steady Flow Apparatus

To provide steady flow with minimum incoming disturbance, a steady flow was provided using an overhead chamber with a constant fluid level. The overflow of this chamber would return to the main reservoir. Figure 2.6 shows the schematic and the configuration of this system. Figure 2.7 shows the dimensions of the system.

2.3 Pulsatile Flow

The setup for the pulsatile flow experiment is shown in Figure 2.8. A pulsatile pump of the Harvard type shown in Figure 2.9, which is typically used to replace the heart function during the heart surgery was used to provide the pulsatile flow to the system. Both the stroke volume and the frequency were adjustable on this device. It also made possible changing the systolic to diastolic ratio during the pumping, which in our experiment was kept constant at a physiologically normal level of thirty five percent. The following picture shows this device and its controls. The flow rate could be changed both by increasing the stroke volume and by changing the frequency of the pulsation. In accordance with the main body of literature, in order to simulate

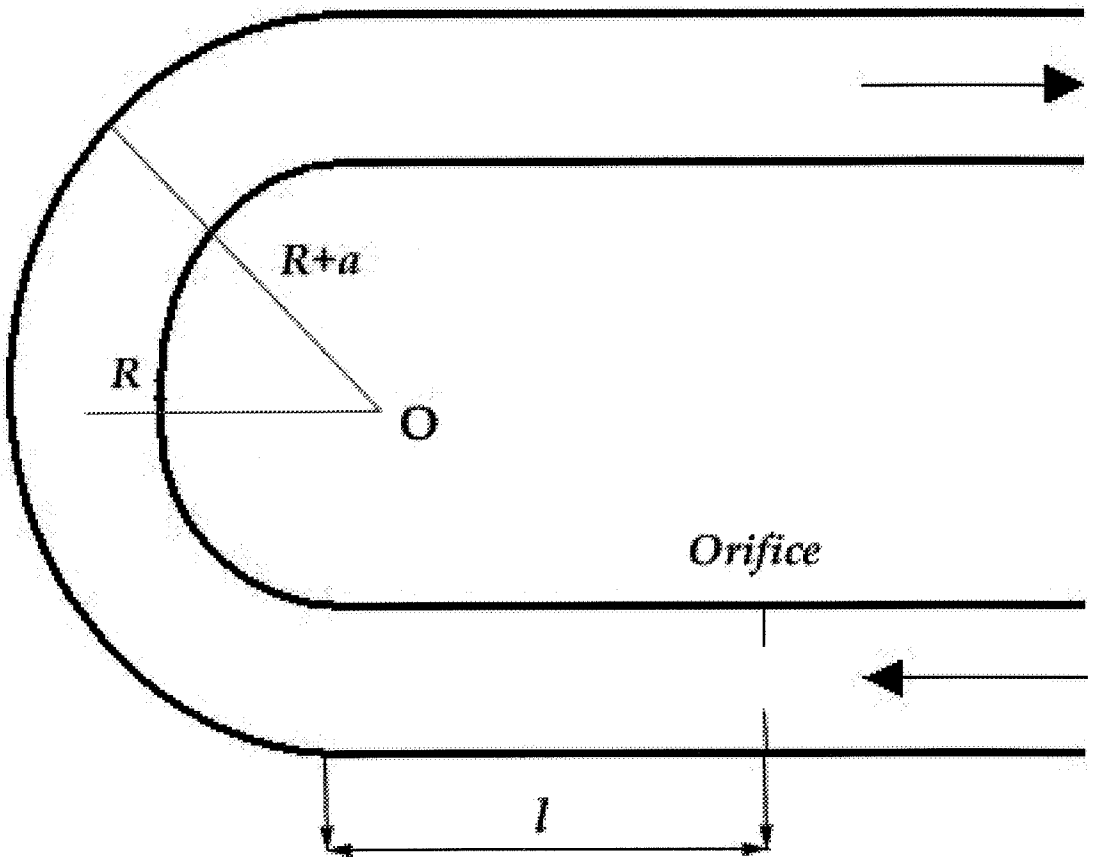

Figure 2.2: The schematic of the arch model. This figure shows the upstream orifice used for simulating the constricted flow. The distance l and the diameter of the orifice as well as the angular position of the constriction can be varied to simulate different flow conditions. For the non-constrained flow, the orifice is removed.

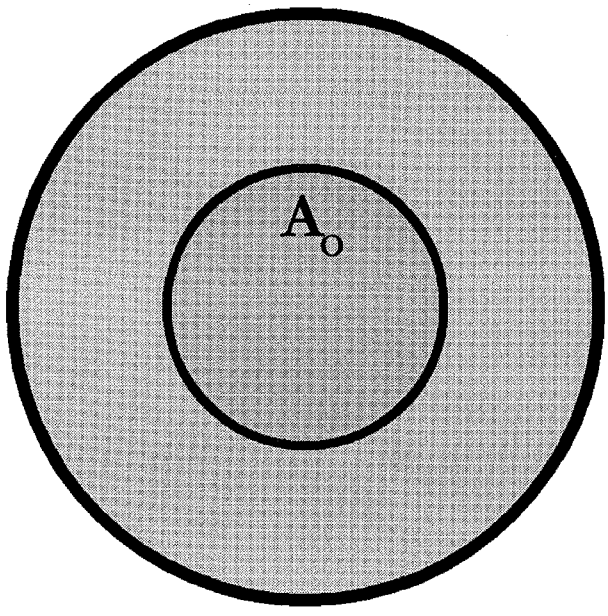

Figure 2.3: The orifice opening has an area of A_o.

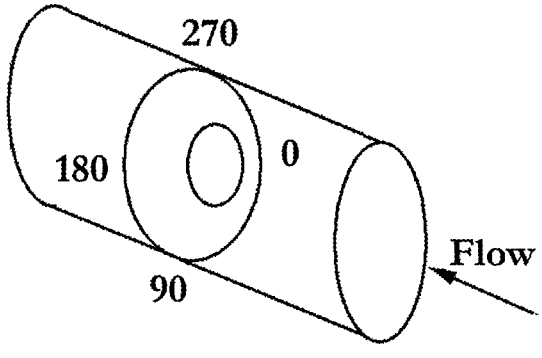

Figure 2.4: The schematic of the arch model with the orifice which has an asymmetric opening.

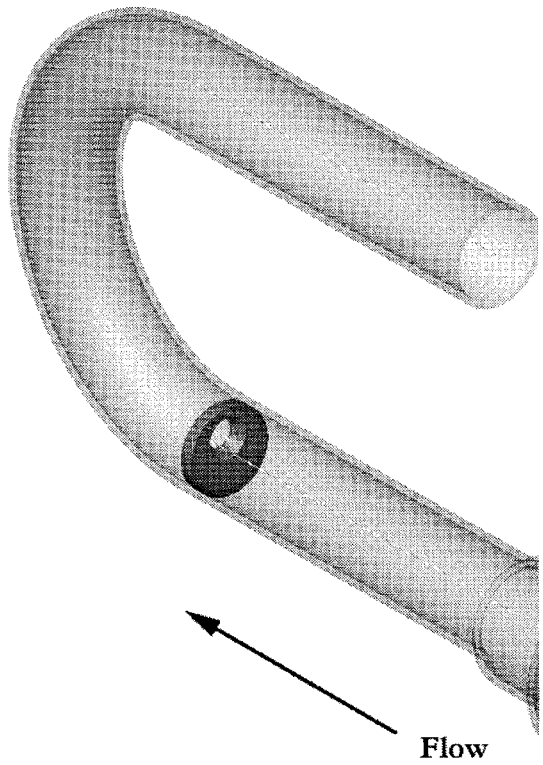

Figure 2.5: The three dimensional view of the arch model with the assymetric constriction.

the actual physiological condition, which uses the change in the heart beat during the physical exercise, we used the same method for our experiment.

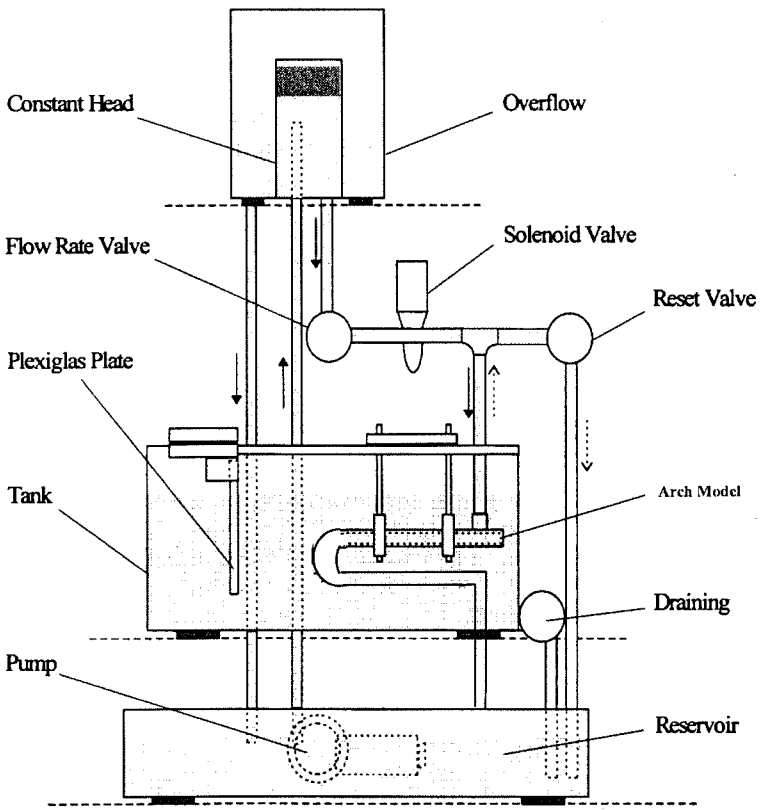

Figure 2.6: The configuration of the steady flow apparatus.

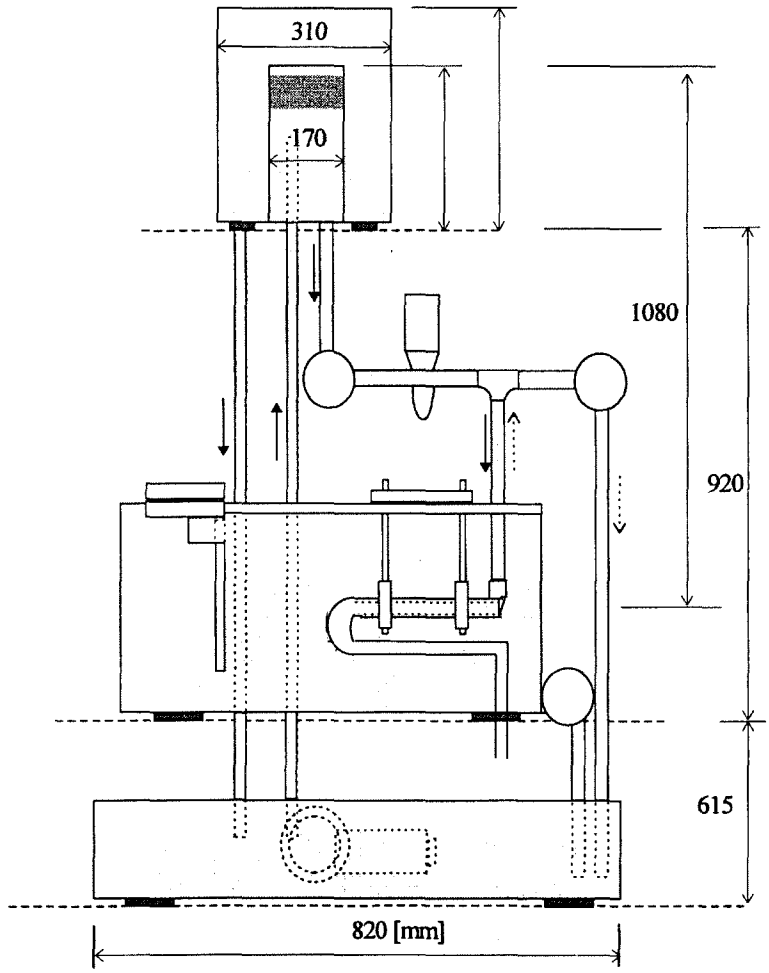

Figure 2.7: The dimensions of the steady flow apparatus.

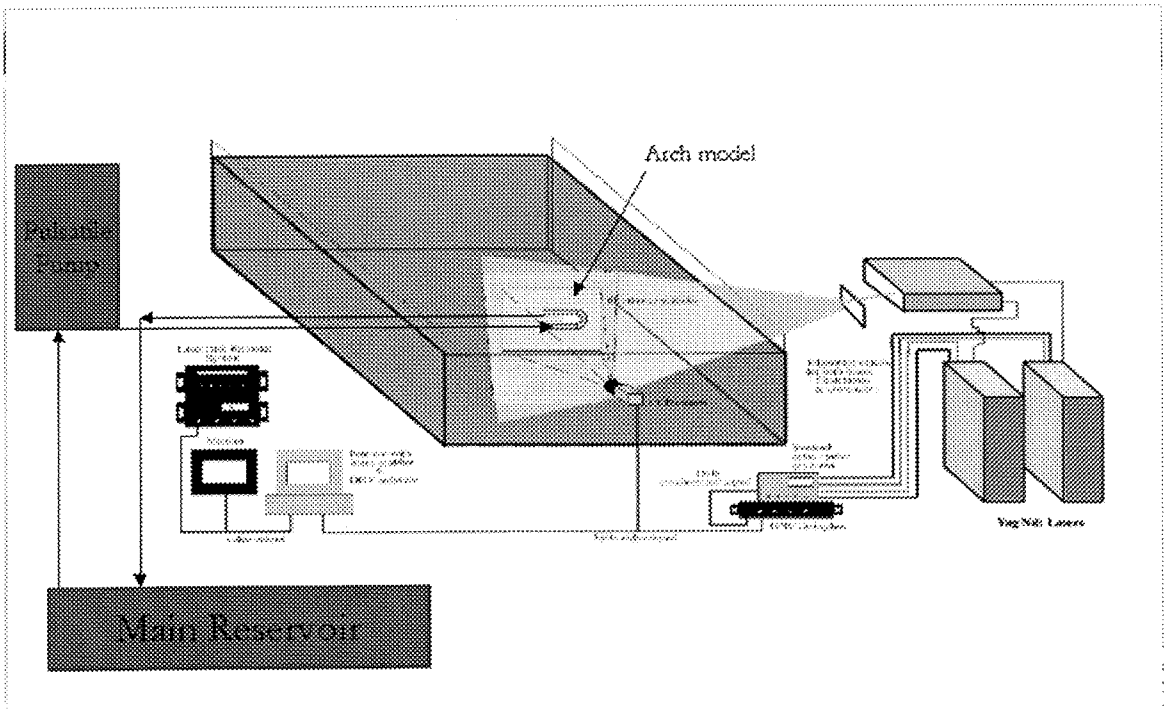

Figure 2.8: The setup for the pulsatile flow.

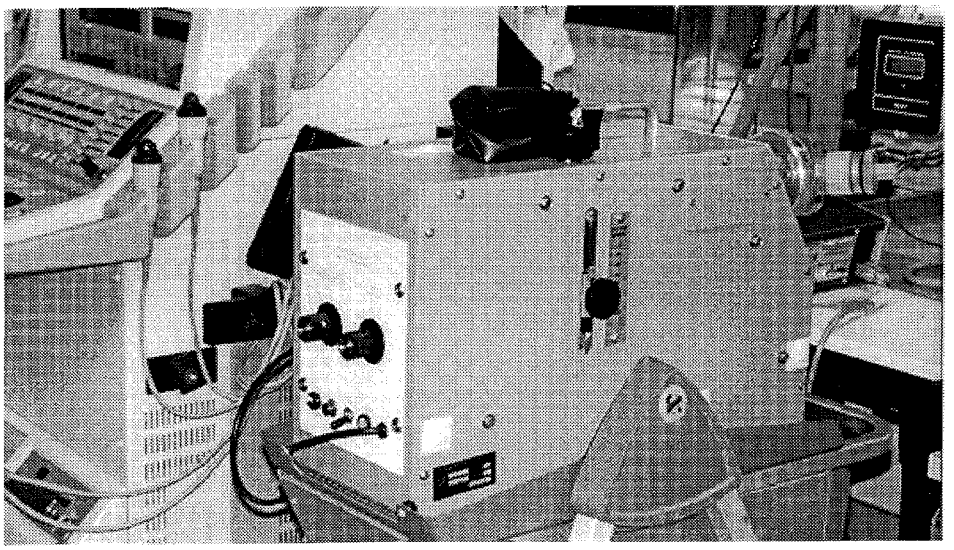

Figure 2.9: The pulsatile Harvard pump used for pulsatile flow experiment.

Chapter 3 Results and Discusion

In this chapter the flow in a 180-degree curved vessel is investigated and our experimental results are presented.

3.1 Results

In order to establish a reference flow standard, we obtained the flow field and secondary flow patterns for conditions similar to the Dean's solution which is steady, non-constrained flow in a curved pipe. The flow rate was chosen around the physiological values of $1.7 - 8$ lit/min which corresponds to a Reynolds number between $1700 - 8000$. The diameter of the test tube is $3.05cm$, and the curvature ratio, a/R, is 0.27, which is close to the curvature ratio of the human aorta. With these conditions the numerical value of the Dean number of the flow is very close to the Reynolds number.

3.1.1 Pattern I. Double Circulation Pattern

The first case is steady flow with a flat incoming velocity profile without any upstream constriction. The secondary flow velocity field for this case is plotted in Figure 3.1. It shows a double circulation pattern similar to what is obtained from the Dean's solution as is plotted in Figure 1.3. The following observations can be drawn from this plot:

- Double circulation secondary pattern.
- As a result of the asymmetry of circulatory pattern and because of mass-conservation higher velocities are observed near the inner bend.

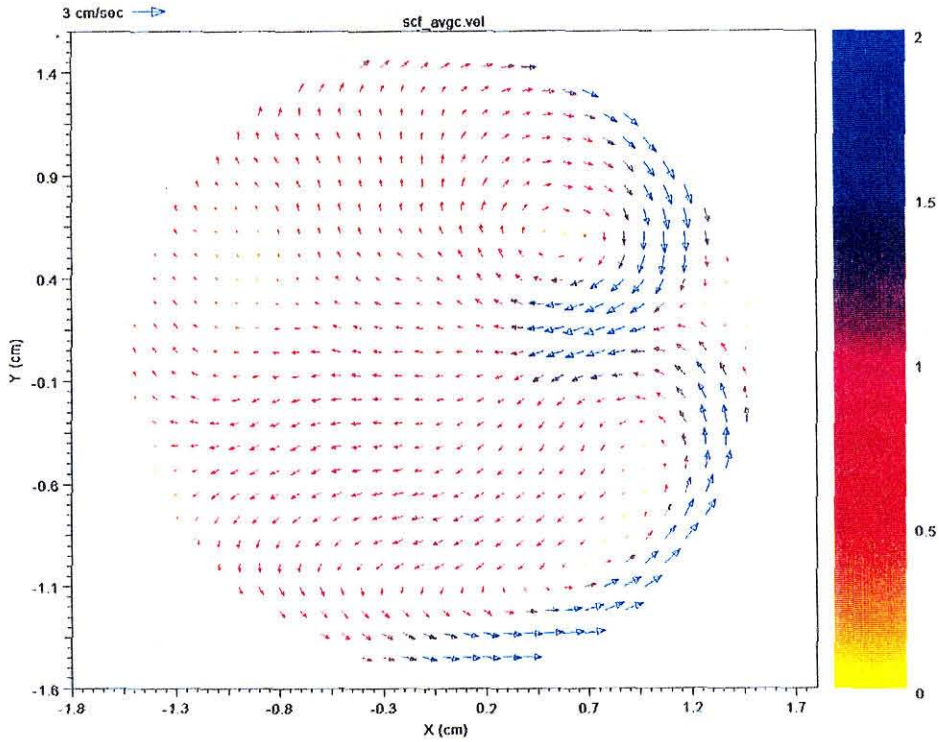

Figure 3.1: The secondary velocity field for the steady flow without upstream constriction. $De = 3850$.

- The secondary flow velocities are about one order of magnitude less than the primary flow velocities.

- As a result the wall shear stress because of secondary flow is much less than the wall shear rate because of primary flow. (we will discuss this in more detail later on.)

The vorticity field corresponding to the flow in Figure 3.1 is plotted in Figure 3.2. The double-circulation pattern corresponds to a Dean type of secondary pattern. From Figure 3.2 the following observations can be made:

- Double circulation secondary pattern is clearly verified.

- The center of the circulatory pattern shifts toward the inner bend and, moreover, the outer bend region and the central part of the cross section have very low vorticity.

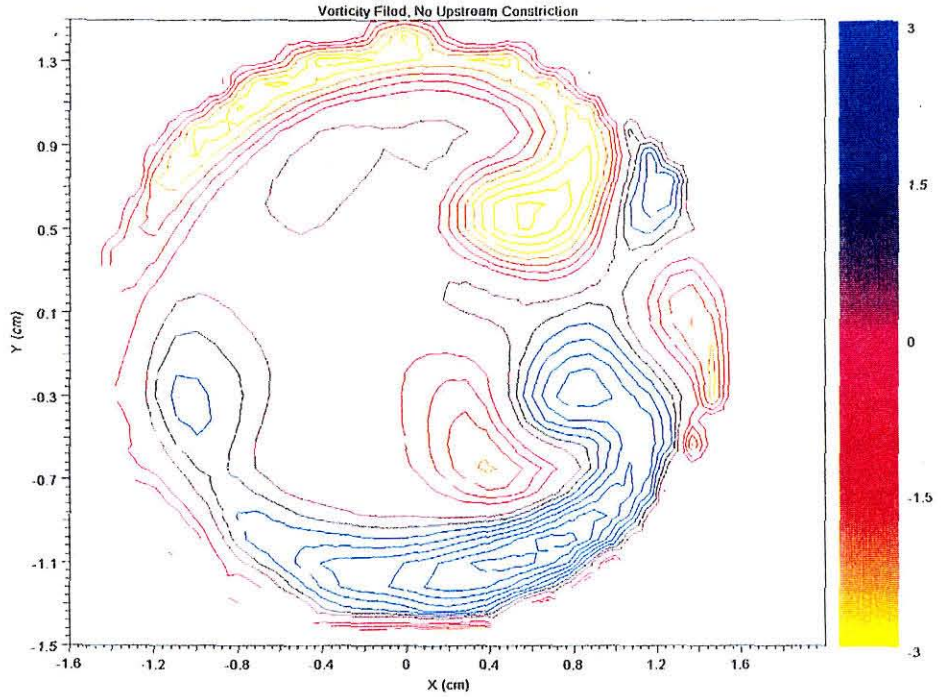

Figure 3.2: The secondary vorticity field for the steady flow without upstream constriction. $De = 3850$.

- A clear separation just at the region near the inner bend is created as a result of the secondary circulatory patterns.

The Reynolds stresses can be calculated and normalized $u'v'$ are depicted in Figure 3.3. This plot shows that the maximum Reynolds stress shifts towards the inner bend. The values of shear stress alongside the outer bend are negligible compared to the shear stress in regions close to the inner bend. From Figure 3.3 the following observations can be made:

- $\omega = 0$ where the velocity is maximum (ω is the vorticity).
- High Reynolds stress is seen near the core of the circulation, close to the region where ω is maximum.

To obtain the value and direction of the shear stress, three velocity profiles along lines shown in Figure 3.4 are drawn and plotted in Figures 3.5, 3.6 and 3.7. The shear stress values along the vessel wall and their change of direction ($\frac{\partial u_\alpha}{\partial r}$) are noticeable. The velocity vector has two components, one parallel and one normal to the line. It

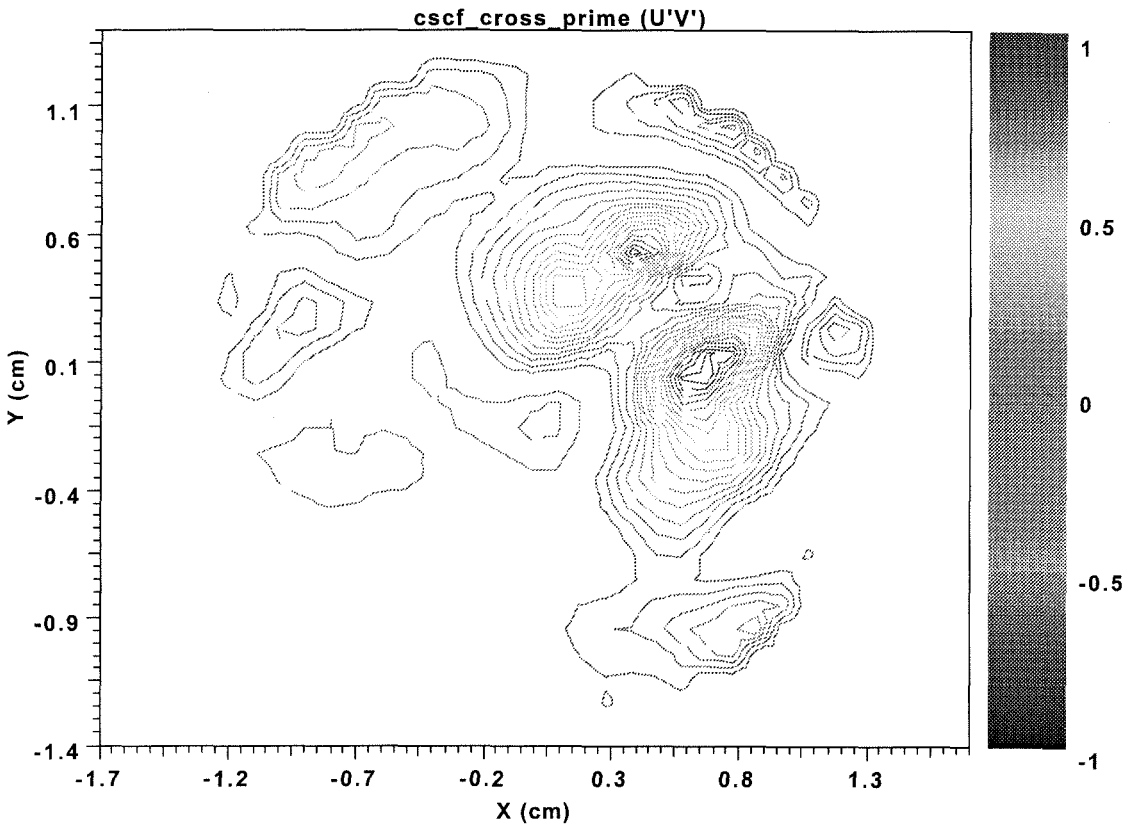

Figure 3.3: The Reynolds stress values for the steady flow without upstream constriction. $De = 3850$.

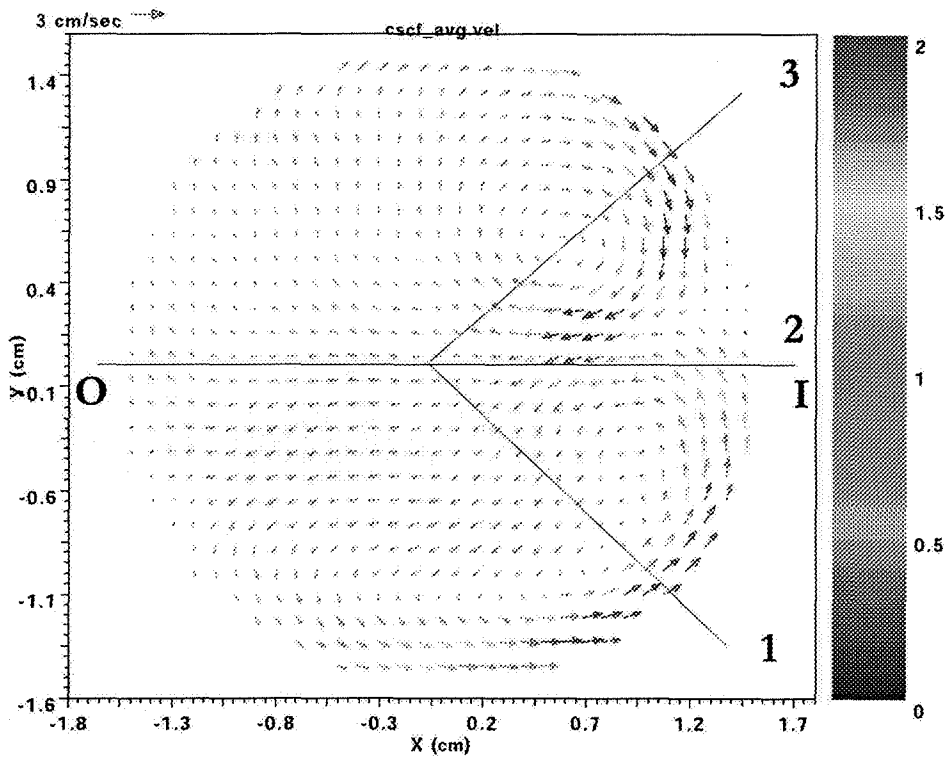

Figure 3.4: The secondary velocity field for the steady flow without upstream constriction and the location of lines for velocity profiles depicted in figures 3.5, 3.6 and 3.7. The horizontal axis is along inner-outer wall and the vertical axis is along the anterior-posterior wall. $De = 3850$.

is noteworthy here that as the radii are perpendicular to the perimeter of the circle, then the normal component of the velocity vector with respect to the profile line gives the u_α component and the tangential component gives the u_r component. At each point on the wall, $(\frac{\partial u_\alpha}{\partial r})$ can be calculated from the slope of the velocity profile in order to calculate the shear stress at the wall. The same convention and terminology will be used consistently throughout the current study, unless stated otherwise.

The velocity and vorticity fields for the pulsatile flow without an upstream constriction are depicted in Figures 3.8 and 3.9. Similar double circulation patterns can be seen for the pulsatile case. The flow signal for the pulsatile flow is plotted in Figure 3.10. To have a time reference for the corresponding phase of the flow a diode signal is triggered which can be matched with the laser pulse signal and the flow signal on

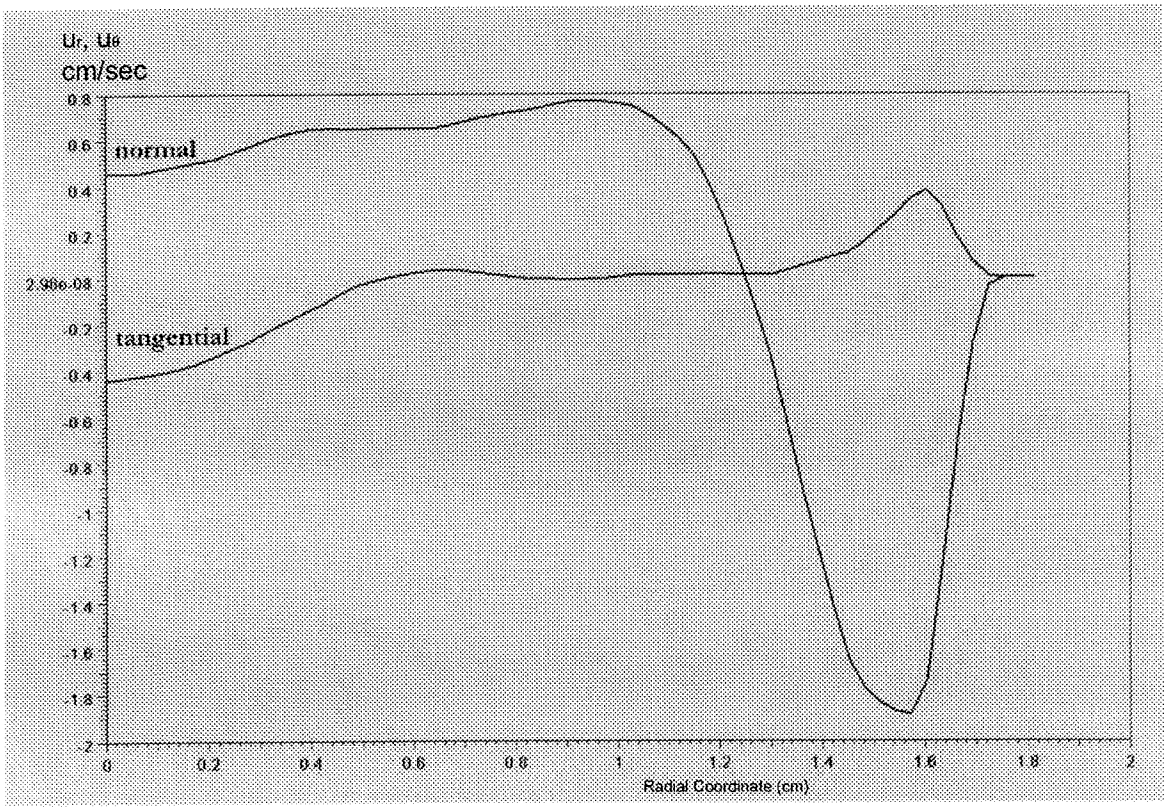

Figure 3.5: The velocity profile of the secondary velocity field for the steady flow without upstream constriction along line 1 as shown in figure 3.4. The velocity vector is decomposed into its normal and tangential components with respect to the line 1. $De = 3850$.

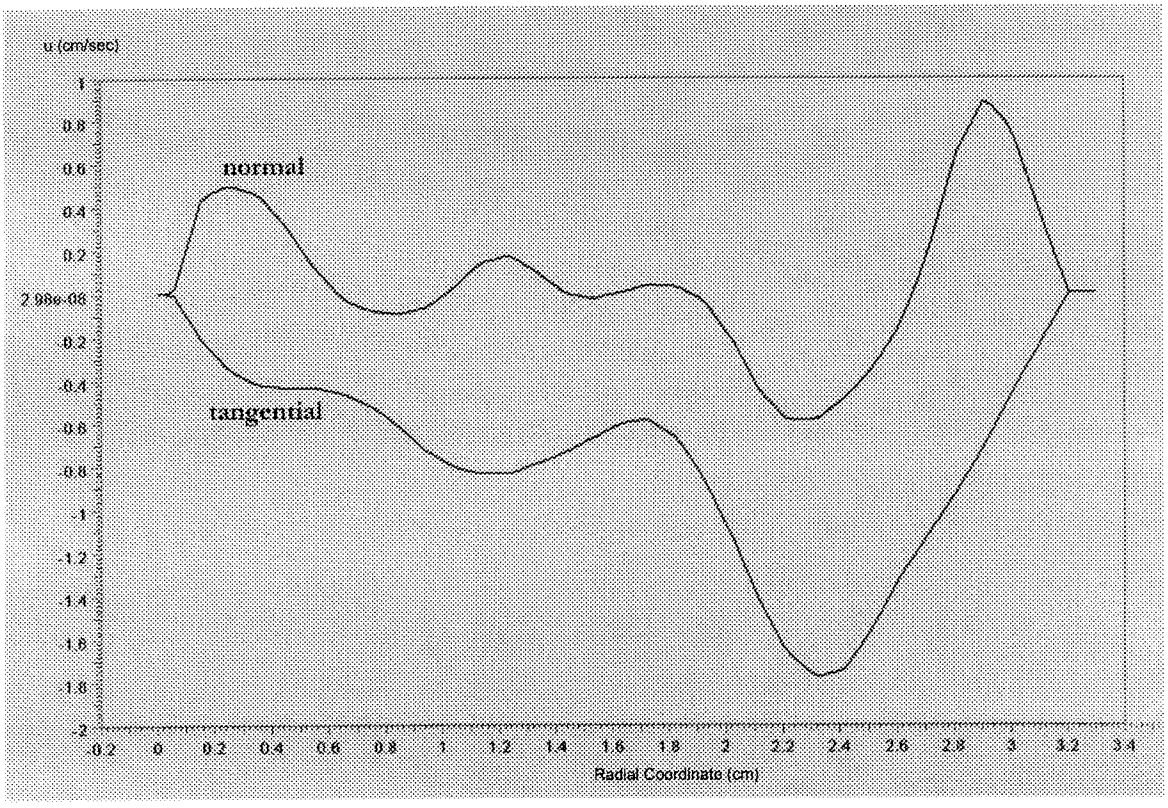

Figure 3.6: The velocity profile of the secondary velocity field for the steady flow without upstream constriction along line 2 as shown in figure 3.4. The velocity vector is decomposed into its normal and tangential components with respect to the line 2. $De = 3850$.

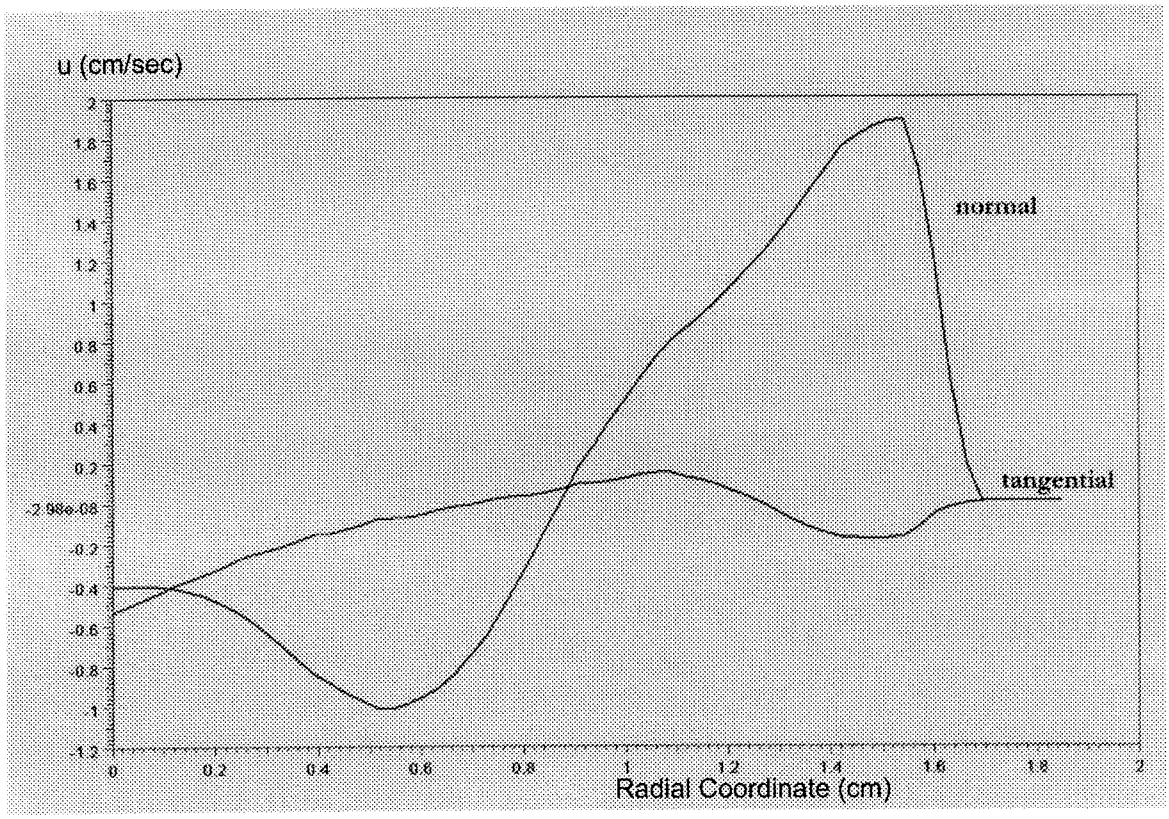

Figure 3.7: The velocity profile of the secondary velocity field for the steady flow without upstream constriction along line 3 as shown in figure 3.4. The velocity vector is decomposed into its normal and tangential components with respect to the line 3. $De = 3850$.

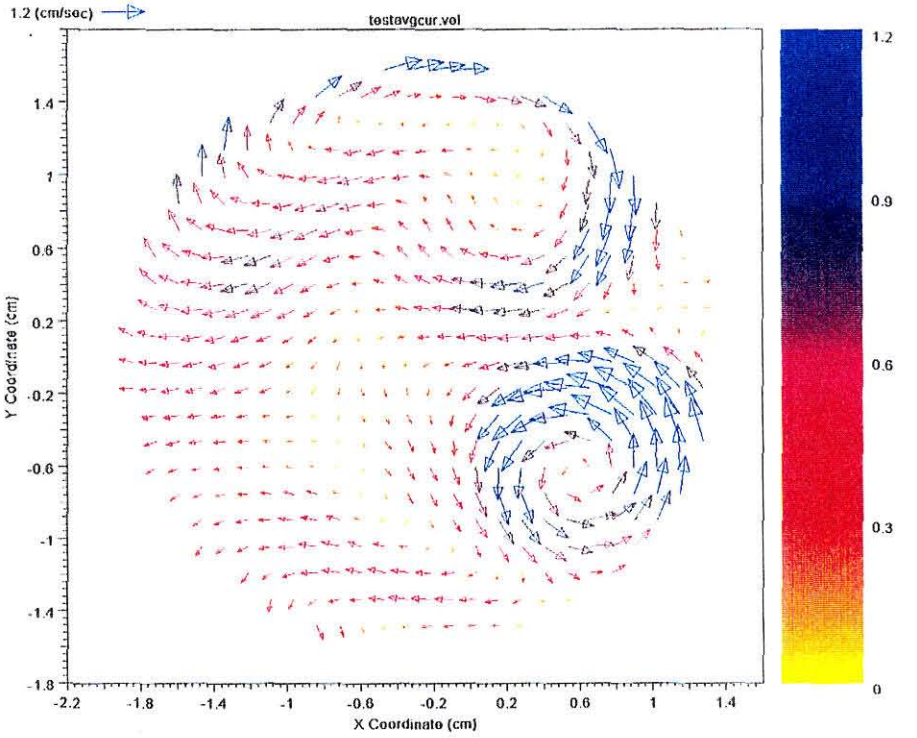

Figure 3.8: The secondary velocity field for the pulsatile flow without upstream constriction. $\alpha = 12.5$.

the same plot in order to specify the frame corresponding to a particular point on the flow signal. Hence, three signals—the flow, the diode and the laser pulse—, are depicted on this figure. Here again we see the change of the direction of shear stress along the inner wall ($\frac{\partial u_\alpha}{\partial r}$). The position of the lines along which the velocity profiles in Figures 3.12, 3.13 and 3.14 are drawn is depicted in Figure 3.11. The Womersley number of this experiment is $\alpha = 12.5$, which corresponds to a 40 bpm pulse rate. In Appendix B all the figures, Womersley numbers and flow conditions are depicted for easy reference.

3.1.2 Pattern II. Single Circulation: Counterclockwise

We study the effect of the upstream constriction on the flow field. Figure 3.15 shows the secondary flow pattern for the steady flow with upstream constriction. The corresponding vorticity field of this case is shown in Figure 3.16. For this case a single-circulation pattern dominates the secondary flow field. The absence of the double-

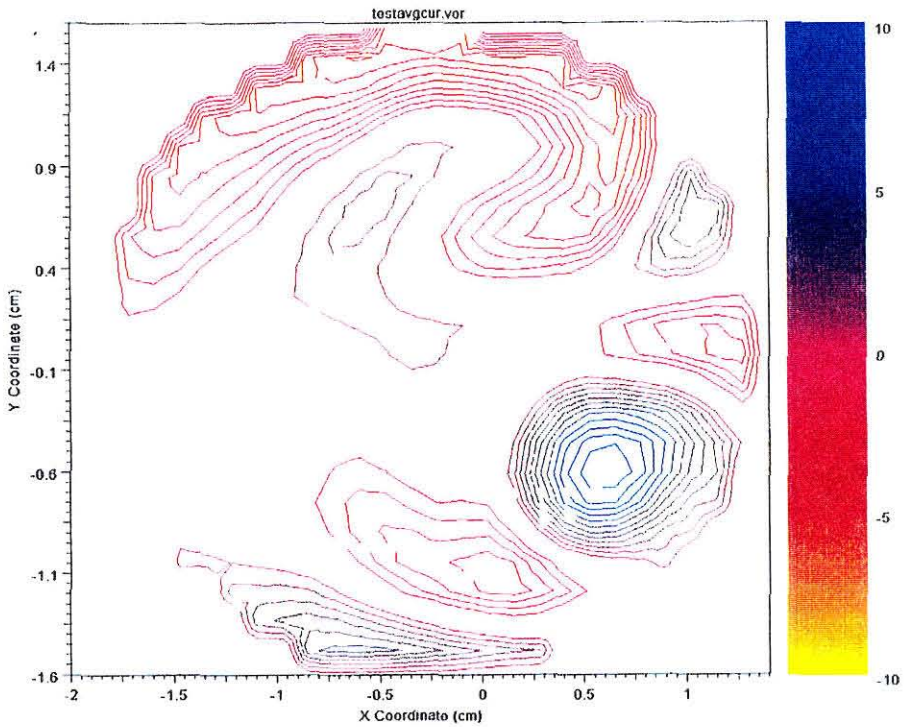

Figure 3.9: The secondary vorticity field for the pulsatile flow without upstream constriction. $\alpha = 12.5$.

circulation pattern is intriguing. For this case the experiment is carried out with a constriction with a 20 percent opening. The transition to a single-circulation pattern was found to happen independent of the flow rate. The same single-circulation pattern characterizes the constrained pulsatile case (Figures 3.21 and 3.22). Figure 3.17 shows the position of the lines across which the velocity profiles depicted in Figures 3.18, 3.19 and 3.20 are obtained.

In the velocity profiles both normal and tangential components of the velocity with respect to the crossing line are plotted. The maximum slope of the normal component in these profiles show the value of $\frac{\partial u_\alpha}{\partial r}$ at the wall, or the shear stress at the wall. The direction of this shear stress is different for points 1, 2, and 3 in the double circulation pattern while it is the same for the single circulation pattern.

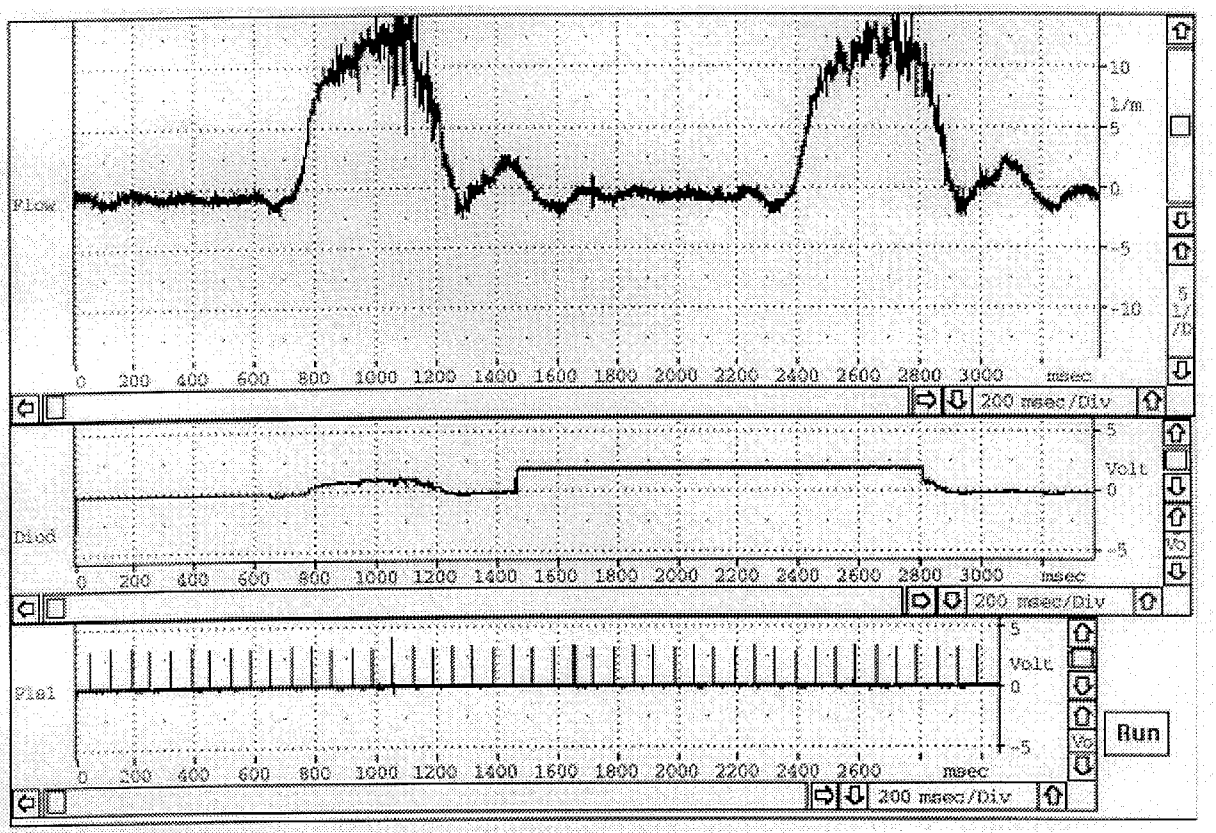

Figure 3.10: The flow signal for the pulsatile flow without upstream constriction. $\alpha = 12.5$. The two other signals are the laser pulse signal and the time-reference signal of a manually triggered diode, which enables us to locate the frame position on the flow signal.

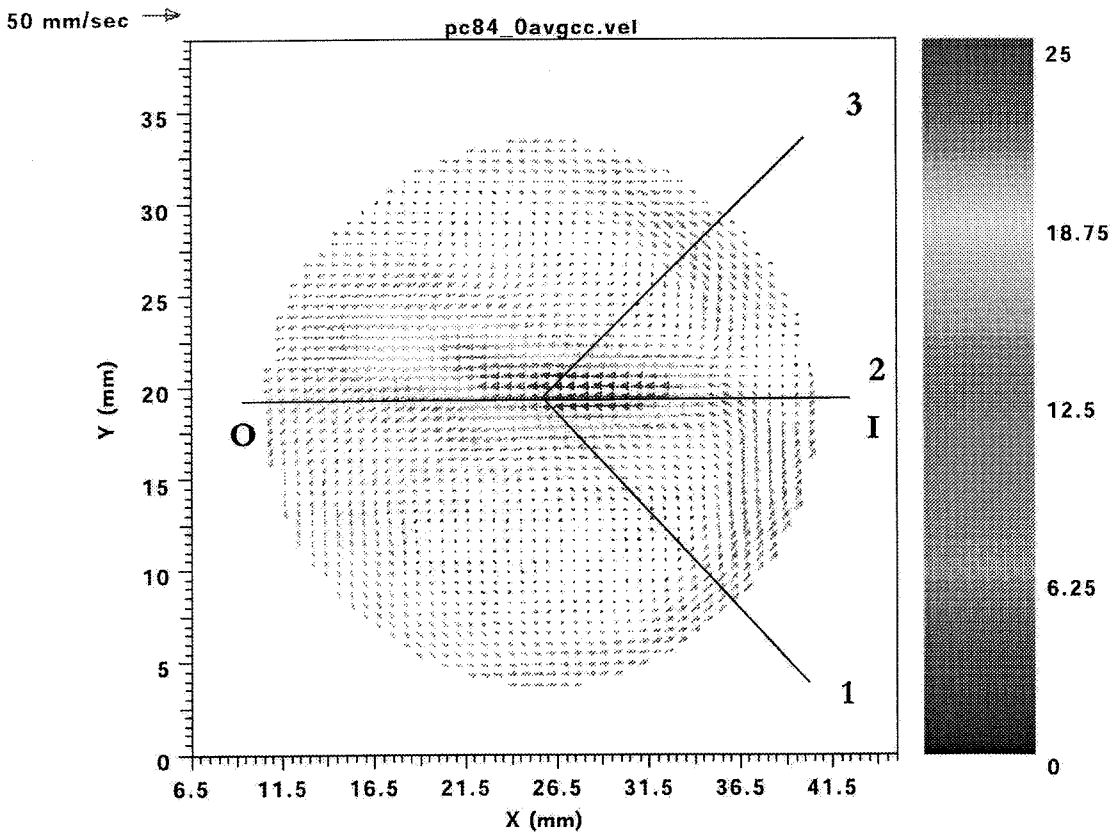

Figure 3.11: The secondary velocity field for the pulsatile flow without upstream constriction and the location of lines for velocity profiles depicted in Figures 3.12, 3.13 and 3.14. The horizontal axis is along inner-outer wall and the vertical axis is along the anterior-posterior wall. $\alpha = 12.5$.

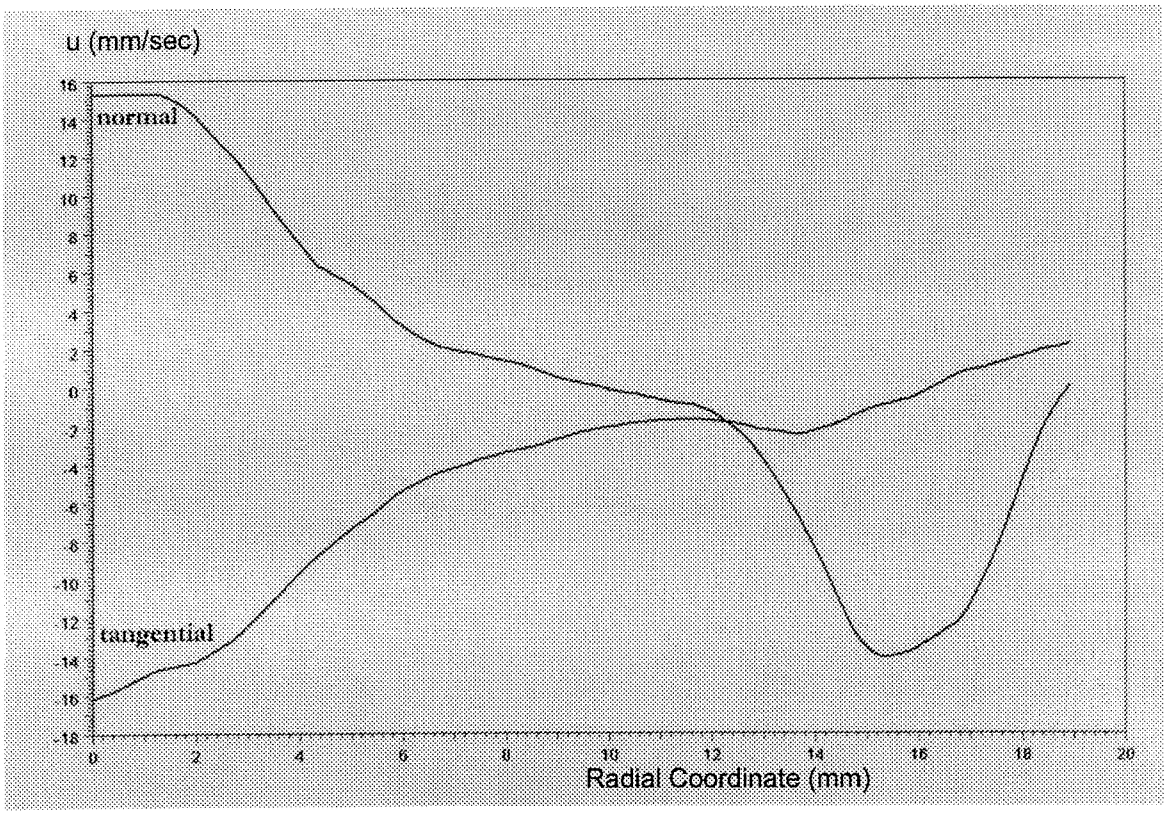

Figure 3.12: The velocity profile of the secondary velocity field for the pulsatile flow without upstream constriction along line 1 as shown in Figure 3.11. The velocity vector is decomposed into its normal and tangential components with respect to the line 1.

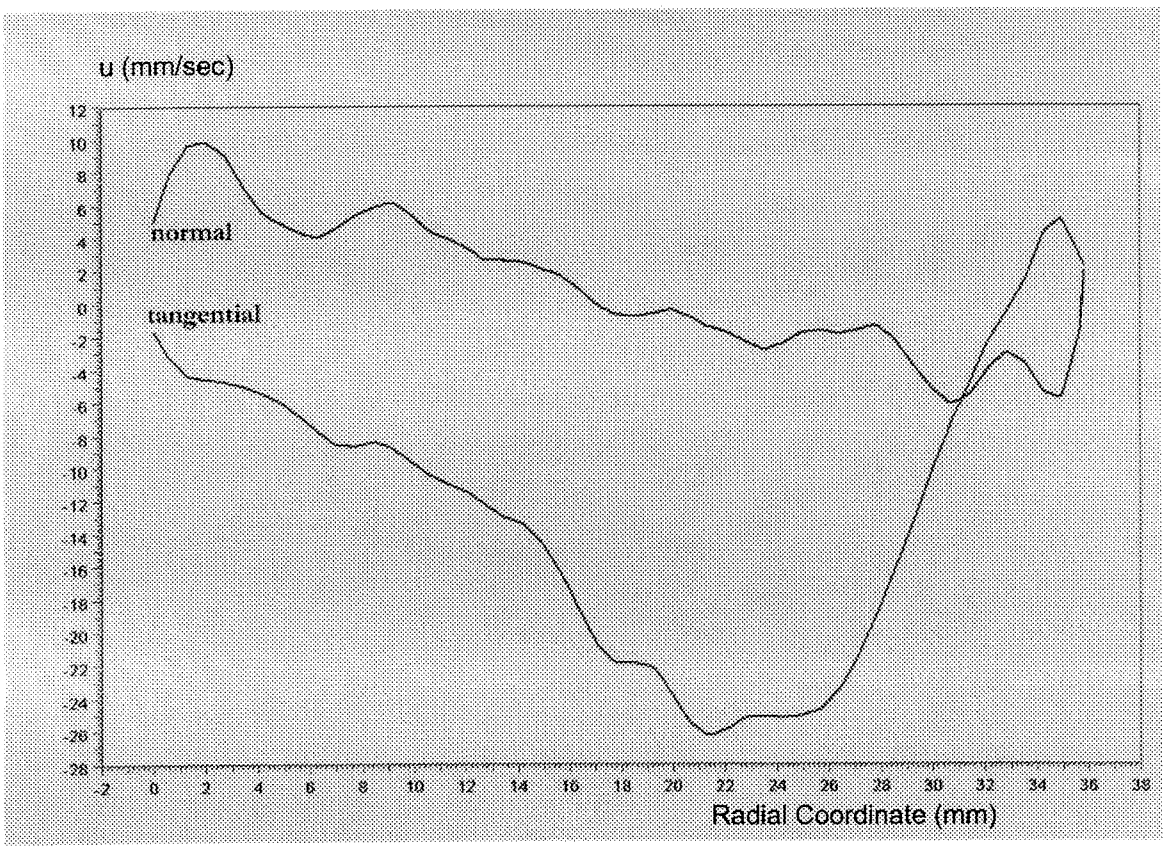

Figure 3.13: The velocity profile of the secondary velocity field for the pulsatile flow without upstream constriction along line 2 as shown in Figure 3.11. The velocity vector is decomposed into its normal and tangential components with respect to the line 2. $\alpha = 12.5$.

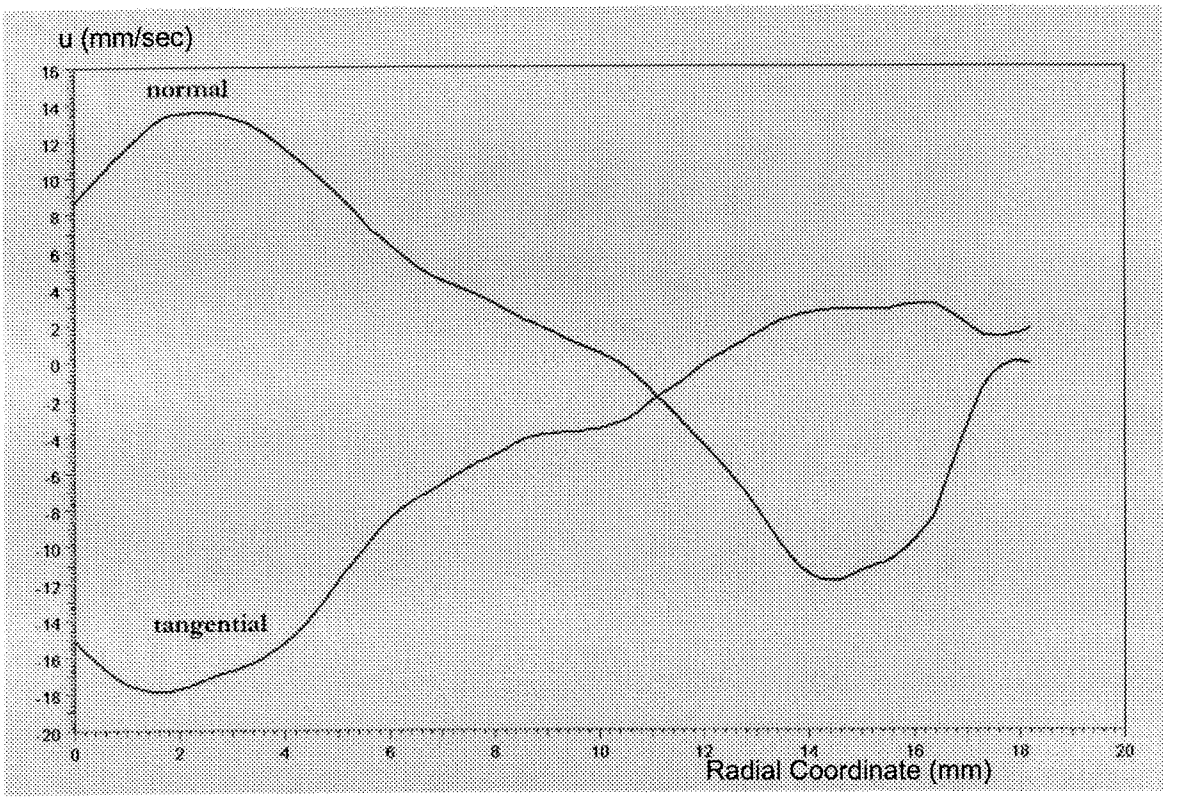

Figure 3.14: The velocity profile of the secondary velocity field for the pulsatile flow without upstream constriction along line 3 as shown in Figure 3.11. The velocity vector is decomposed into its normal and tangential components with respect to the line 3. $\alpha = 12.5$.

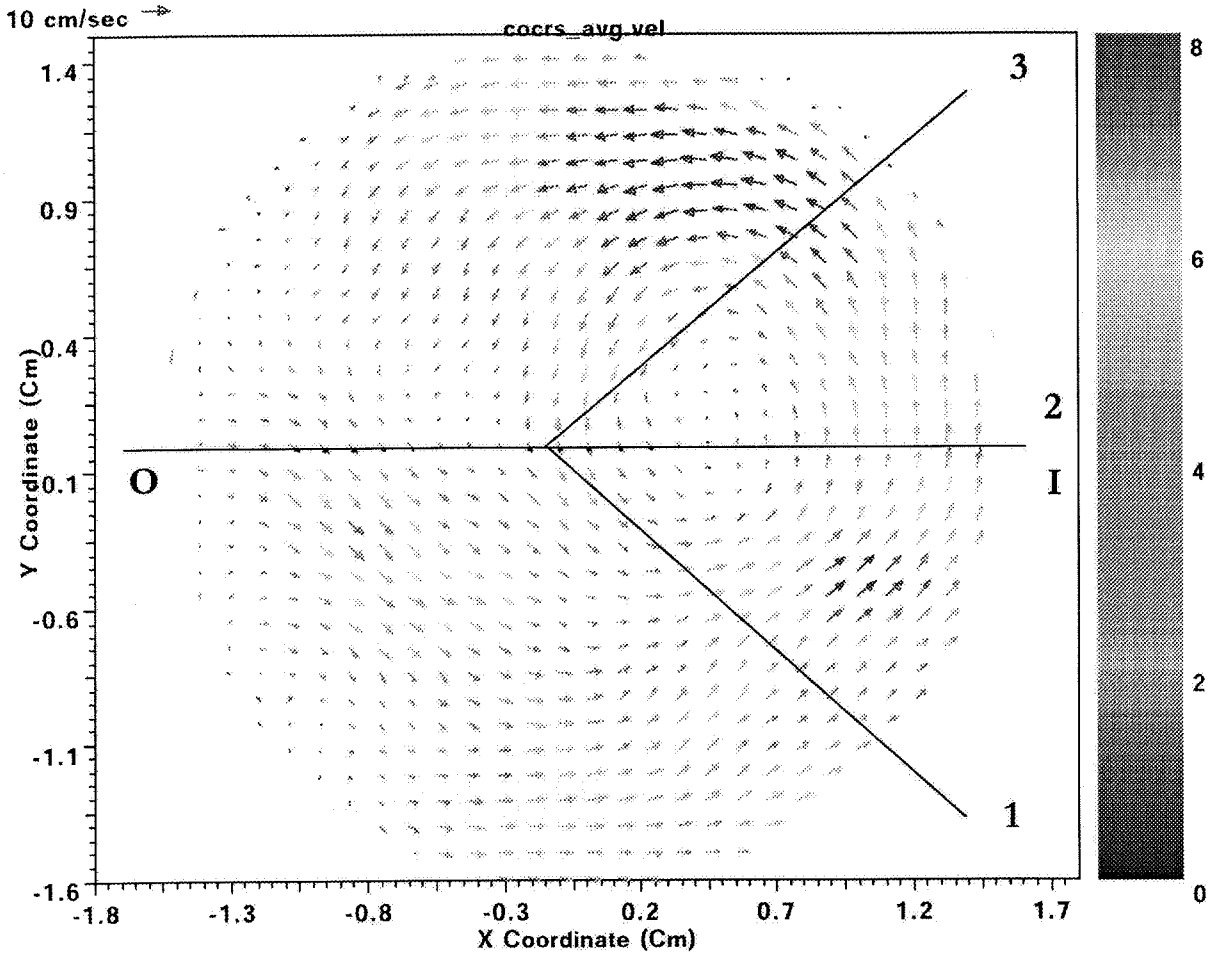

Figure 3.15: The secondary velocity field for the steady flow with upstream constriction. $De = 3850$.

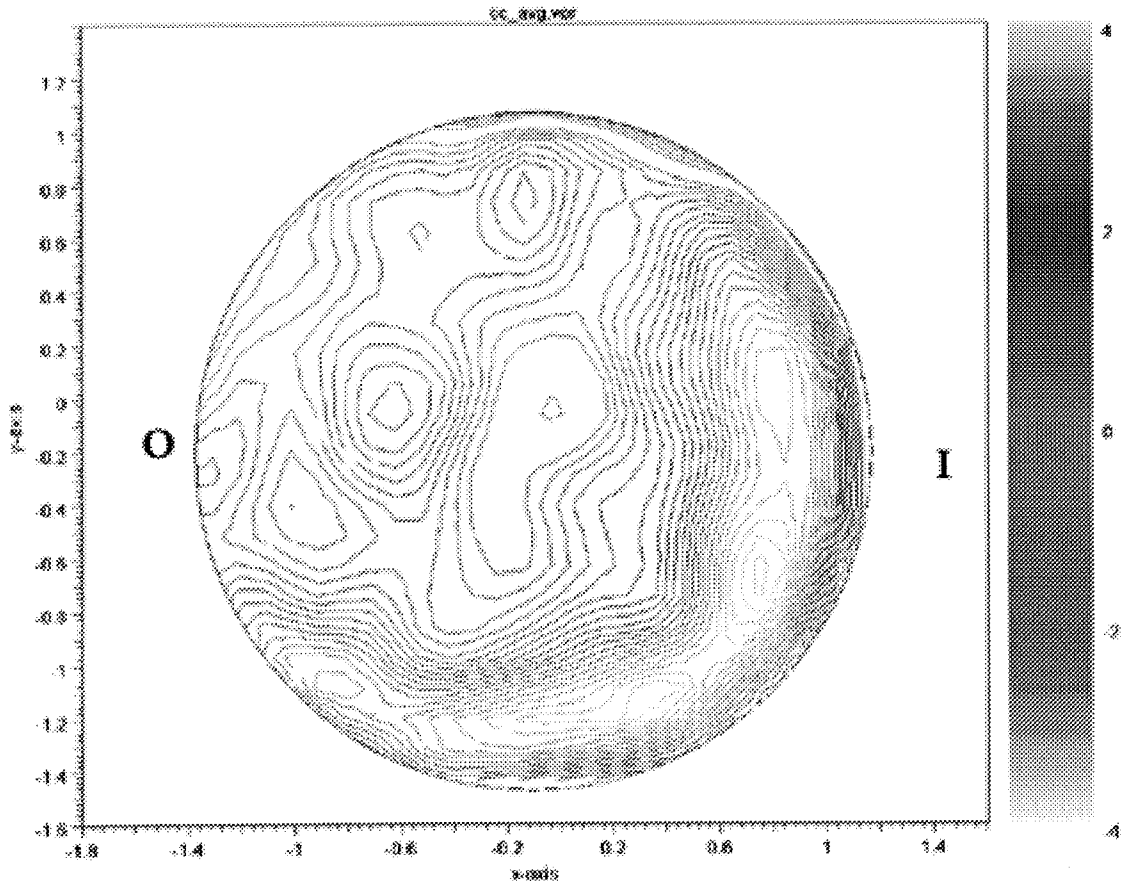

Figure 3.16: The secondary vorticity field for the steady flow with upstream constriction. $De = 3850$.

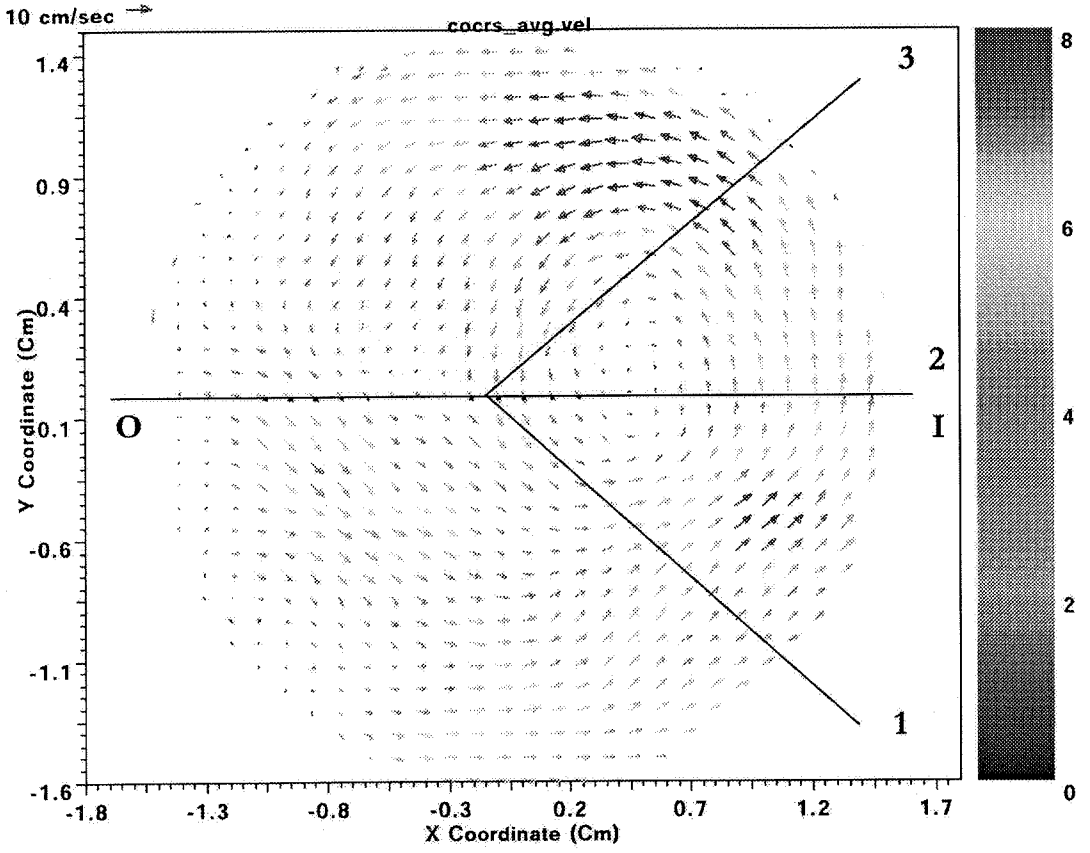

Figure 3.17: The secondary velocity field and the location of lines for velocity profiles depicted in Figures 3.18, 3.19 and 3.20 for the steady flow with upstream constriction. The horizontal axis is along inner-outer wall and the vertical axis is along the anterior-posterior wall. $De = 3850$.

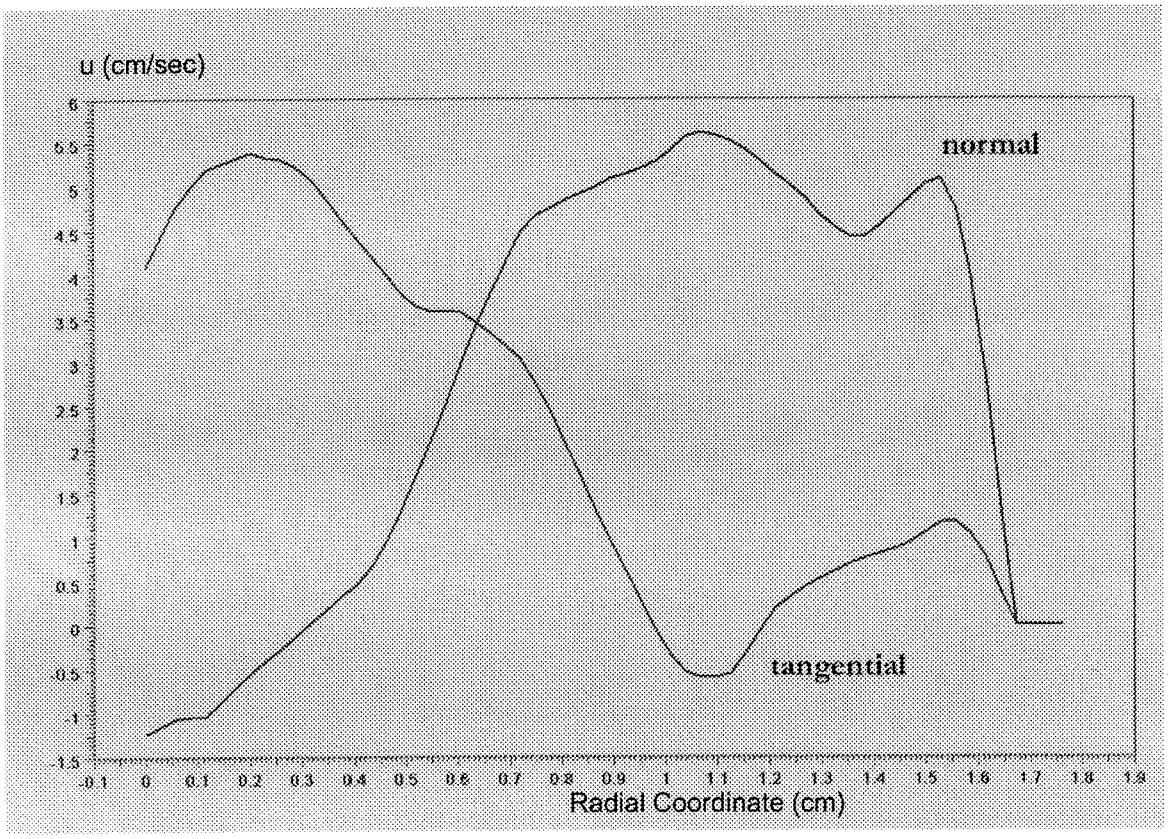

Figure 3.18: The velocity profile of the secondary velocity field along the line 1 as shown in Figure 3.17, for the steady flow with upstream constriction. The velocity vector is decomposed into its normal and tangential components with respect to the line 1. $De = 3850$.

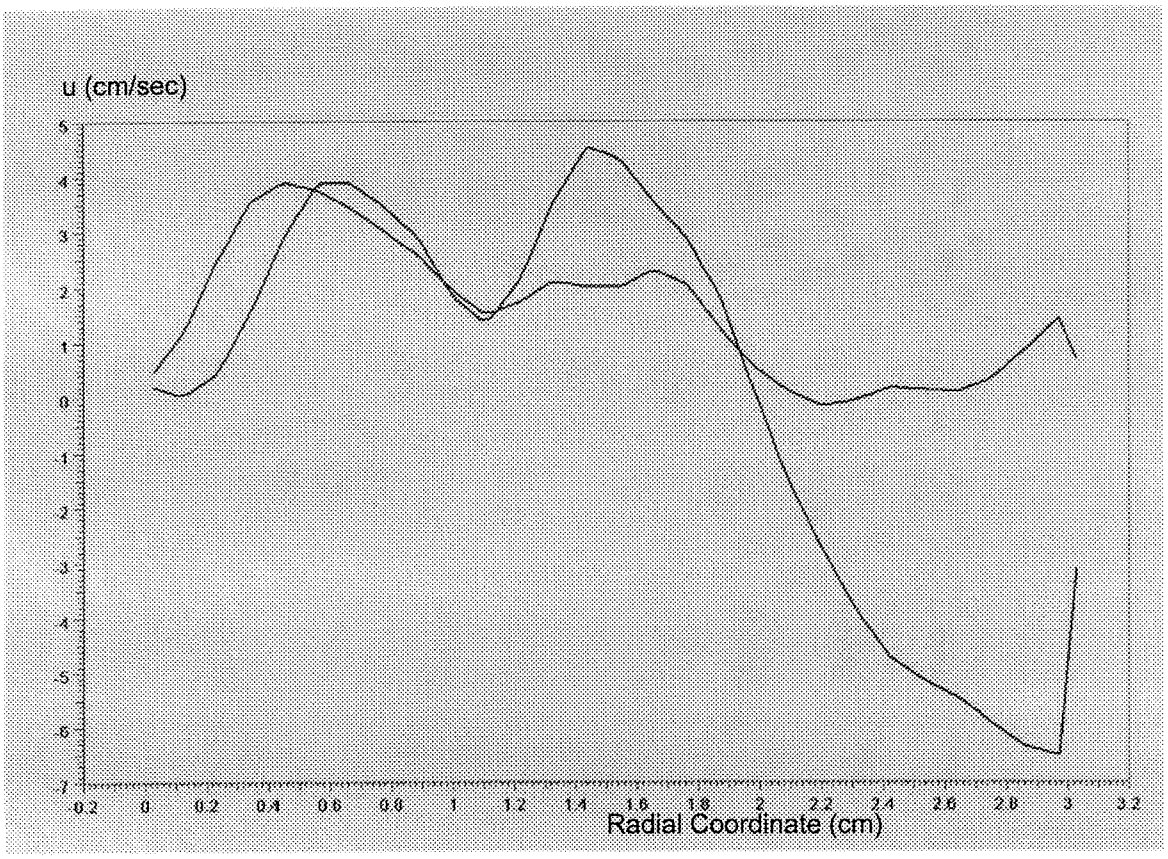

Figure 3.19: The velocity profile of the secondary velocity field along the line 2 as shown in Figure 3.17, for the steady flow with upstream constriction. The velocity vector is decomposed into its normal and tangential components with respect to the line 2. $De = 3850$.

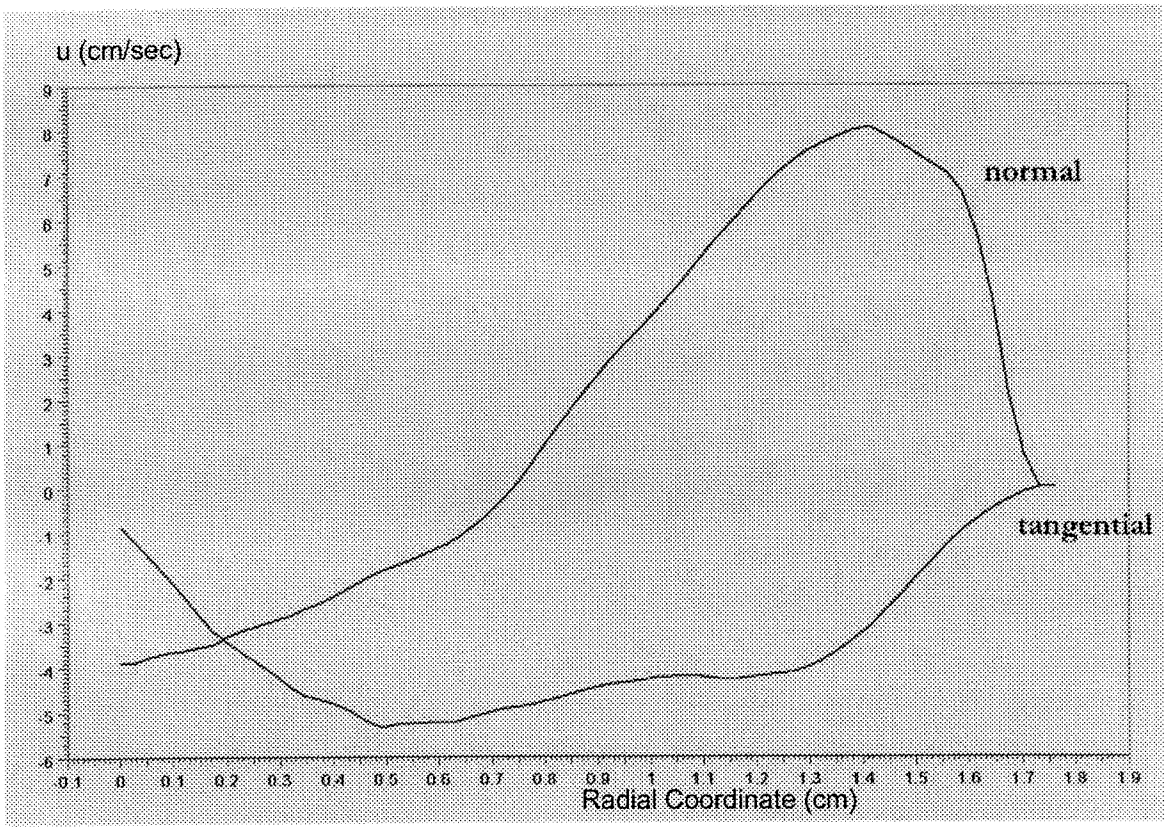

Figure 3.20: The velocity profile of the secondary velocity field along the line 3 as shown in Figure 3.17, for the steady flow with upstream constriction. The velocity vector is decomposed into its normal and tangential components with respect to the line 3. $De = 3850$.

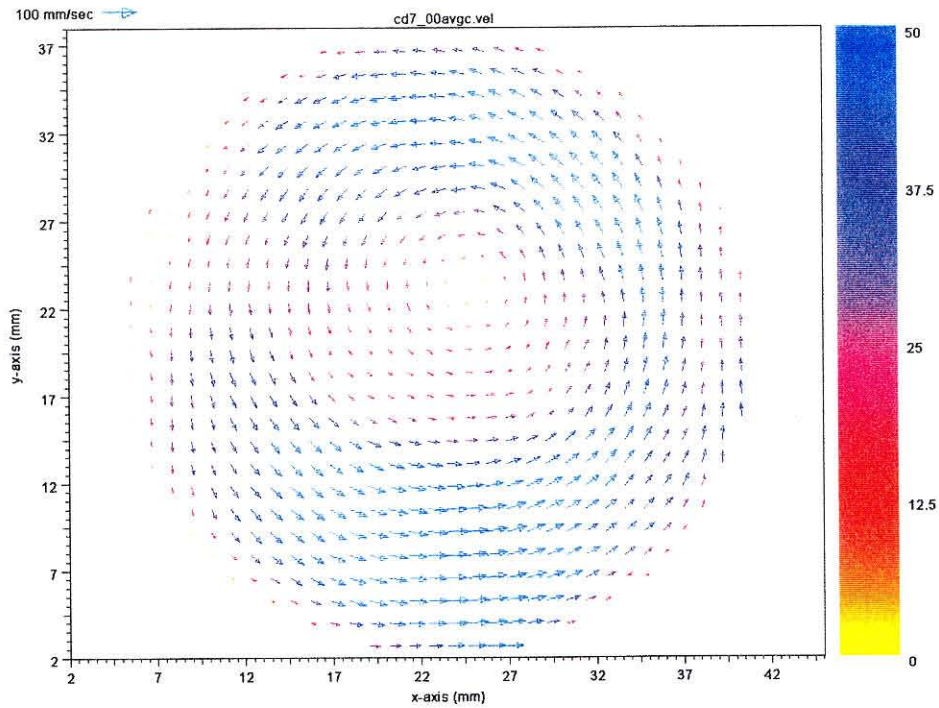

Figure 3.21: The secondary velocity field for the pulsatile flow with upstream constriction $\beta = 80\%$. $\alpha = 12.5$.

3.1.3 Pattern III. Clockwise Single Circulation

To further determine the effect of the spatial configuration of the upstream constriction on the secondary flow pattern, a series of experiments were carried out with an orifice which had an asymmetric opening with a constriction ratio, $\beta = 80\%$. α, the angular position of the orifice opening, measured as depicted in Figure 2.4 was set for $\alpha = 0^0, 90^0, 180^0, 270^0$. For all cases a single circulation pattern was observed. For $\alpha = 180^0$ position the sense of rotation of the circulation changed from a counter-clockwise to a clockwise circulation. The corresponding flow fields are depicted in the Appendix B and the results are summarized in the Table 1-3. This pattern turns out to be the same regardless of the flow type, *i.e.*, for both the steady and the pulsatile flows, and at different flow rates the same behavior is observed. The velocity field for the steady flow with an asymmetric constriction with $\alpha = 180^0$ with respect to the posterior wall is depicted in Figure 3.23. The corresponding vorticity field is depicted in Figure 3.24.

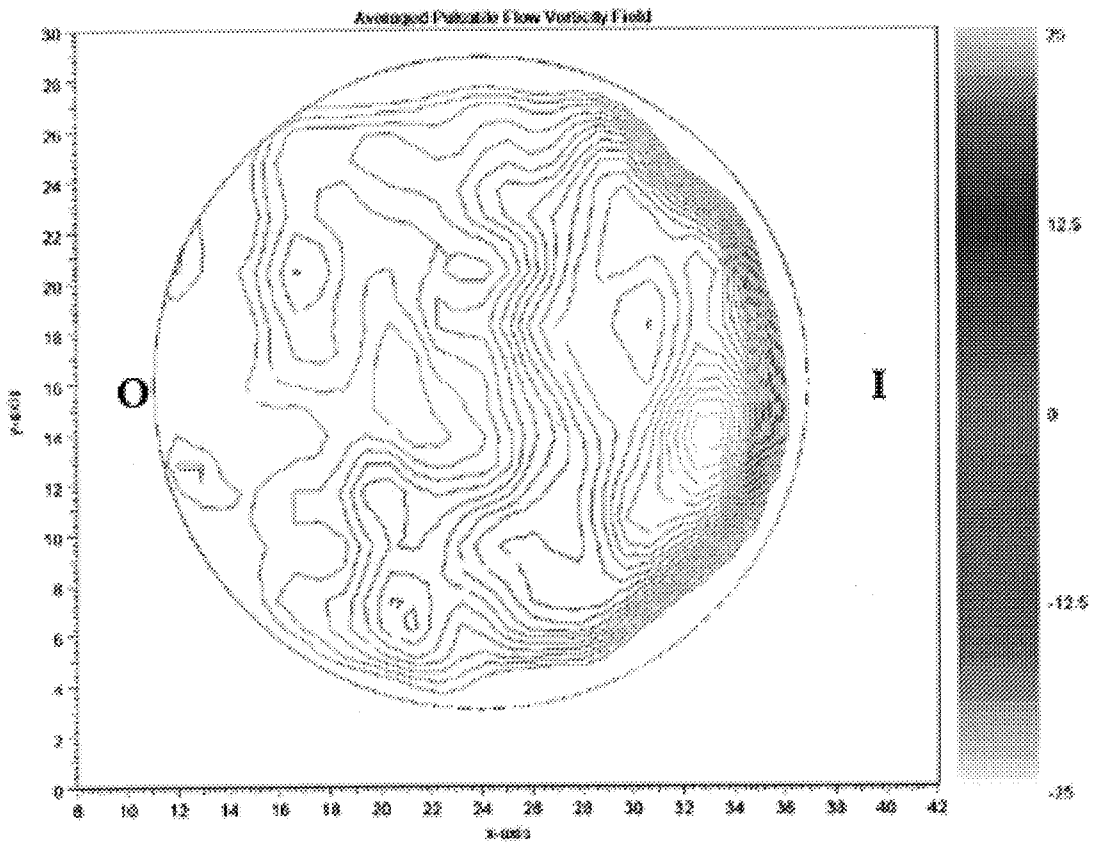

Figure 3.22: The secondary vorticity field for the pulsatile flow with upstream constriction $\beta = 80\%$. $\alpha = 12.5$.

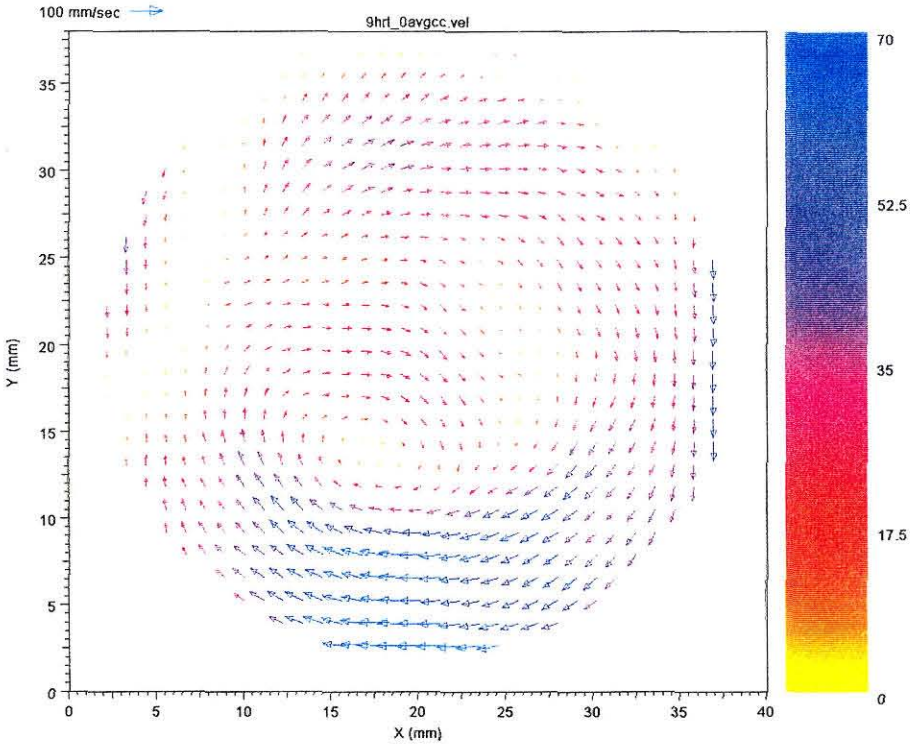

Figure 3.23: The secondary velocity field for the steady flow with asymmetric upstream constriction at angular position $\alpha = 180^0$. $De = 1900$.

3.2 Table of Results

The secondary flow patterns and the sense of rotation are summarized in Table 3.1 for different flow rates, flow signals(steady versus pulsatile) and upstream constriction conditions. Table 3.2 shows the Dean number and Reynolds number values for the steady flow case, and Table 3.3 gives the Womersley number, frequency and average flow rate for the pulsatile flow experiments in the curved vessel.

No.	Condition	*Steady*	*Pulsatile*
1	*No Constriction(low)*	Double Circulation	Double Circulation
2	*No Constriction(high)*	Double Circulation	Double Circulation
3	*Small Orifice(low)*	CCW Single Circulation	CCW Single Circulation
4	*Small Orifice(high)*	CCW Single Circulation	CCW Single Circulation
5	*Middle Orifice(low)*	CCW Single Circulation	CCW Single Circulation
6	*Middle Orifice(high)*	CCW Single Circulation	CCW Single Circulation
7	*Large Orifice(low)*	CCW Single Circulation	CCW Single Circulation
8	*Large Orifice(high)*	CCW Single Circulation	CCW Single Circulation
9	*Asymmetric Orifice,* 0^0 *(low)*	CCW Single Circulation	CCW Single Circulation
10	*Asymmetric Orifice,* 0^0 *(high)*	CCW Single Circulation	CCW Single Circulation
11	*Asymmetric Orifice,* 90^0 *(low)*	CCW Single Circulation	CCW Single Circulation
12	*Asymmetric Orifice,* 90^0*(high)*	CCW Single Circulation	CCW Single Circulation
13	*Asymmetric Orifice,* 180^0*(low)*	CW Single Circulation	CW Single Circulation
14	*Asymmetric Orifice,* 180^0*(high)*	CW Single Circulation	CW Single Circulation
15	*Asymmetric Orifice,* 270^0*(low)*	CCW Single Circulation	CCW Single Circulation
16	*Asymmetric Orifice,* 270^0*(high)*	CCW Single Circulation	CCW Single Circulation

Table 3.1: Secondary flow patterns and the sense of rotation for steady and pulsatile flow with different upstream boundary conditions. The angular position of the asymmetric constriction is measured from the posterior wall of the bend. High and low refer to the flow rate. CW stands for clockwise rotation and CCW stands for counterclockwise rotation. The numerical values of the Reynolds number and flow rates are reported in the table 3.2 for the steady case and in table 3.3 for the pulsatile flow. The angular position of the asymmetric orifice, α, is measured clockwise from the posterior wall of the bend.

No.	Condition	Flow Rate(l/m)	De	Re
1	*No Constriction(low)*	2.5	1840	1768.5
2	*No Constriction(high)*	5.0	3680	3537
3	*Small Orifice(low)*	2.5	1840	1768.5
4	*Small Orifice(high)*	5.0	3680	3537
5	*Middle Orifice(low)*	2.5	1840	1768.5
6	*Middle Orifice(high)*	5.0	3680	3537
7	*Large Orifice(low)*	2.5	1840	1768.5
8	*Large Orifice(high)*	5.0	3680	3537
9	*Asymmetric Orifice,* 0^0 *(low)*	2.5	1840	1768.5
10	*Asymmetric Orifice,* 0^0 *(high)*	5.0	3680	3537
11	*Asymmetric Orifice,* 90^0 *(low)*	2.5	1840	1768.5
12	*Asymmetric Orifice,* 90^0*(high)*	5.0	3680	3537
13	*Asymmetric Orifice,* 180^0*(low)*	2.5	1840	1768.5
14	*Asymmetric Orifice,* 180^0*(high)*	5.0	3680	3537
15	*Asymmetric Orifice,* 270^0*(low)*	2.5	1840	1768.5
16	*Asymmetric Orifice,* 270^0*(high)*	5.0	3680	3537

Table 3.2: Flow rate values, Dean number and Reynolds number for the steady flow experiment in the curved vessel model. The angular position of the asymmetric orifice, α, is measured as depicted in Figure 2.4.

No.	Condition	Flow Rate(l/m)	$\omega(min^{-1})$	α
1	*No Constriction(low)*	1.7	20	8.6
2	*No Constriction(high)*	3.4	40	12.5
3	*Small Orifice(low)*	1.7	20	8.6
4	*Small Orifice(high)*	3.4	40	12.5
5	*Middle Orifice(low)*	1.7	20	8.6
6	*Middle Orifice(high)*	3.4	40	12.5
7	*Large Orifice(low)*	1.7	20	8.6
8	*Large Orifice(high)*	3.4	40	12.5
9	*Asymmetric Orifice,* 0^0 *(low)*	1.7	20	8.6
10	*Asymmetric Orifice,* 0^0 *(high)*	3.4	40	12.5
11	*Asymmetric Orifice,* 90^0 *(low)*	1.7	20	8.6
12	*Asymmetric Orifice,* 90^0*(high)*	3.4	40	12.5
13	*Asymmetric Orifice,* 180^0*(low)*	1.7	20	8.6
14	*Asymmetric Orifice,* 180^0*(high)*	3.4	40	12.5
15	*Asymmetric Orifice,* 270^0*(low)*	1.7	20	8.6
16	*Asymmetric Orifice,* 270^0*(high)*	3.4	40	12.5

Table 3.3: Flow rate values, frequency and Womersley number for the pulsatile flow experiment in the curved vessel model. The angular position of the asymmetric orifice, α, is measured clockwise as depicted in Figure 2.4.

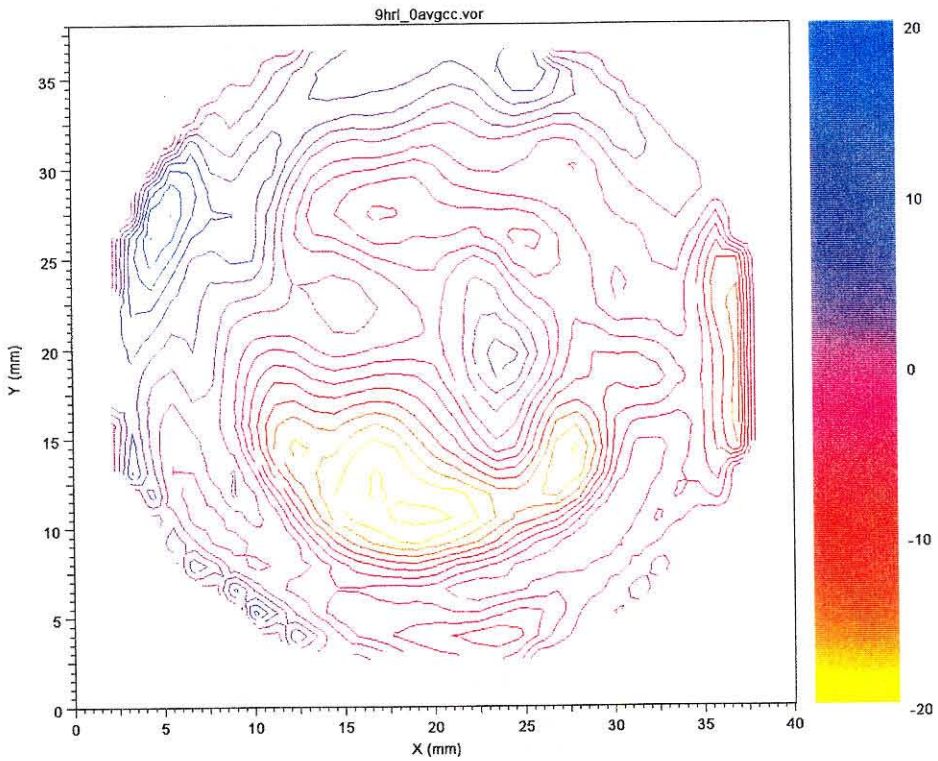

Figure 3.24: The secondary vorticity field for the steady flow with asymmetric upstream constriction at angular position $\alpha = 180^0$. $De = 1900$.

3.3 Further Investigation of the Sense of Rotation for Secondary Flow Patterns

To further investigate the parameters that determine the sense of rotation for the single-circulation patterns, another set of experiments were carried out with the position of orifice opening being varied in 45^0 increments from the posterior and anterior wall of the vessel. The results are tabulated in Table 3.4. The corresponding secoondary velocity fields are depicted in Figure 3.25, Figure 3.26, Figure 3.27and Figure 3.28. For the sake of brevity only one figure from each is depicted here and the rest are depicted in the Appendix.

No.	Condition	*Steady*	*Pulsatile*
1	*Asymmetric Orifice,* 45^0 *(low)*	CCW Single Circulation	CCW Single Circulation
2	*Asymmetric Orifice,* 45^0 *(high)*	CCW Single Circulation	CCW Single Circulation
3	*Asymmetric Orifice,* 135^0 *(low)*	CW Single Circulation	CW Single Circulation
4	*Asymmetric Orifice,* 135^0*(high)*	CW Single Circulation	CW Single Circulation
5	*Asymmetric Orifice,* 225^0*(low)*	CW Single Circulation	CW Single Circulation
6	*Asymmetric Orifice,* 225^0*(high)*	CW Single Circulation	CW Single Circulation
7	*Asymmetric Orifice,* 315^0*(low)*	CCW Single Circulation	CCW Single Circulation
8	*Asymmetric Orifice,* 315^0*(high)*	CCW Single Circulation	CCW Single Circulation

Table 3.4: Secondary flow patterns and the sense of rotation for steady and pulsatile flow with different upstream boundary conditions. The angular position of the asymmetric constriction is measured from the posterior wall of the bend. High and low refer to the flow rate. CW stands for clockwise rotation and CCW stands for counterclockwise rotation. The numerical values of the Reynolds number and flow rates are reported in the table 3.2 for the steady case and in table 3.3 for the pulsatile flow. The angular position of the asymmetric orifice, α, is measured clockwise from the posterior wall of the bend.

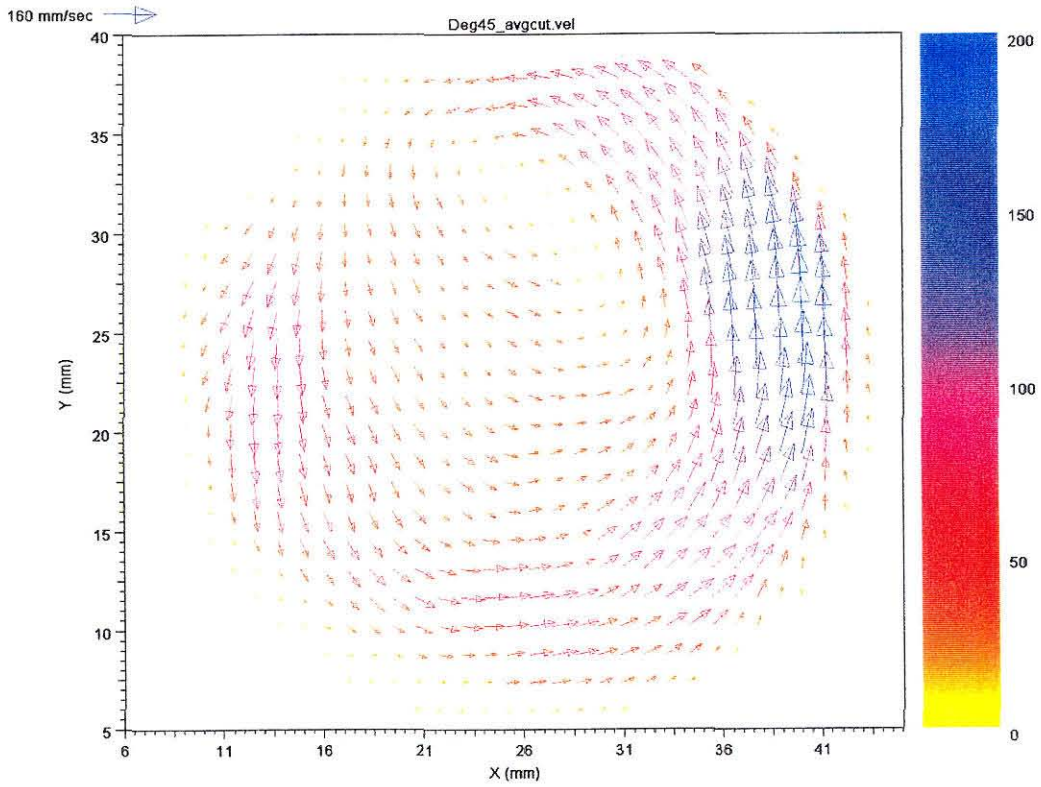

Figure 3.25: The secondary velocity field for the steady flow with upstream constriction $\beta = 80\%$ mounted in $\alpha = 45^0$ position with respect to the posterior wall of the vessel.

3.4 Longitudinal or Axial Flow

In this section the axial or longitudinal flow for the steady and pulsatile flow, with and without upstream constriction, are investigated.

3.4.1 Case I. Steady Flow

Figures 3.29, 3.30 and 3.31 show the axial velocity field for the steady flow under the following upstream conditions:

- No upstream constriction
- Upstream constriction with $\beta = 80\%$
- Upstream constriction with $\beta = 88\%$

From these images the following conclusions can be made:

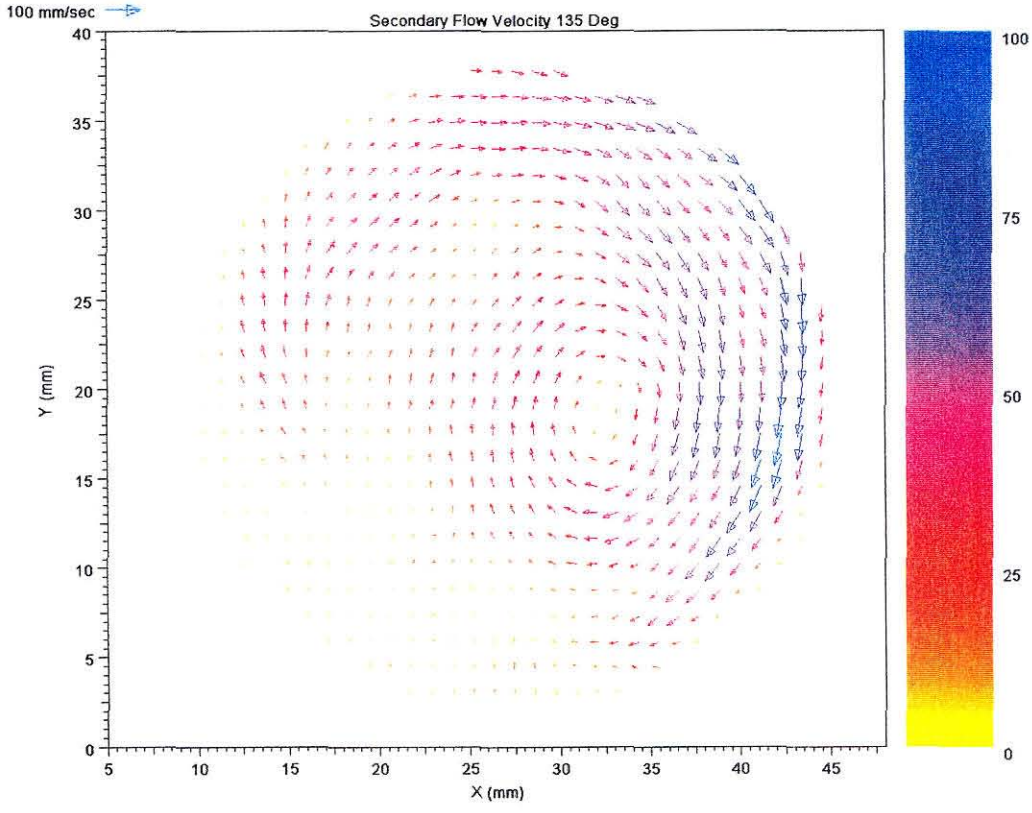

Figure 3.26: The secondary velocity field for the steady flow with upstream constriction $\beta = 80\%$ mounted in $\alpha = 135^0$ position with respect to the posterior wall of the vessel.

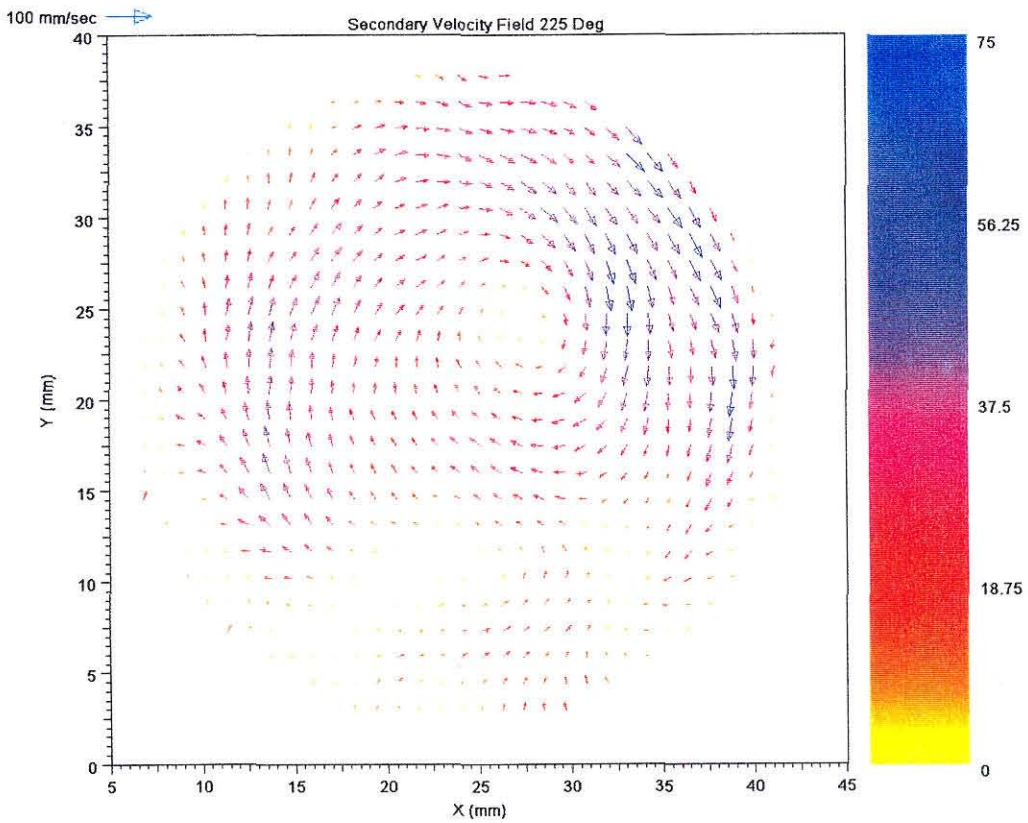

Figure 3.27: The secondary velocity field for the steady flow with upstream constriction $\beta = 80\%$ mounted in $\alpha = 225^0$ position with respect to the posterior wall of the vessel.

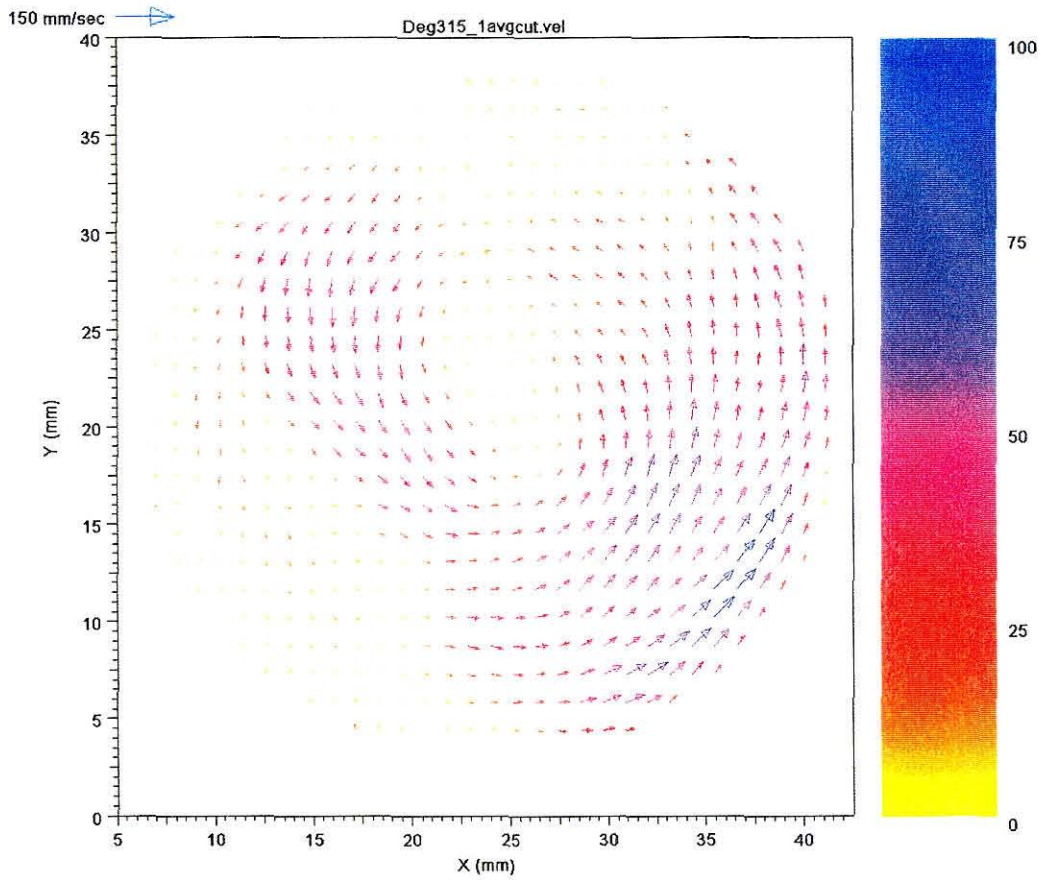

Figure 3.28: The secondary velocity field for the steady flow with upstream constriction $\beta = 80\%$ mounted in $\alpha = 315^0$ position with respect to the posterior wall of the vessel.

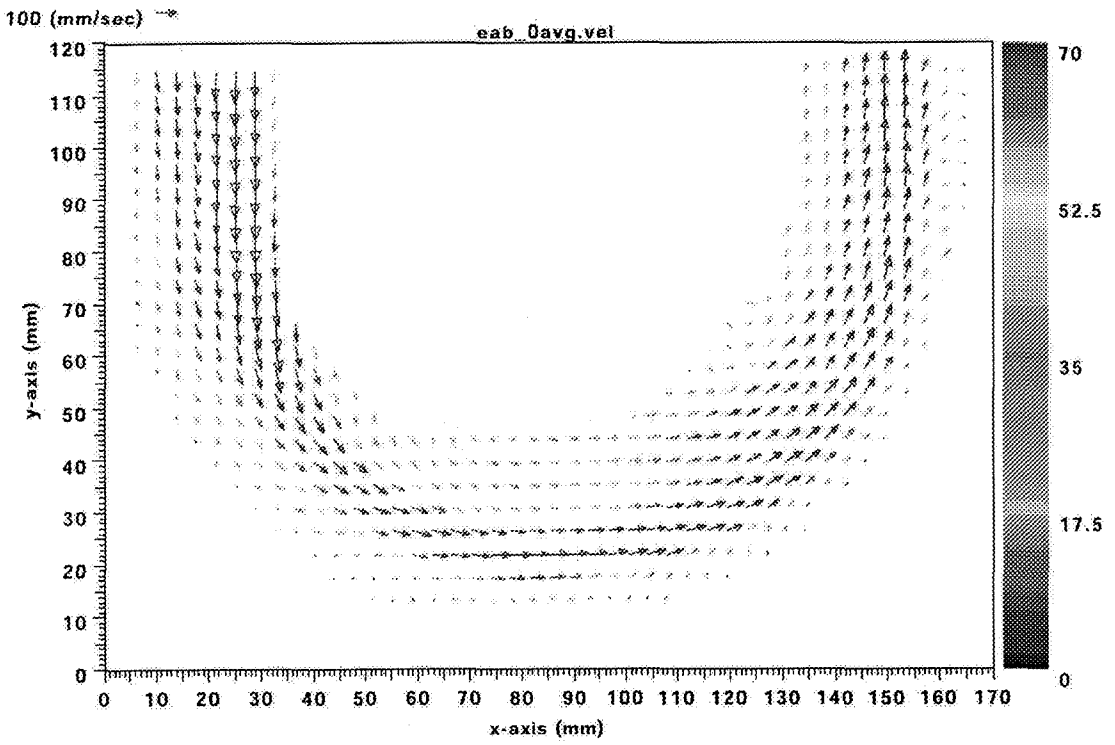

Figure 3.29: The axial velocity field for the steady flow without upstream constriction. $De = 3850$.

- In the case of upstream constriction, the impingement of the jet on the vessel wall is accompanied with a flow separation and reversal along the inner wall just at the beginning of the arch.
- The maximum axial velocity in the down stream flow shifts towards the outer bend.
- There is no separation in the downstream region of the arch.

3.4.2 Case II. Pulsatile Flow

Figures 3.32 and 3.34 show the pulsatile longitudinal flow field in the curved vessel model at two different phases of the flow cycle for the constricted flow. As it is seen the position of maximum axial velocity in the downstream flow shifts towards either the outer or the inner bend, according to the phase of the flow. This is an important

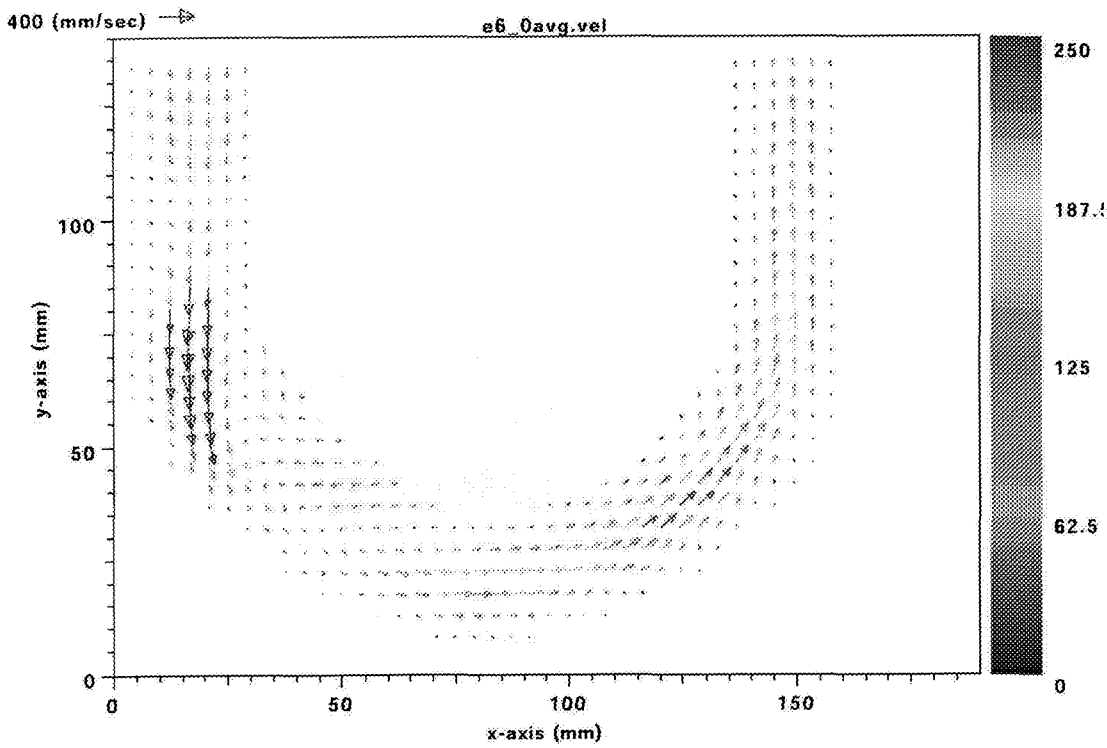

Figure 3.30: The axial velocity field for the steady flow with upstream constriction $\beta = 80\%$. $De = 3850$.

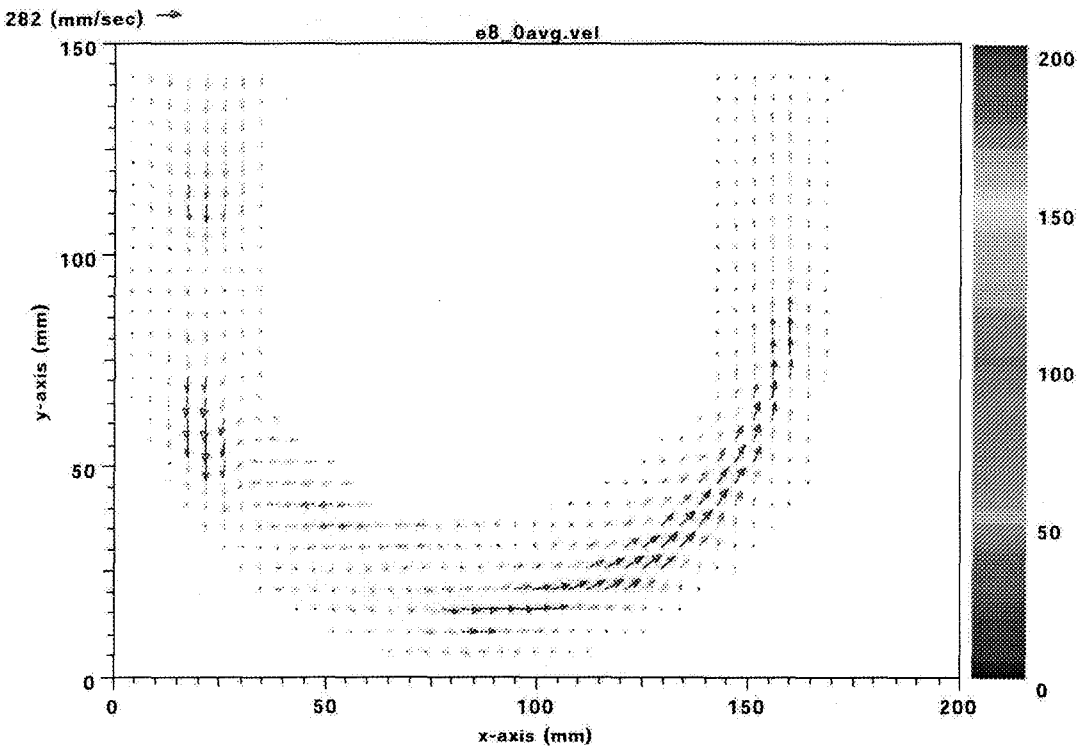

Figure 3.31: The axial velocity field for the steady flow with upstream constriction $\beta = 88\%$. $De = 3850$.

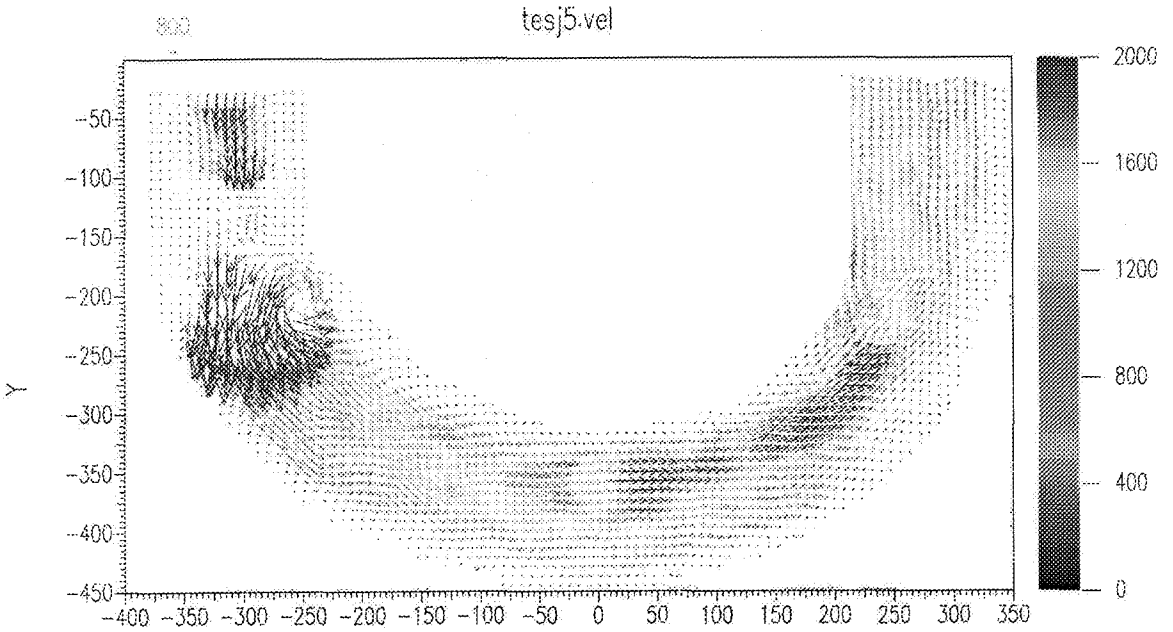

Figure 3.32: The axial velocity field for the pulsatile flow with upstream constriction $\beta = 80\%$. $\alpha = 12.6$. Note: the axis units in this image are in pixels.

observation because one of the unsolved issues or controversies regarding the flow in human aorta has been the position of maximum axial velocity for the longitudinal or axial flow. The position of maximum axial velocity, which is at the centerline for pipe flow, is shifted towards the outer bend in open channel flow in a curved conduit. The same phenomenon is expected in the flow in human aorta. However, there has been contradicting *in vivo* evidence regarding this question. Our result shows that this depends on the phase of the flow. This means that both cases can occur.

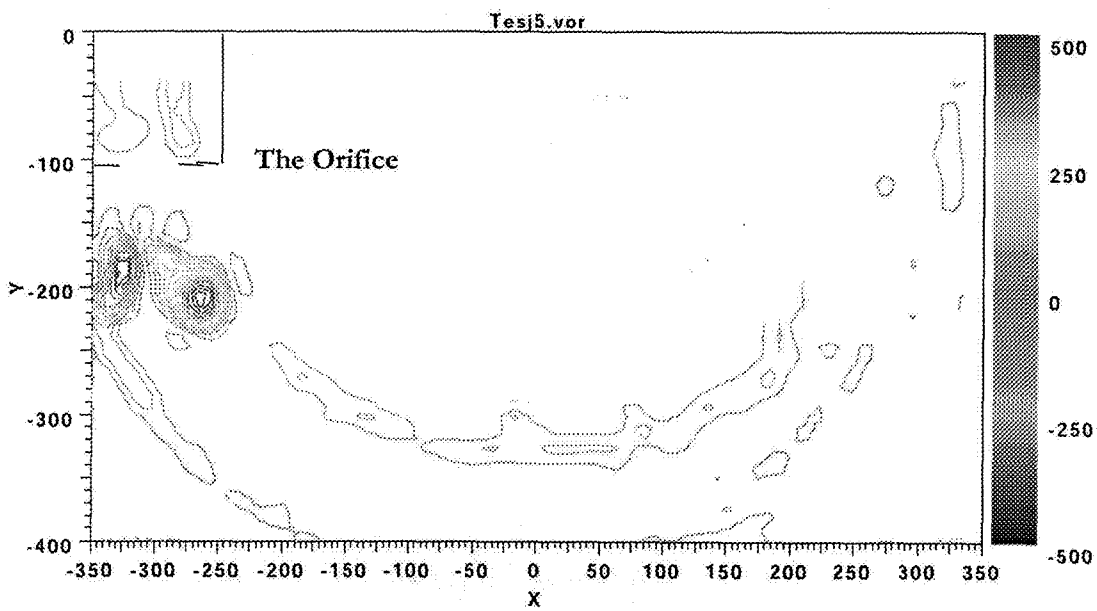

Figure 3.33: The vorticity field for the pulsatile flow with upstream constriction $\beta = 80\%$. $\alpha = 12.6$. This figure corresponds to the velocity field depicted in Figure 3.32. This figure shows the vortex ring formation at the orifice. Note: the axis units in this image are in pixels.

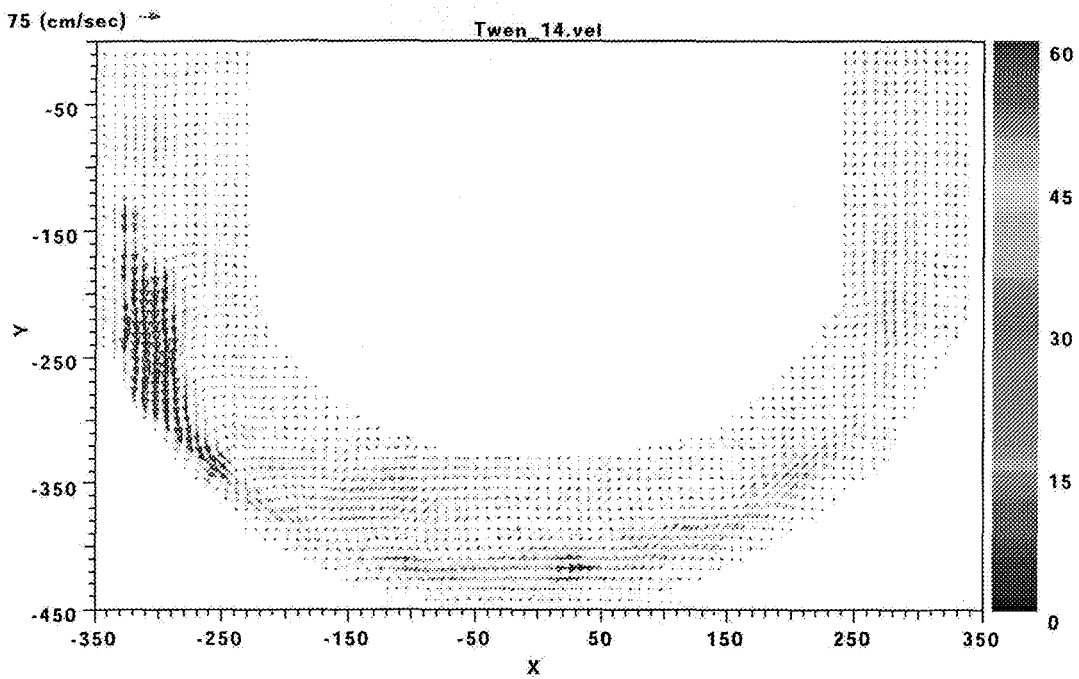

Figure 3.34: The axial velocity field for the pulsatile flow with upstream constriction $\beta = 80\%$. $\alpha = 8.6$. Note: the axis units in this image are in pixels.

3.5 Discussion

3.5.1 Secondary or Cross-sectional Flow

Our results obviously show that the effect of the incoming structures on the secondary flow patterns is very important. Even though this result may seem too obvious, but it has been completely neglected in all previous studies of the flow in curved vessels in general and aortic flow in particular. The only speculation about the non-uniqueness of the solution to the governing equations applying to this problem is by Pedley (1980). He does not go further to prove it theoretically and to find the other possible solutions. Our results shed light on a very important feature of the secondary flows in curved vessels, which demands systematic studies of these flow patterns experimentally and theoretically. This can be epitomized in the discovery of single circulation pattern for constrained flows, an entrance condition that resembles the actual physiological situation in aortic flow, as well as many industrial flows. The inconsistencies in the theories about the effect of the wall shear rate on the proper functioning of aorta and in the values reported for wall shear rates in aortic flow arise from this important result that there are at least two different secondary flow patterns in curved vessels. Our study not only reveals these different structures and their dependence on the spatial boundary conditions, but also provides detailed measurements of the location and the value of the maximum wall shear rate. The radial distributions of the blood cells in response to the flow field differ considerably in the case of the double circulation models used until now and the single circulation pattern observed in our studies. Another important factor revealed in the current study is the dependence of the sense of rotation of the single circulation patterns on the symmetry of the initial constriction. One important feature of our results is the difference between the direction of wall shear stress for three observed patterns of secondary flows. The main issues which our current research has revealed are:

- There is a bifurcation in the secondary flows which results from the spatial boundary conditions.

- The time periodicity of the flow does not change the secondary flow patterns but changes the location of the maximum secondary velocities towards the inner vessel wall.

- By putting an upstream constriction, the secondary flow patterns will change from a double-circulation (in the absence of a constriction) to a single circulation.

- The asymmetry of the upstream constriction will determine the sense of rotation of the single-circulation pattern. When the asymmetric constriction is moved from the posterior wall towards the anterior wall of the vessel, the rotation changes from a counterclockwise to a clockwise one.

- The wall shear stress, τ_w, is unidirectional for secondary flows with an upstream constriction, while it changes its direction for the secondary flow without an upstream constriction. This finding has important pathological consequences.

- For high constriction ratios, the longitudinal flow in the pulsatile flow is characterized by advancing vortex rings in the arch. Also, the position of maximum axial velocity depends on the phase of the flow.

Of these findings, the last two items have important pathological consequences. The studies by Malek *et al.*(1999) have shown that the proper response of the cells in the endothelial linings of blood vessels depends more crucially on the change of direction of shear stress than the value of the shear. Malek *et al.*(1999) claim that change of direction in the shear values are unfavorable for the endothelial linings of blood vessels. This is in accordance with our results.

Conjectural Hypothesis on Re-direction of Incoming Jet as the Cause of Single-circulation Patterns

Based on the fact that an asymmetry in the upstream constriction with respect to the anterior-posterior vessel wall position will lead to single-circulation patterns with

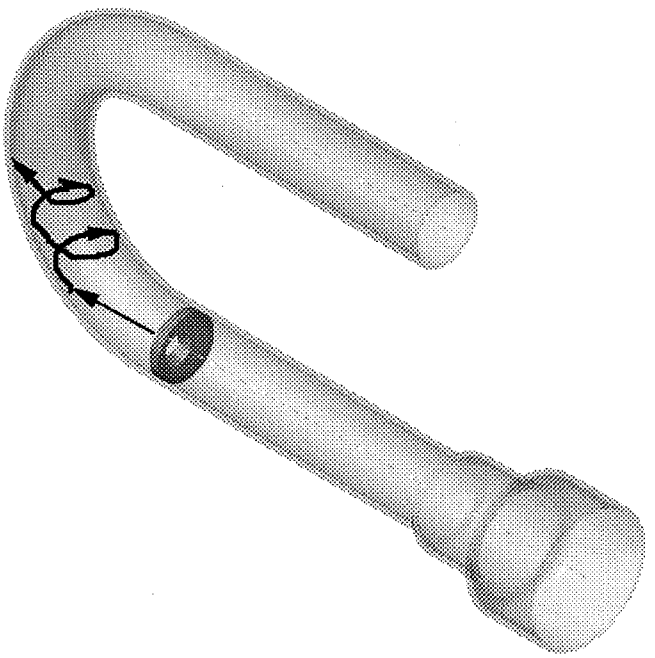

Figure 3.35: The clockwise re-direction of the incoming jet after impingement on the side of the anterior wall.

different sense of rotation, we propose the following scenario for the cause of new pattens for secondary flows in curved vessels:

- The incoming jet caused by the upstream constriction impinges on the vessel wall in the arch. The direction of the local curvature of the arch at the impingement point determines the clockwise and counter-clockwise rotation patterns, which arise from the helical movement of the jet in the arch.

- If the impingement point is closer to the anterior wall the clockwise scenario is depicted in Figure 3.35.

- If the impingement point is closer to the posterior wall the counter-clockwise scenario is depicted in Figure 3.36.

Recent clinical MRI studies by kilner based on the data for longitudinal flow suggest the possibility of such helical movements in the aortic arch(Mohiaddin 94). The more recent results by the same group give stronger evidence for such a possibility. In aortic flow the out of plane curvature of the aortic arch may play an important role in re-direction of the incoming jet.

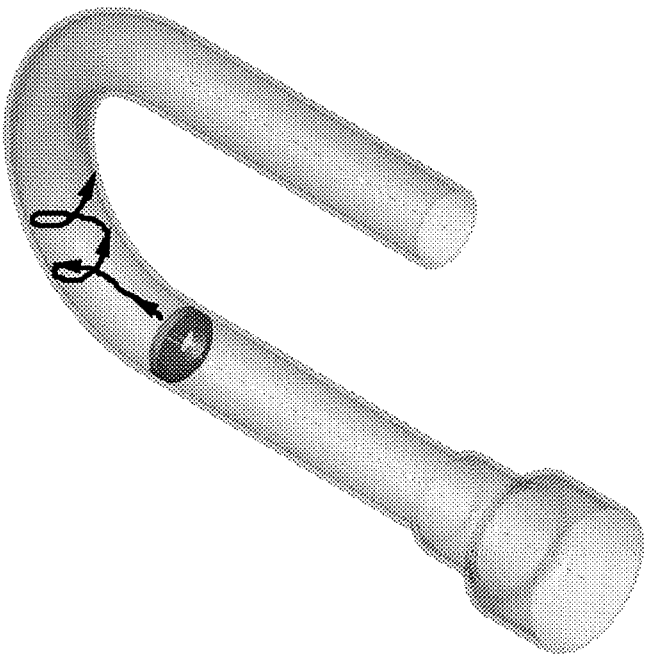

Figure 3.36: The counter-clockwise re-direction of the incoming jet after impingement on the side of the posterior wall.

3.5.2 Primary or Longitudinal Flow

Regarding the longitudinal or axial velocity field, our study reveals the following features for the steady flow:

- The flat incoming velocity profile without any upstream constriction leads to the shifting of the maximum axial velocity towards the outer bend.
- In the case of upstream constriction, the impingement of the jet on the vessel wall is accompanied with a flow separation and reversal along the inner wall just at the beginning of the arch.
- There is no separation in the downstream region of the arch.

For the pulsatile flow the longitudinal velocity field shows the following features:

- The flow entering the arch takes the form of vortex rings (Figure 3.33). This figure shows the vorticity field for the flow depicted in Figure 3.32. The vortex ring after the orifice is obvious.

- The position of the maximum axial velocity in the downstream flow depends on the phase of the flow cycle.

- There is no separation in the downstream region of the arch.

3.6 Further Work

There are still some unresolved issues surrounding the primary and secondary flow in curved vessels in general and in aorta in particular. Based on the results of the current work, the issues which need to be addressed in the future are:

- The transition from double-circulation to single-circulation pattern depends on the stenosis ratio, β. A novel design which allows the incremental variation of the upstream constriction will reveal when this transition occurs.

- The asymmetry of the upstream constriction and its effect on the sense of rotation in the arch has an important potential pathological consequences and it needs to be investigated in detail.

- The spatial resolution of the DPIV technique should be improved for the study of the behavior of secondary flows near the vessel wall. The mapping of the flow field near the physical boundaries is a major challenge for the technique of DPIV.

- The dependence of the sense of the rotation of single-circulation patterns on the relative position of orifice opening with respect to the anterior-posterior vessel wall axis suggests that the out of plane curvature of aorta may play an important role in the re-direction of the incoming jet in the arch. This conjecture needs careful study.

- The dependence of the position of the maximum axial velocity in the downstream flow on the phase of the flow needs careful study. The possible effect of Womersley number on this should be investigated in further detail.

- The effect of elastic walls and their interaction with secondary flow patterns is the next step in the research on aortic flow. Until now, researchers have only considered the interaction of double-circulation with elastic walls. With the discovery of new patterns, there is need to investigate this factor again.

Bibliography

[1] ADLER, M. 1934 Strömung in gekrümmten Rohren. *Z. Angew. Math. Mech.* **14**:257-275.

[2] ADRIAN, R. J. 1986b Multi-point optical measurements of simultaneous vectors in an unsteady flow-a review. *Int. J. Heat & Fluid Flow* . **7**:127-145.

[3] ADRIAN, R. J. 1991 Particle-imaging techniques for experimental fluid mechanics. *Annual Rev. Fluid Mech.* **22**:261-304.

[4] AGRAWAL, Y., TALBOT, L., GONG, K. 1978 Laser anemometer study of flow development in curved circular pipes. *J. Fluid Mech.* **85**:497-518.

[5] ALEXANDER, B. F., NG, K. C. 1991 Elimination of systematic-error in subpixel accuracy centroid estimation. *Opt. Eng.* **30**:1320-1331.

[6] BERGER, S.A., TALBOT, L., YAO, L.S. 1983 Flow in Curved Pipes. *Ann. Rev. Fluid Mech.* **15**:461–512.

[7] CARO, C. J., FITZ-GERALD, J. M., SHROTER, R. C., 1971 Atheroma and aterial wall shear: observation, correlation and proposal of a shear dependent mass transfer mechanism for atherogenesis. *Proc. R. Soc. London Ser. B.* **28**:109-159.

[8] CHANDRAN, K. B., SWANSON, W. M., GHISTA, D. M., 1974 Oscillatory flow in thin-walled curved elastic tubes *Ann. Biomedical Eng.* **2**:392-412.

[9] CHANDRAN, K. B., YEARWOOD, T. L., WIETING, D. N. 1979 An experimental study of pulsatile flow in a curved tube. *J. Biomech.* **12**:793-805.

[10] CHANDRAN, K. B., YEARWOOD, T. L., WIETING, D. N. 1979 An experimental study of pulsatile flow in a curved tube. *J. Biomech.* **12**:793-805.

[11] CHANG, L. J., TARBELL, J. M., 1985 Numerical-simulation of fully-developed sinusoidal and pulsatile (physiological) flow in curved tubes. *J. Fluid Mech.* **161**, 175-198.

[12] COLES, D. 1981 Prospects for useful research on coherent structure in turbulent shear flows. *Proc. Indian Acad. Sci. (Eng. Sci.).* **4**:111-127.

[13] DEAN, W. R. 1927 Note on the motion of fluid in a curved pipe. *Philos. Mag.* **20**:208-223.

[14] DEAN, W. R. 1928 The streamline motion of fluid in a curved pipe. *Philos. Mag.* **30**:673-693.

[15] EUSTICE, J., 1910 Flow of water in curved pipes. *Proc. R. Soc. London Ser. A.* **84**:107-118.

[16] EUSTICE, J. 1911 Experiments of streamline motion in curved pipes. *Proc. R. Soc. London Ser. A.* **85**:119-131.

[17] FRY D. L., 1968 Acute vascular endothelial changes associated with increased blood velocity gradients. *Circ. Res.* **22**:165-197.

[18] GHARIB, M., WILLERT C. 1990 Particle tracking-revisited, in Lecture Notes in Engineering: Advances in Fluid Mechanics Measurements 45, ed. M. Gadel-Hak, Springer-Verlag, New York, 109-126.

[19] GHARIB, M., WEIGAND A. 1996 Experimental studies of vortex disconnection and connection at a free surface. *J. Fluid Mech.* **321**:59-86.

[20] HAMAKIOTES, C. C., BERGER, S. A. 1988 Fully developed pulsatile flow in a curved pipe. *J. Fluid Mech.* **195**:23-55.

[21] HAMAKIOTES, C. C., BERGER, S. A. 1990 Periodic flows through curved tubes - the effect of the frequency parameter. *J. Fluid Mech.* **210**:353-370.

[22] LAMBOSSY, P. 1979 Oscillations forcees d'un liquide incompressible et viscueux dans un tube ridige et horizontal: calcul de la force de frottement. *Helvetica Physiologica Acta.* **25**:371-386.

[23] LIGHTHILL, M. J. 1975 *Mathematical Biofluid-dynamics.* Philadelphia: Soc. Ind. Appl. Math.

[24] MALEK A.M., ZHANG G., IZUMO S. 1994 Cytoskeletal Involvement and Cell-shape Contribution to Regulation of Endothelin-1 Gene-expression by Fluid Shear-stress *Circulation* **90**: (4) 292

[25] MALEK A.M., ALPER S.L., IZUMO S. 1999 Hemodynamic shear stress and its role in atherosclerosis. *JAMA-Journal of the American Medical Association* **282**: (21) 2035-2042

[26] MELLING A. 1997 Tracer particles and seeding for particle image velocimetry. *Meas. Sci. Technol.* **8**:1406-1416.

[27] MERZKIRCH, W. 1987 *Flow Visualization, 2nd Edition.* Academic Press, Orlando.

[28] MOHIADDIN R.H., YANG G.Z., KILNER P.J. 1994 Visualization of flow by vector analysis of multidirectional cine MR velocity mapping. *Journal of Computer Assisted Tomography* **18**: (3) 383-392

[29] PEARLSTEIN A. J., CARPENTER B. 1995 On the determination of solenoidal or compressible velocity fields from measurements of passive and reactive scalars. *Physics of Fluids.* **7**: No. 4, 754-763.

[30] PEDLEY, T. J. 1980 *The Fluid Mechanics of Large Blood Vessels.* Cambridge Univ. Press.

[31] RAFFEL, M., WILLERT, C., KOMPENHANS, J. 1998 Particle image velocimetry-a practical guide. Ed. R. J. Adrian, M. Gharib, W. Merzkirch, D. Rockwell, H. Whitelaw, Springer-Verlag, Heidelberg.

[32] RINDT, C. M., VANSTEENHOVEN, A. A., JANSSEN, J. D., *et al.,* 1991 Unsteady entrance flow in a 90-degrees curved tube. *Amsterdam: Assoc. Sci. Publ.* **226**:445-474.

[33] SHARP, M.K., *et al.,* 1991 Dispersion in a Curved Tube during Oscillatory Flow. *Journal of Fluid Mechanics.* **223**:537-563.

[34] SINGH, A. 1991 *Optic flow computation.* IEEE, Computer Society Press.

[35] SWANSON C.J. , STALP S. R., DONNELEY R. J. 1996 Experimental Investigation of Periodic-flow in Curved Pipes. *Journal of Fluid Mechanics.* **256**:69-83 NOV 1993.

[36] TADA, S., OSHIMA, S., YAMANE, R. 1996 Classification of pulsating flow patterns in curved pipes. *J. Biomechanical Eng.* **118**:311-317.

[37] TAYLOR, G. I. 1929 The criterion for turbulence in curved pipes. *Proc. R. Soc. London Ser. A.* **124**:243-249.

[38] TEXON, M., 1991 The hemodynamic basis of atherosclerosis - further observations - the linear lesion. *New York Acad. Med.* **62 (9)**: 875-880.

[39] THOMSON, J., 1876 On the origin of windings of rivers in alluvial plains, with remarks on the flow of water round bends in pipes. *Proc. R. Soc. London Ser. A.* **25**:5-8.

[40] THOMSON, J., 1877 Experimental demonstration in respect to the origin of windings of rivers in alluvial plains, and to the mode of flow

of water round bends of pipes. *Proc. R. Soc. London Ser. A.* **26**:356-357.

[41] WEIGAND, A. 1996 Simultaneous mapping of the velocity and deformation field at a free surface. *Exp. Fluids.* **20**:358-364.

[42] WESTERWEEL, J. 1985 Digital particle image velocimetry-Theory and application. Ph.D. Dissertation, Delft University Press, Delft.

[43] WESTERWEEL, J. 1997 Fundamentals of digital particle image velocimetry. *Meas. Sci. & Technol.* **8**:1379-1392.

[44] WHITE, C. M. 1929 Streamline flow through curved pipes. *Proc. R. Soc. London Ser. A.* **123**:645-663.

[45] WILLERT, C.E., GHARIB, M. 1991 Digital Particle Image Velocimetry. *Experiemnts in Fluids.* **10**:181-193.

[46] WILLERT, C., GHARIB M. 1997 The interaction of spatially modulated vortex pairs with free surfaces. *J. Fluid Mech.* **345**:227-250.

[47] WILLIAMS, G. S., HUBBELL, C. W., FENKELL, G. H., 1902 Experiments at Detroit, Mich., on the effect of curvature upon the flow of water in pipes. *Trans. ASCE.* **471**-196.

[48] WITZIG, K., 1914 Uber erzwungene Wellenbewegungen zaher, inkompressibler Flussigkeiten in elastischen Rohren. *Inaug. Diss. Bern. Bern: Wyss.*

[49] WOLSTRAHOLME, G. E. W., KNIGHT, J., 1973 CIBA Symp *Amsterdam: Assoc. Sci. Publ.*

[50] WOMERSLEY, J. R. 1957 The mathematical study of the arterial circulation in a state of oscillatory motion. *Tech. Rep. WADC - TR 56-614, Wright Air Dev. Cent.*

[51] YAO, L. S., BERGER, S. A. 1975 Entry flow in a curved pipe. *J. Fluid Mech.* **67**:177-210.

[52] ZALOSH, R. G., NELSON, W. G. 1991 Pulsating flow in a curved tube. *J. Fluid Mech.* **59**:693-705.

Appendix A

Digital Particle Image Velocimetry (DPIV)

A.1 Principle

The digital particle image velocimetry (DPIV) is a non-intrusive optical technique that permits the mapping of instantaneous velocity field through a selected two-dimensional slice of a flow. This method can be used for mapping of three-dimensional flows as well. However, to study the secondary flows in the present work, the two-dimensional DPIV is needed and we confine our description here to the two-dimensional DPIV. The method is particularly suitable for investigating unsteady flows, whether periodic or transient. In DPIV, a plane of light is positioned parallel to the camera's sensor. Video or photography is used to record images of seeding particles moving within the laser sheet. Analysis of the multiple images yields velocity magnitudes and directions throughout the illuminated flow plane. Quantitative flow visualization has many roots and has taken several approaches. The advent of digital image processing has made it possible to extract practically useful information from every kind of flow image. In a direct approach, the image intensity or color (wavelength or frequency) can be used as an indication of concentration, density and temperature fields or of gra-

dients of these scalar fields in the flow (Merzkirch 1987). These effects can be part of the inherent dynamics of the flow (*e.g.*, gradients of density are used in shadowgraph and Schlieren techniques) or generated through the introduction of optically passive or active dye agents tracers, liquid crystals, or various molecular tagging schemes.

In general, the optical flow or the motion of intensity fields can be obtained through time sequenced images (Singh 1991). For example, the motion of patterns generated by dye, clouds or particles can be used to obtain such a time sequence. The main problem with using a continuous-intensity pattern generated by scalar fields (*e.g.*, dye patterns) is that it must by fully resolved (space/time) and contain variations of intensity at all scales before mean and turbulent velocity information can be obtained (Pearlstein 1995). In this respect, the discrete nature of images generated by seeding particles has made particle tracking the method of choice for whole field velocimetry. The technique recovers the instantaneous two and three-dimensional velocity vector fields from multiple photographic images of a particle field within a plane or volumetric slab of a seeded flow, which is illuminated by a light source. Various methods for individual tracking of particles can be used to obtain the displacement information and subsequently the velocity fields. The spatial resolution of this method depends on the number density of the particles. A major drawback in tracking individual particles has been the unacceptable degree of manual work that is required to obtain the velocity field from a large number of traces

or particle images. Digital imaging techniques have helped to make particle tracking less laborious (Gharib & Willert 1990). However, because of the errors involved in identifying particle pairs in high particle-density images, the design of an automatic particle tracking method, especially for three-dimensional flows, has been extremely challenging. Therefore, applications of the automatic particle tracking methods have been limited to low particle density images. In this respect, an alternative method which concentrates on following a pattern of particles has been implemented by various investigators in order to resolve the above mentioned issues with a particle tracking method. This method is known as particle image velocimetry. The method returns to the fundamental definition of velocity by estimating the velocity from

$$U(t_0, x) = \lim_{\Delta t \to 0} \frac{[x(t_0) - x(t_0 + \Delta t)]}{(\gamma \Delta t)} \tag{A.1}$$

where $x = x(x, y)$ describes the position of a particle image, Δt is the time separating the two exposures and γ is a scaling factor. Since the flow motion is reflected by the motion of visible seeding particles, velocities cannot be determined at the place where no particles are present. Thus, high particle seeding density is usually required for a detailed representation of the velocity field. In DPIV the particle seeding density is so high that each single particle track can no longer be recognized. Instead of determining the displacement of each single particle inside the light sheet, the local particle displacement is defined as that of a group of particles. This group of particles is usually referred

to as interrogation area, interrogation spot or spatial sub sample of two successive video images. The average displacement of this group of particles is considered to be the local displacement at the geometry center of the interrogation area. The whole velocity field is obtained when each desired point in the flow picture has been interrogated.

The correlation function of an image gives a measure of the periodic nature of that image. The function is computed using two-dimensional fast Fourier transforms (FFTs) for high efficiency. A typical PIV image will yield a cross correlation function consisting of one or more peaks distributed non-symmetrically. The spatial position of the main peak within the cross-correlation image gives the average frequency of the multiple particle separation in the DPIV image. This information is then combined with the time separation to give the average velocity of the particles in the image. Cross-correlation offers the advantage of easy directional resolution as there is no 180-degree ambiguity as for autocorrelation, but requires a high recording rate. Most correlation functions have more than one frequency peak within the image. These peaks are due to particles correlating with other particles rather than themselves. These peaks which are usually of lower amplitude can be thought of as noise, and can occasionally give spurious results. A high cross-correlation value near I is observed where many particle images match up with their corresponding spatially shifted partners. Small cross-correlation peaks may be observed when individual particle images match up with other particle images. The highest correlation peak

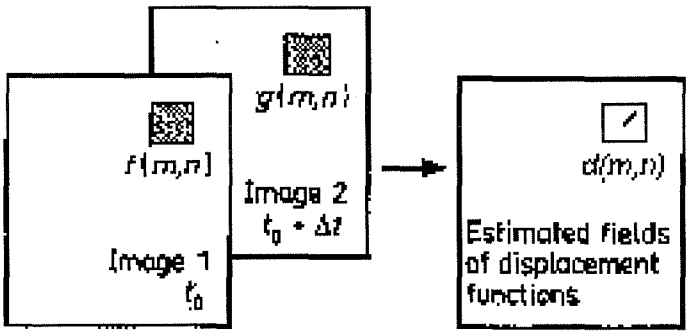

Figure A.1: Conceptual arrangement of frame-to-frame sub sampling associated with digital particle image velocimetry. Division of the displacement by the time scale between the capture of the images gives the average velocity in the sampled region.

is considered to represent the best match of particle images.

A.2 The Technique of Cross-correlation

A digitized video image may be considered to be a two-dimensional signal field analogous to a digital time series in one dimension. Many one-dimensional signal processing techniques can be readily extended to two dimensions.

In DPIV, two sequential digital images are subsampled at one particular area via an interrogation window (Figure A.1). Within these image samples an average spatial shift of particles may be observed from one sample to its counterpart in the other image, provided a flow is present in the illuminated plane. This spatial shift may be described quite simply with a linear digital signal-processing shown in Figure A.2. One of the sampled regions obtained through an interrogation window, $f(m, n)$ may be considered the input to a system whose output $g(m, n)$ corresponds to the sampled region of another image taken a time Δt

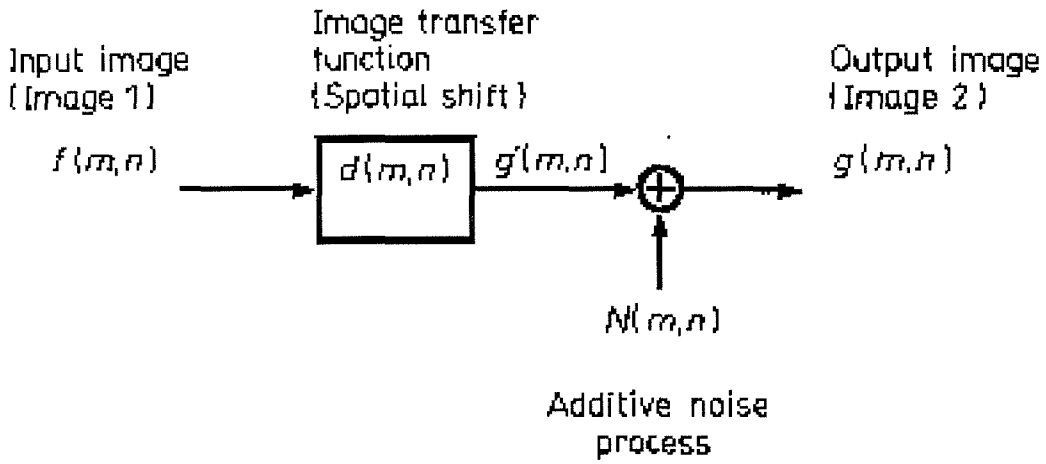

Figure A.2: The digital signal processing block diagram for DPIV.

later. The system itself consists of two components, a spatial displacement function $d(m,n)$ (also known as the system's impulse response) and an additive noise process $N(m,n)$. This noise process is a direct result of particles moving off the sampling region, particles disappearing through three-dimensional motions in the laser sheet, the total number of particles present in the window and other components that may add to the measurement uncertainty. Of course the original sample $f(m,n)$ and $g(m,n)$ may be noisy as well. The major task in DPIV is the estimation of the spatial shifting function $d(m,n)$, but the presence of noise $N(m,n)$ complicates this estimation. A description of how the output sample $g(m,n)$ relates to the input sample $/f(m,n)$ can be given mathematically through the use of the discrete cross-correlation function.

The technique of deconvolution and cross-correlation in DPIV is described in detail by Willert and Gharib (1991).

A.2.1 Peak Finding

Perhaps the most important step in DPIV is locating the position of the correlation peak to sub-pixel accuracies. Typically, correlation results without special peak finding schemes are accurate only to within +/- half pixels. However, with peak finding schemes, it is possible to obtain accuracies as low as 0.01pixels. Several sub-pixel peak finding schemes have been studied. Centroiding (Alexander & Ng 1991), defined as the ratio of the first order moment to the zeroth order moment has been used initialy, and required that the correlation domain be thresholded in order to define the region containing the correlation peak. For fractional displacements, this scheme strongly biases the sub-pixel measurements towards integer values (Westerweel 1997); an effect referred to as "peak-locking." For particle images in the $2-3$ pixel range, more reliable methods such as parabolic and Gaussian curve fits (Westerweel 1993; Willert & Gharib 1991) have also been developed. Of these, the Gaussian three-point curve fit produces the least uncertainty since the cross-correlation peak itself displays a Gaussian intensity profile (Westerweel 1993; Raffel, *et al.* 1998).

A.3 Illumination System and Seeding Particles

For most fluid flow applications, experiments are performed either in air or water. Since these fluids are transparent, the flow must be quantitatively visualized through the use and motion of flow markers. Figure

A.5 shows a standard acquisition setup for DPIV image acquisition. In water, fluorescent, polystyrene, silver-coated particles, or other highly reflective particles must be used to seed the flow; while olive oil or alcohol droplets are generally used in wind tunnels. Since the fluid velocity is inferred from the particle velocity, it is important to select markers that will follow the flow to within acceptable uncertainties without affecting the fluid properties that are to be measured. This implies that the fluid marker must be small enough to minimize velocity differences across its dimensions, and to have a density as close as possible to the density of the fluid being measured. Further discussions of types of particles, and error analysis associated with particle motion, is given by Merzkirch (1987), Adrian (1986b, 1991), and Melling (1997). Upon proper selection, the particles are illuminated with a pulsed laser sheet, most typically a Nd:YAG laser. The images of the reflected particles are then acquired with a CCD camera, typically at a 30 frame per second video rate, where each image is singly exposed. Though this video rate may seem too slow, the DPIV technique has overcome this limitation through the evolution of the CCD chip, which shall be discussed in the following sections. The images are captured onto digital memory using a computerized data acquisition system. Finally, the shift of the particle images between sequential image pairs is measured using a cross-correlation technique. As the process is entirely digital, we refer to this approach as digital particle image velocimetry or DPIV. In our experiments a pulsed YAG laser (Nd:YAG,$\lambda = 532nm$) is used as

light source to illuminate the flow region. The light sheet is formed by using a cylindrical lens (focal length $f = 6.4mm$). This type of laser is likely to provide the best results since it can produce very high power (30 $J/pulse$) over a very short time span, thus freezing the motion of the particle images. The pulsed Nd:YAG laser requires a high voltage period of at least 3 us to be externally triggered. Generally, particle images in video-based DPIV should have good contrast. Suitable exposed images are obtained by choosing the adequate laser light intensity as well as the suitable shutter time. Too long exposure time will result in particle images being blurred and overlapped. The suitable exposure time makes the tracer particle images to appear circular. Since the fluid flow investigated is water, the tracer particle's density must match the density of water. If the particles are fine enough, their motion is assumed to follow the flow exactly. It is rather easy to satisfy this condition. However, it is more difficult to satisfy the two other requirements: small size and high light scattering, *i.e.*, have as large as possible surface reflection index. The size deviation of seeding particles should be as small as possible, otherwise the small particles will contribute to the background noise due to the poor spatial resolution of CCD chips (see section A.5). This again will result in poor contrast of particle images. Figure A.3 shows portions of two typical DPIV images.

In vortical flows the shearing action will generate lift on the particle. Ideally, the seeding particles should be as small as possible, yet scatter

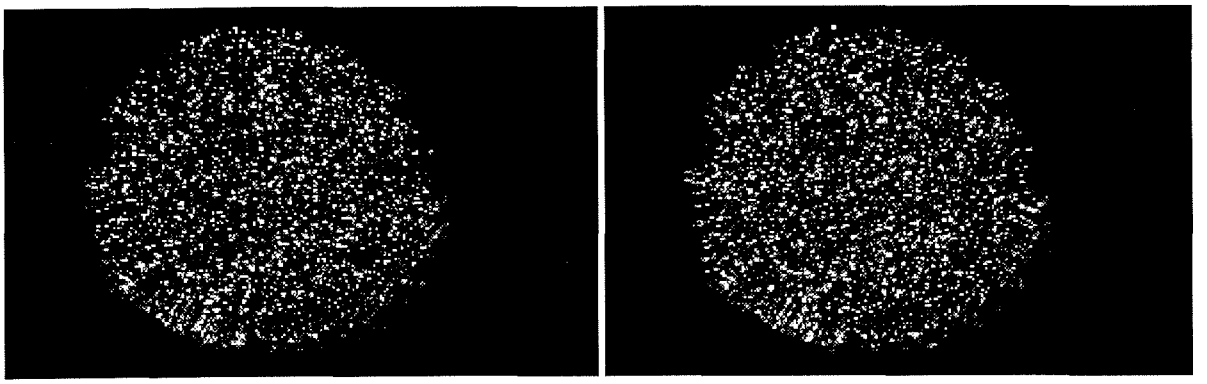

Figure A.3: The images show two sub samples of $768X480$ pixels. The displacement of the pattern can clearly be identified. A cross-correlation of these interrogation windows would result in a 'left-downward' pointing vector at the center of the image.

enough light to provide a good signal-to-noise ratio. In the present work we use either silver-coated hollow glass spheres with a diameter of approximately $14\mu m$ or fluorescent particles with a diameter of $80 - 100$ *mesh* and a specific weight of approximately 1.1.

A.4 Timing

The Nyquist sampling criterion associated with the discrete Fourier transforms limits the maximum recoverable spatial displacement in any sampling direction to half the window size in that direction. In reality, this displacement is often too large for the technique to work properly, since the signal to noise ratio in the cross-correlation decreases with increasing spatial shift. That means that the number of particle image pairings decreases in the sampling region while more particle images are unpaired. Given a window side of length N, a third of this length (*i.e.*, $N/3$) is an adequate limit for recoverability of the displacement vector. In the following we try to quantify the time scale between the capture

of two images. This simple approach gives usually a good estimate of Δt. The mean flow velocity of the region of interest is U $[cm/s]$ we then can define the scaling factor (see equation A.1):

$$\gamma = N/D \ pixels/cm \tag{A.2}$$

where N describes the number of pixels necessary to represent the length $D[cm]$ on the set-up. The propagation velocity of the particles U_p is

$$U_p = \gamma.U \ pixels/sec \tag{A.3}$$

The displacement of a tracer particle should not exceed a third of the sub sample window. Therefore the time between two images corresponding to a pair should satisfy:

$$t_3 = n/U_p \tag{A.4}$$

where n is the maximum allowable displacement in pixels ($n = N/3$) of the particles. The cross-correlation peak is initialy determined by finding the highest value in the two-dimensional array of correlation values. Around this element a parabolic or exponential curve fit in both the horizontal and vertical direction yields the approximate location of the correlation peak to sub-pixel accuracy.

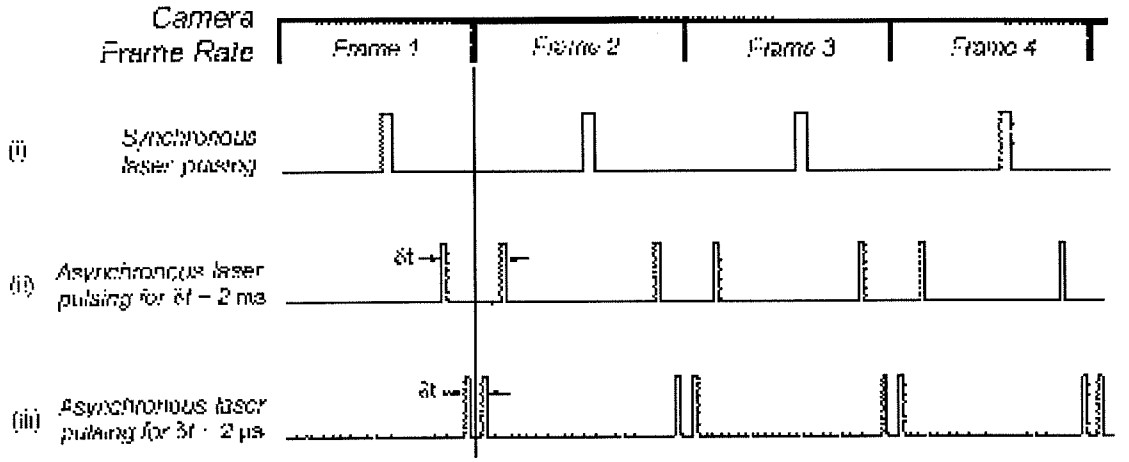

Figure A.4: The timing diagram for the DPIV acquisition sequence.

A.4.1 The Timing Diagram

This section describes the timing sequence of the DPIV acquisition system.

A pulse generating device (timing box) is used to control the shutter times, t_{e1}, t_{e2}, of two consecutive images as well as the time shift Δt between the two exposures. Basically a frame, *i.e.*, an image, is constituted of both an odd and an even field. As shown in Figure A.4 the falling edge of the delay, t_d, determines the exposure of the first image during the frame integration period of the CCD chip. The second delay is the time shift (Δt) between the two images constituting an image pair. The CCD camera we use attains exposure times as short as 4 ms. Section A.5 describes the connection of the timing box to the recording configuration we use.

A.5 Recording and Grabbing of Particle Images

In order to get the original data base, the first step of video-based DPIV is to record and grab the particle images. As described earlier, images are acquired with a CCD camera. An understanding of CCD cameras is therefore imperative in order to be able to take full advantage of their features. CCD cameras contain an array of photosensitive pixels that are sensitive to light. Standard CCD video cameras are capable of acquiring video at 30 frames per second. The full-frame CCD cameras read out pixel values sequentially in a row-by-row manner, requiring almost one full frame time ($1/30sec$) to read out completely. This presented a severe limitation, as this type of CCD necessitated the light source to be pulsed at exactly the same location frame. Therefore, initial applications of DPIV were limited to slow flows, since sequential images could only be pulsed synchronously at $1/30$ *second* time difference. To overcome this limitation, Dabiri & Roesgen (1991) suggested exposing each frame asynchronously. To do so, they suggested using the frame transfer CCD. This CCD is exactly the same as a full frame CCD, except that the lower half is masked off and used only for storage. Using the frame transfer CCD marked a significant improvement as shifting the image from the exposed section to the masked-off section took 2 milliseconds, making it possible to reduce the time separation between the laser exposure pulses to 2 milliseconds. This increased the use of DPIV to study fluid flows that were one order of magnitude

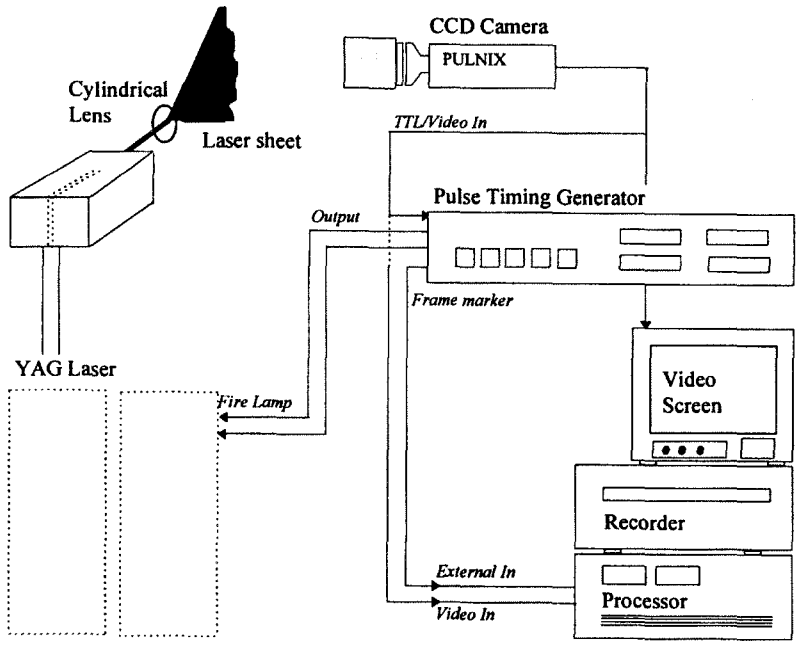

Figure A.5: System configuration for image grabbing.

faster than what had been previously possible (Willert & Gharib 1997; Weigand 1996; Weigand & Gharib 1996). Most recently, the full-frame interline transfer CCD has allowed even shorter pulse separations to be implemented for DPIV. Rather than use half of the CCD array as storage, this CCD placed the masked storage area adjacent to the pixel itself, making the total image shift time into storage approximately 1 microsecond. This vastly broadened the applications of DPIV to study even faster fluid flows as it reduced the pulse separation by 3 orders of magnitude with respect to the frame transfer CCD and 4 orders of magnitude with respect to the full frame CCD.

The raw images are obtained by digitizing the video signals directly from a CCD (charged coupled device) camera (PULNIX). The objective

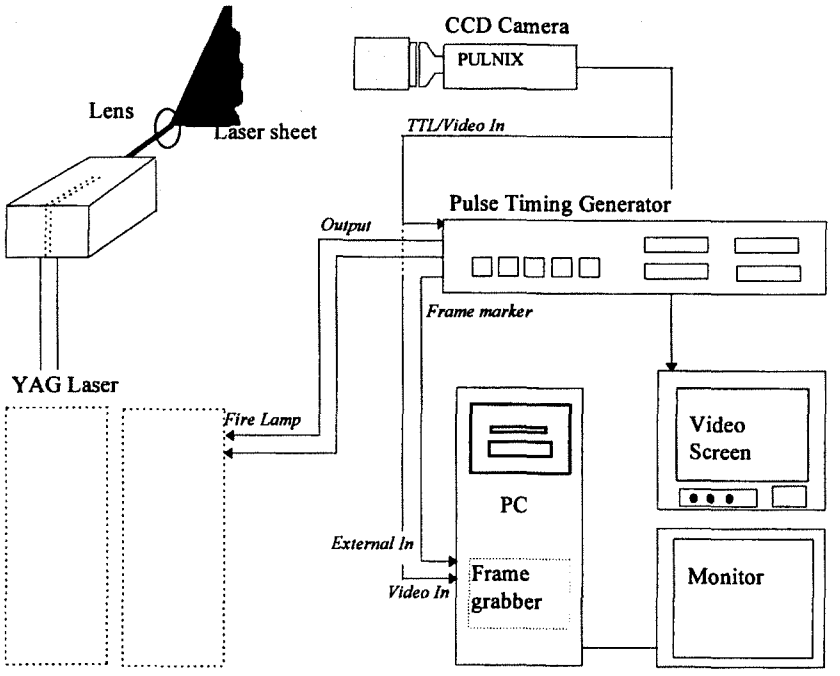

Figure A.6: System configuration for laser-disc recording.

mounted on the camera is a *Nikon* 70−2 10*mm* zoom. The camera has a resolution of 768*pixels* horizontally and 480 *pixels* vertically. Each pixel has a resolution of 8 *bits*, allowing 256 possible gray levels. These levels are usually assigned integer values ranging from 0 to 255, with 0 representing the darkest intensity level. The CCDs transfer electric charge from the light transducer to the electronic circuit that encodes the resultant current into a video signal. The frame rate of the camera ($30Hz$) is input to a timing box that controls the pulse rate of the YAG:Nd Laser.

Two modes of data acquisition are available. A frame grabber (EPIX 10) installed on a Pentium computer (120 MHz) digitizes images into the a frame buffer. This mode (*i.e.*, the buffer, 4 MB) limits the

number of digitized image to 5 pairs. The system configuration for this mode is shown in Figure A.5. Continuous recording is achieved by the use of a Videodisk system (Player-LVR-6000A and Processor-LVS-6000AP). The Video images can be recorded onto laser videodisks in frame mode, at 30 $frames/second$. Images can be downloaded to the memory of the computer using a serial port RS 170 (see Figure A.5). The second stage of the experiments was carried on an updated system, which used a Pentium computer (450 MHz) with a CORECO frame grabber. This system also allowed the possibility of real time downloading of the images, which facilitates the processing and timing check procedure.

A.6 Error Sources

A.6.1 Particle Seeding

Non homogeneous particle size particle geometry and quality (oxidation after a few days) density and size (particles following the dynamics of the fluid motion) low particle density may reduce processing accuracy (occurrence) strong velocity gradients inside the interrogation area. A more detailed account of error sources in DPIV can be found in Huang *et al.*(1997).

- Not enough particle pairs due to flow components perpendicular to laser sheet (3D-flow effects).
- The size of the seeding particles are not in conjunction with the

scale and the resolution of the CCD array.

A.6.2 Image Acquisition

- image distortion due to lens error
- misalignment of camera
- light reflections due to misalignment of optical lenses
- image sharpening, exposure time
- different intensity of the particle images (misalignment of the laser beams)

A.6.3 Image Processing

- noise of the video camera
- noise of ADIO conversion
- bad correlation peak (due to high signal to noise ratio)

Appendix B. Figures

B.1 Figures for the Curved Vessel Experiment

The velocity and vorticity fields for the curved vessel experiment are presented in this section. The flow signals for the pulsatile case is also shown. The Dean number, Reynolds number and Womersley number (for the pulsatile flow) are shown for each case. Note: Unless explicitly stated otherwise, in all images in this section the inner bend is located at the right part of the circle and the outer bend is located at the left part of the circle.

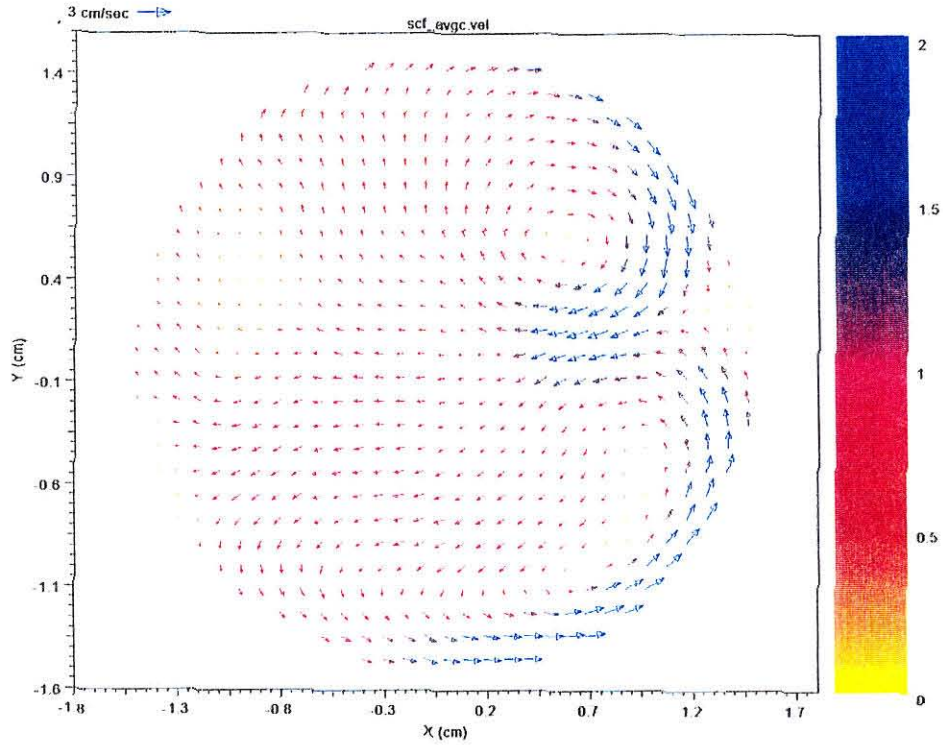

Figure B.1: The velocity field of the steady flow in the curved vessel model without upstream constriction. De = 3850.

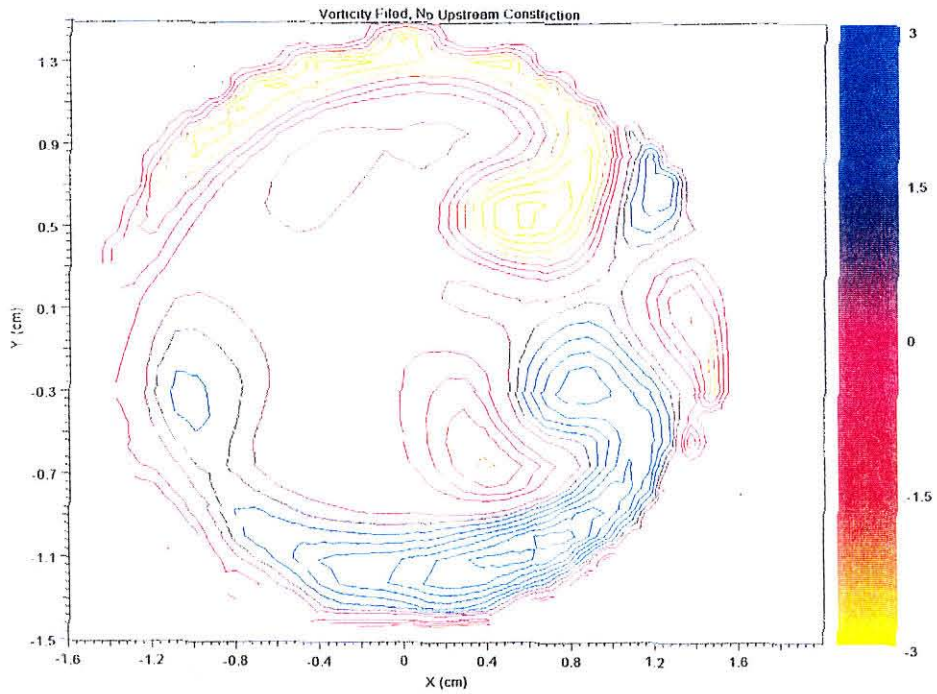

Figure B.2: The vorticity field of the steady flow in the curved vessel model without upstream constriction. De = 3850.

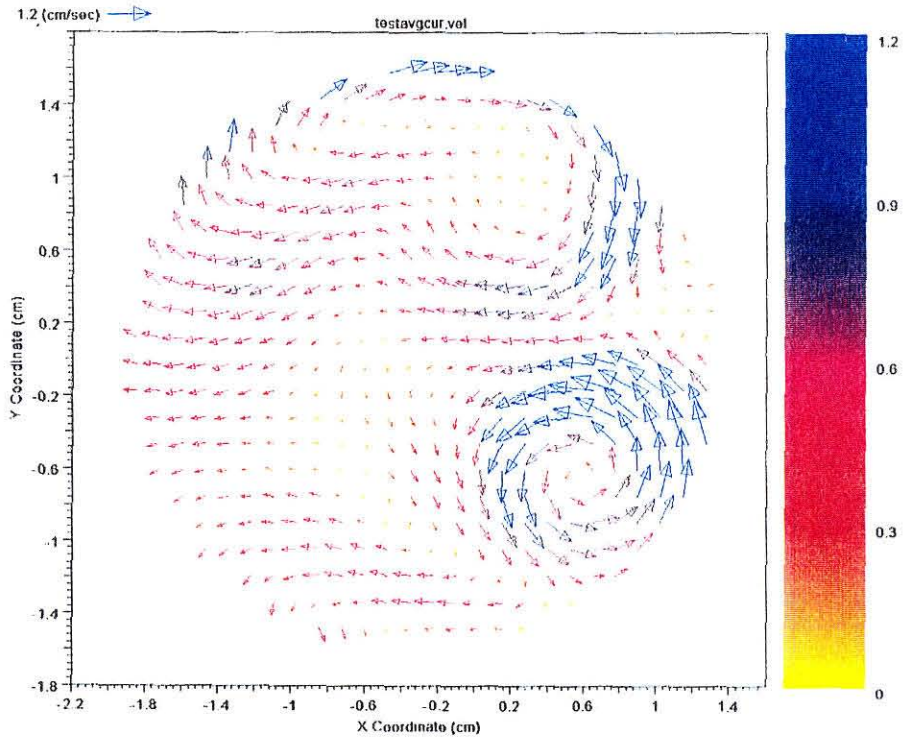

Figure B.3: The velocity field of the pulsatile flow in the curved vessel model without upstream constriction. $\alpha = 12.5$.

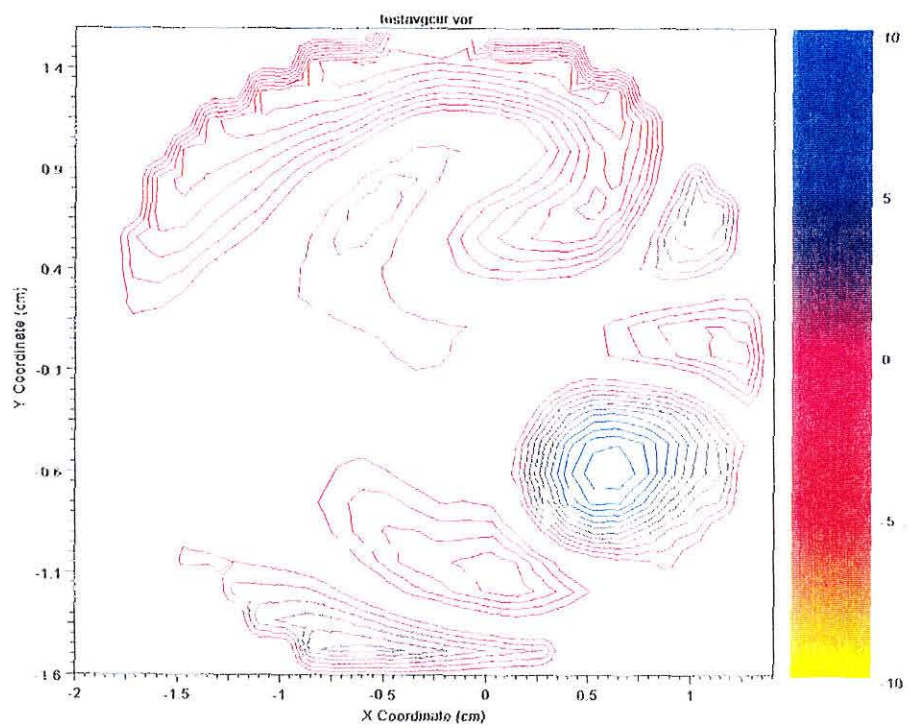

Figure B.4: The vorticity field of the pulsatile flow in the curved vessel model without upstream constriction. $\alpha = 12.5$.

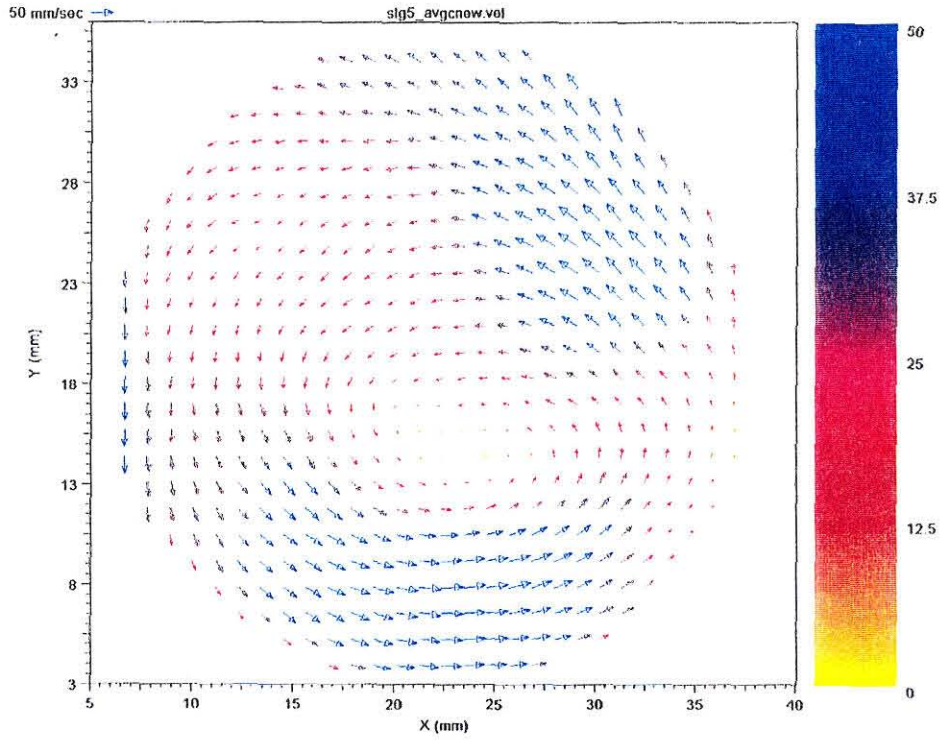

Figure B.5: The velocity field of the steady flow in the curved vessel model with upstream constriction $\beta = 65\%$.

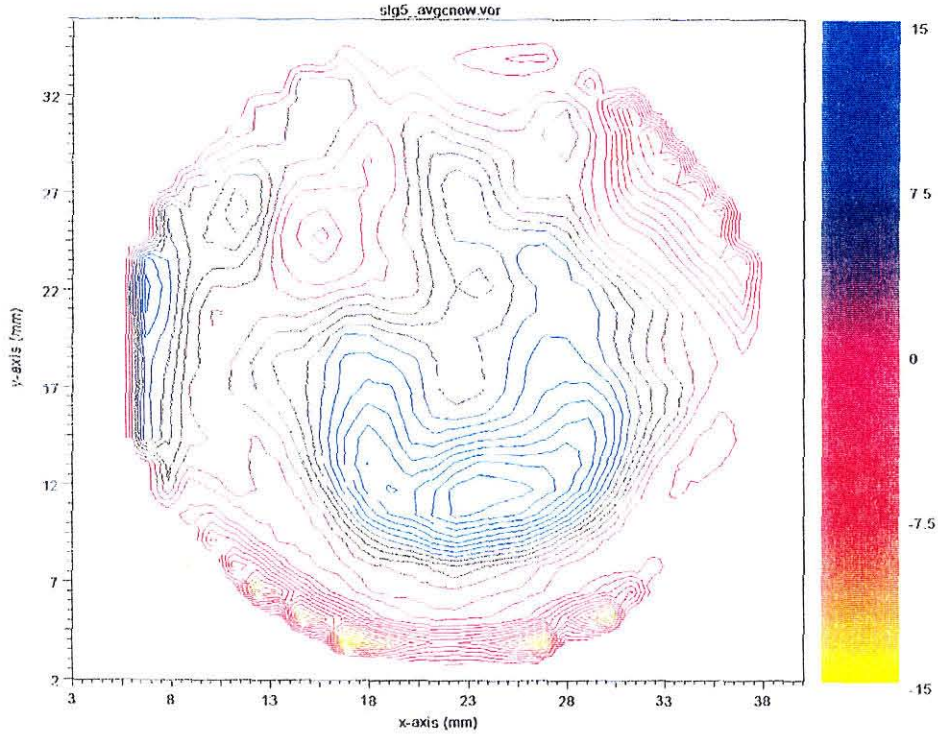

Figure B.6: The vorticity field of the steady flow in the curved vessel model with upstream constriction $\beta = 65\%$.

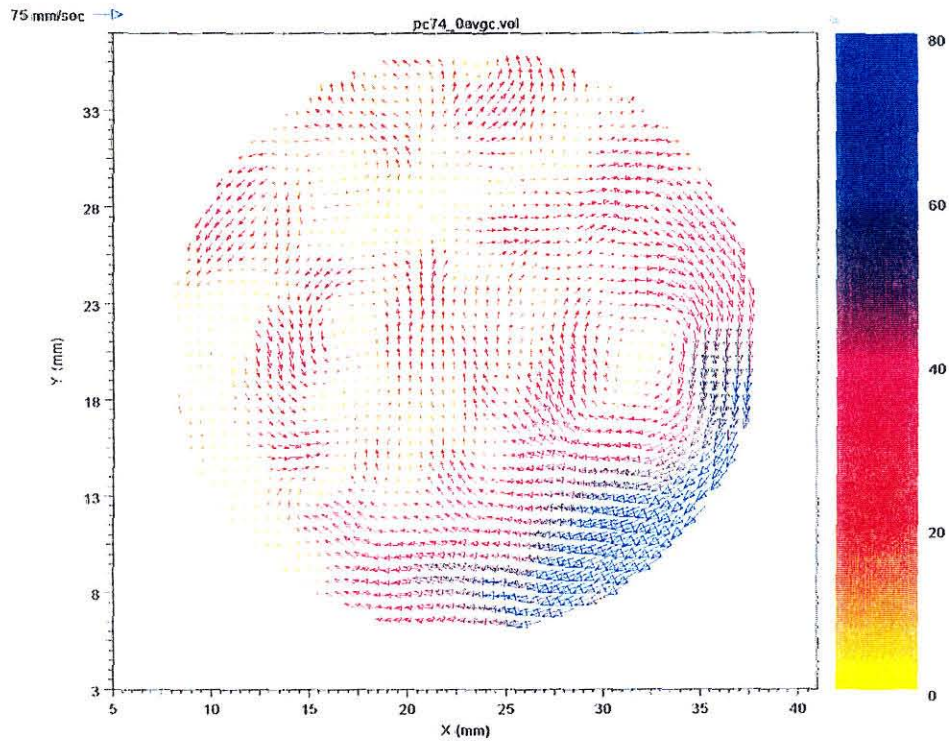

Figure B.7: The velocity field of the pulsatile flow in the curved vessel model with upstream constriction $\beta = 88\%$.

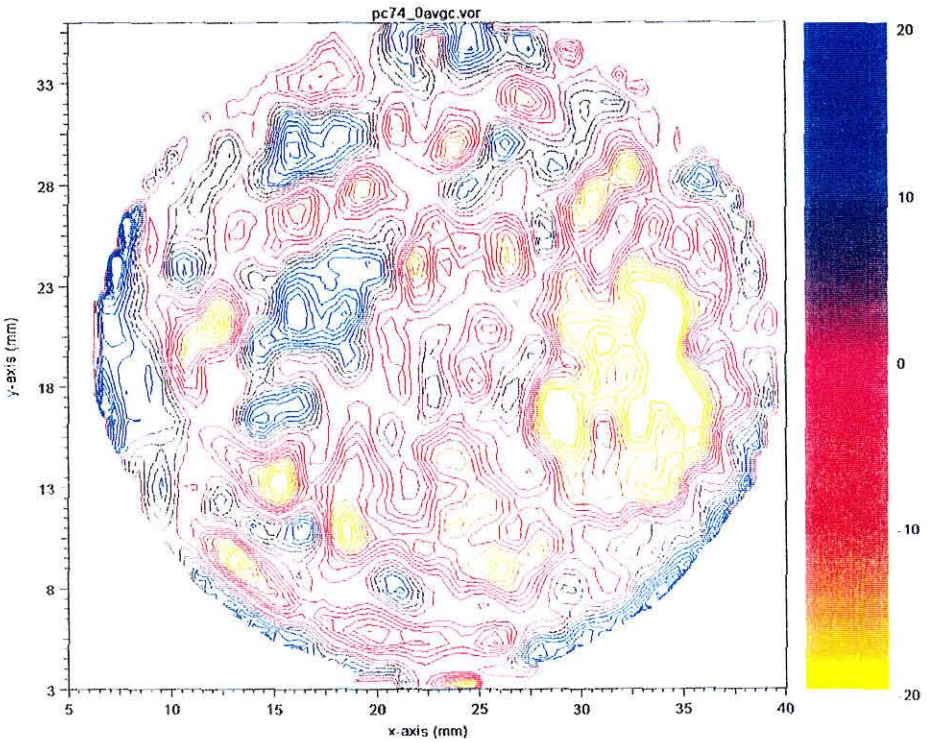

Figure B.8: The vorticity field of the pulsatile flow in the curved vessel model with upstream constriction $\beta = 88\%$.

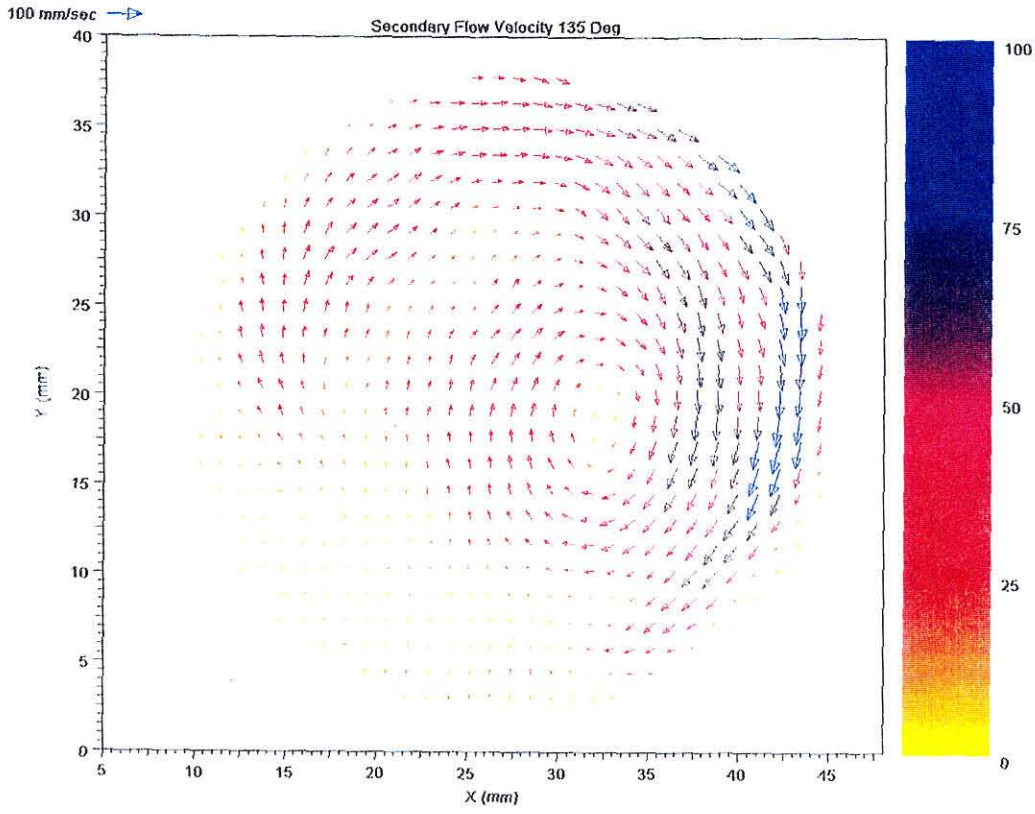

Figure B.9: The velocity field of the pulsatile flow in the curved vessel model with upstream constriction $\beta = 80\%$ asymmetrically positioned at 135^0 with respect to the posterior wall. $\alpha = 12.6$.

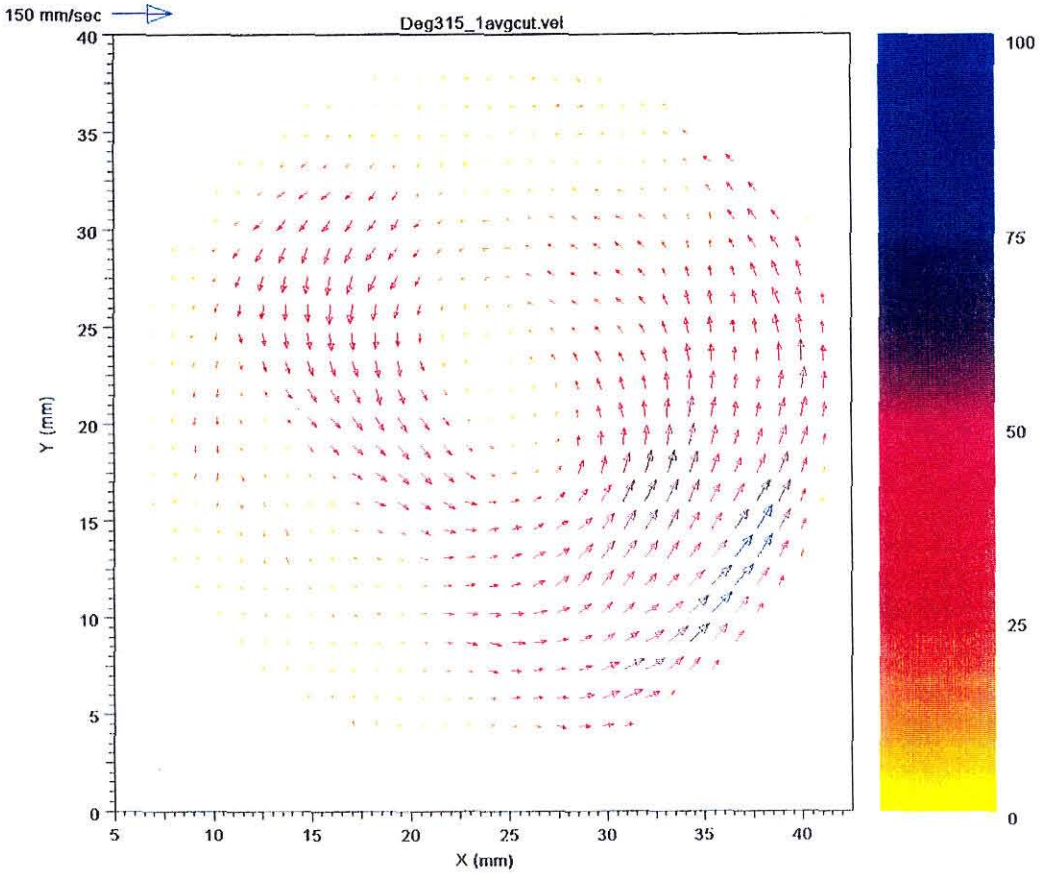

Figure B.10: The velocity field of the pulsatile flow in the curved vessel model with upstream constriction $\beta = 80\%$ asymmetrically positioned at 315^0 with respect to the posterior wall. $\alpha = 8.4$.

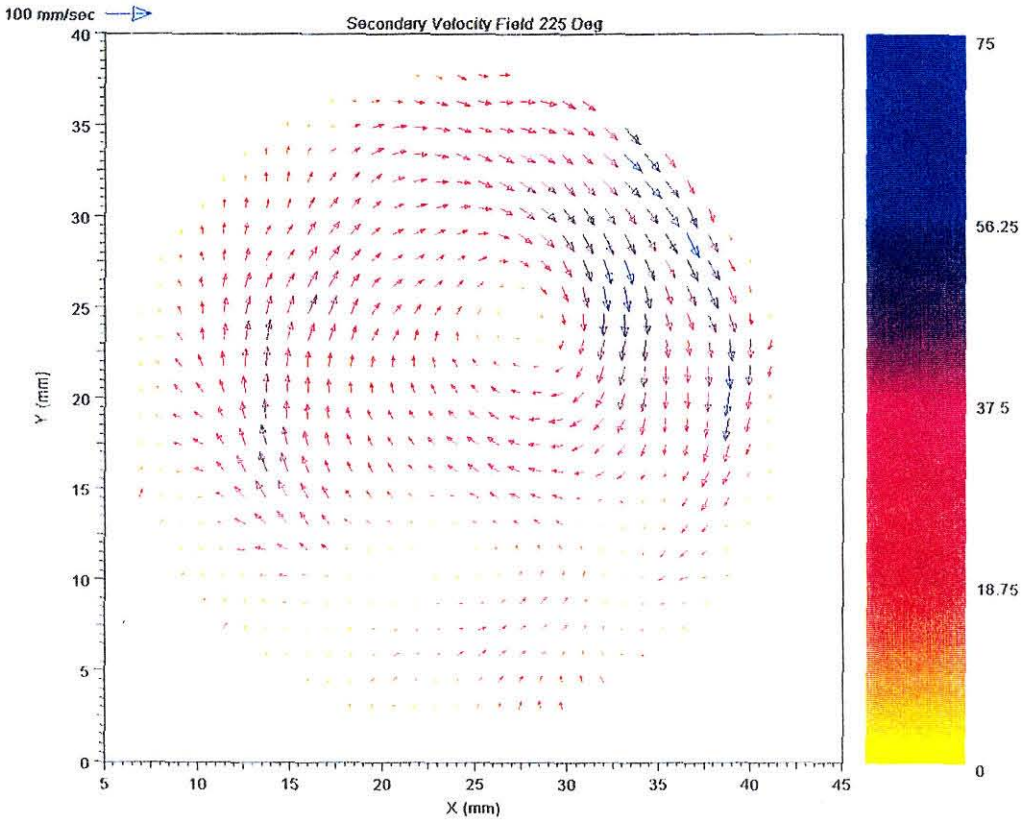

Figure B.11: The velocity field of the pulsatile flow in the curved vessel model with upstream constriction $\beta = 80\%$ asymmetrically positioned at 225^0 with respect to the posterior wall. $\alpha = 12.6$.

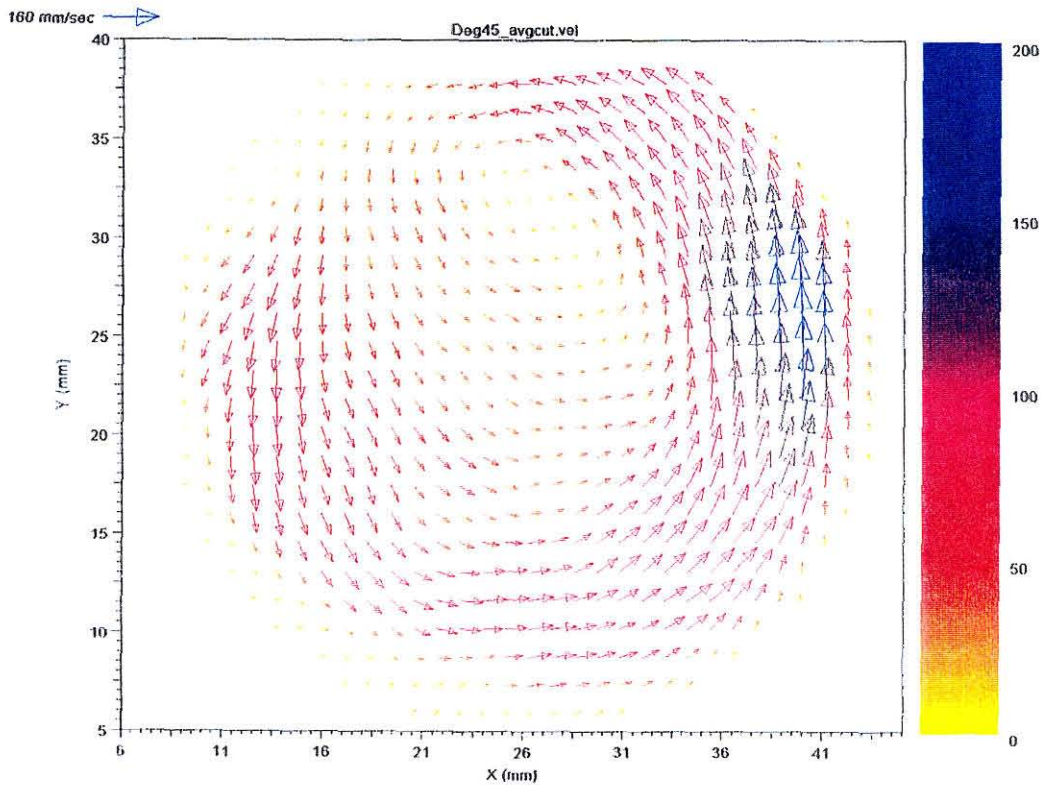

Figure B.12: The velocity field of the pulsatile flow in the curved vessel model with upstream constriction $\beta = 80\%$ asymmetrically positioned at 45^0 with respect to the posterior wall. $\alpha = 8.4$.

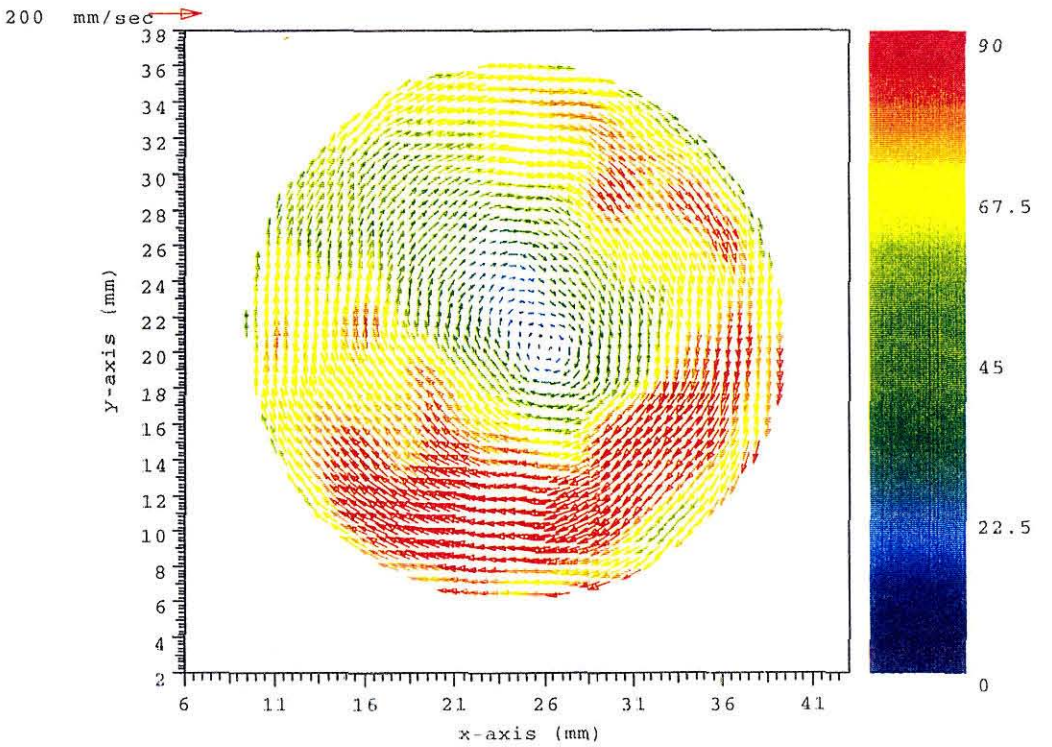

Figure B.13: The velocity field of the pulsatile flow in the curved vessel model with upstream constriction $\beta = 80\%$ asymmetrically positioned at 180^0 with respect to the posterior wall. $\alpha = 12.6$.

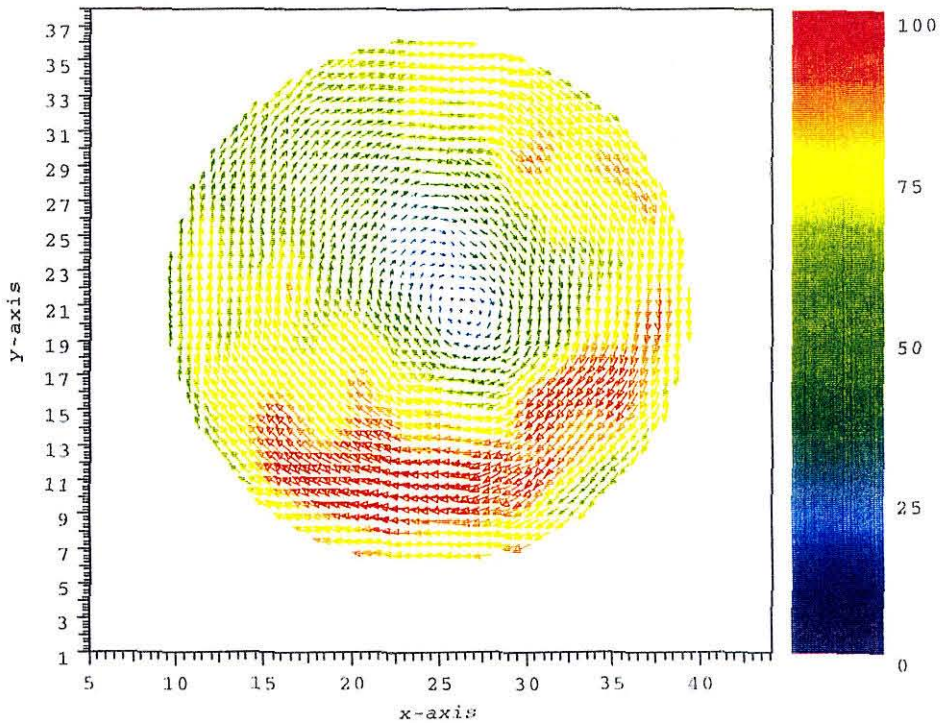

Figure B.14: The velocity field of the pulsatile flow in the curved vessel model with upstream constriction $\beta = 80\%$ asymmetrically positioned at 180^0 with respect to the posterior wall. $\alpha = 8.4$.

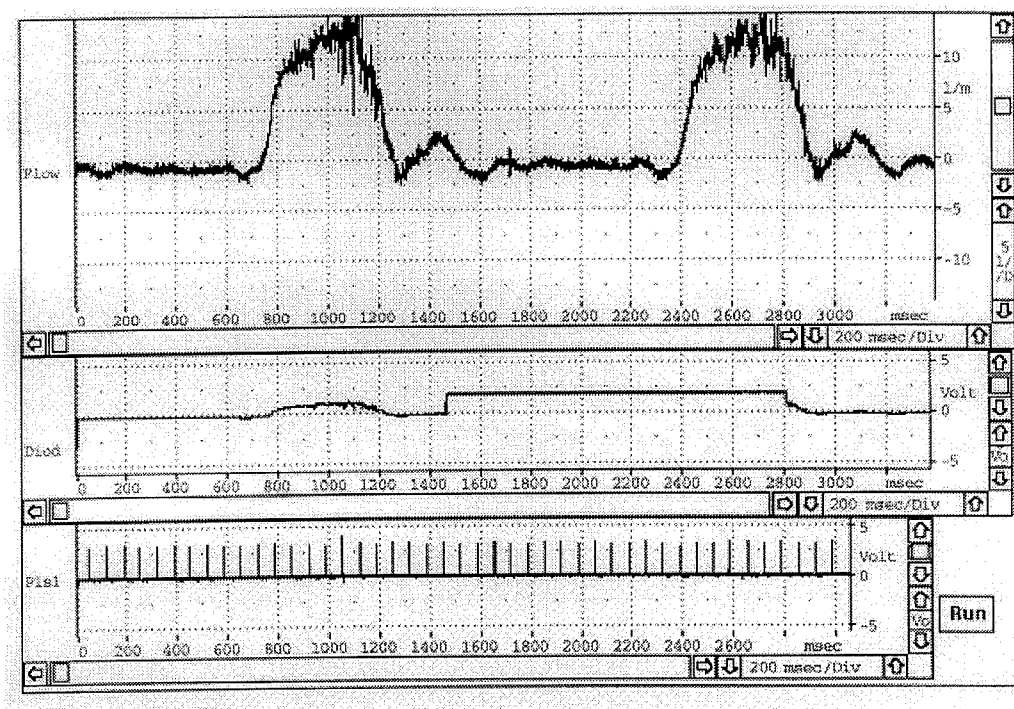

Figure B.15: The flow signal for the pulsatile flow without upstream constriction. $\alpha = 12.5$. The two other signals are the laser pulse signal and the time-reference signal to enable locating the frame position on the flow signal.

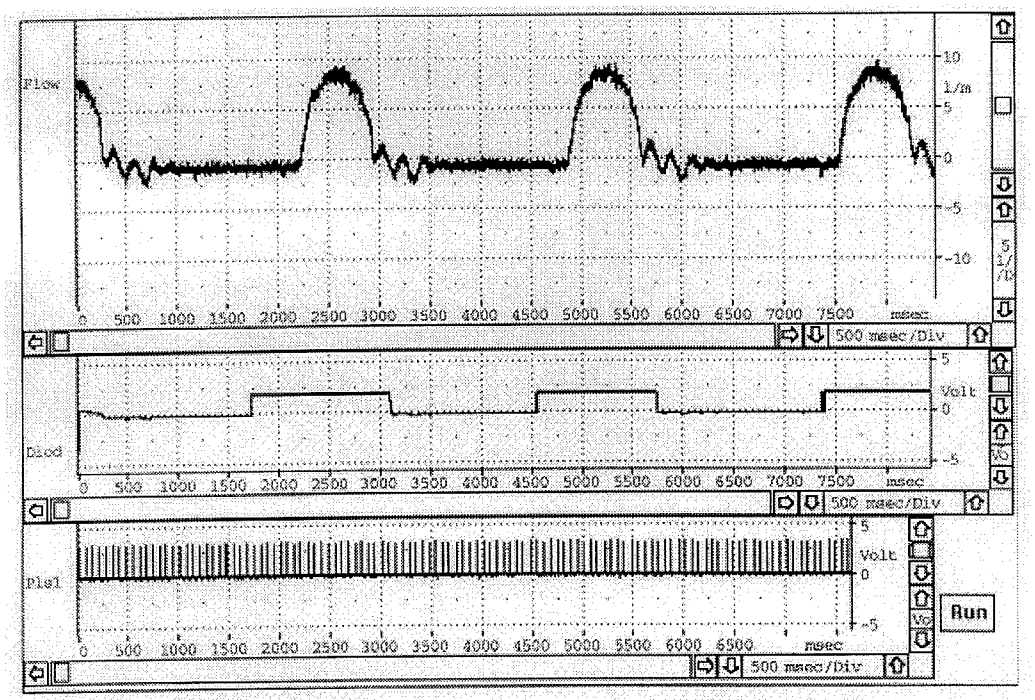

Figure B.16: The flow signal for the pulsatile flow without upstream constriction. $\alpha = 8.4$. The two other signals are the laser pulse signal and the time-reference signal to enable locating the frame position on the flow signal.